الجمهورية الجزائرية الديمقراطية الشعبية

République Algérienne Démocratique et Populaire

وزارة التعليم العالي والبحث العلمي

Ministère de l'Enseignement Supérieur et de la Recherche Scientifique

Université Mohamed Khider – Biskra

Faculté des Sciences Exactes et Sciences de la Nature et de la Vie

جامعة محمد خيضر - بسكرة

كلية العلوم الدقيقة و علوم الطبيعة و الحياة

Thèse présentée en vue de l'obtention du diplôme de:

Doctorat LMD

Option**:**

Physique des matériaux

Thème

تصميم و بحث الخلايا الشمسية ذات الطبقات الرقيقة II-VI

Design and investigate of II-VI thin film solar cells

Conception et investigation des cellules solaires en couches minces II-VI

Par

Chala Slimane

Jury

Nom et Prénom	**Grade**	**Etablissement**	**Qualité**
Meftah Afak	Professeur	U.M.K. Biskra	Présidente
Sengouga Nouredine	Professeur	U.M.K. Biskra	Encadreur
Meftah Amjad	Professeur	U.M.K. Biskra	Examinatrice
Rahmane Saâd	Professeur	U.M.K. Biskra	Examinateur
Benhaliliba Mostefa	Professeur	U.S.T.M.B. Oran	Examinateur
Ayadi Kamel Eddine	Professeur	U.K.M. Ouargla	Examinateur

Acknowledgement

I would like to thank everyone who supported me
and helped me to get my PhD.

ملخص

الطاقة الشمسية هي واحدة من المجالات الواعدة كبديل لمصادر الطاقة التقليدية. ولكن كفاءة الألواح الشمسية اليوم هي أبعد ما تكون لاختيار هذا القطاع. المكون الأساسي لهذه الصناعة هي الخلية الشمسية. هذه الأخيرة يمكن أن تشمل مختلف المركبات نصف الناقلة مثل السيليكون. السيليكون المبلور مكلف للغاية. وكبديل أقل تكلفة للخلايا الشمسية هي الطبقات الرقيقة. يتوسط أفضل أداء قليل التكلفة السيليكون غير المتبلور (a-Si) وأنصاف النواقل II-VI (CdO, CdTe, CdSe, CdS, ZnO, ZnTe, ZnSe, ZnS...).

الأكاسيد الناقلة الشفافة (TCO) ذات السمك الرقيق لها أهمية كبيرة في تطبيقات الأجهزة الإلكترونية. وأغلبها تعتبر أنصاف نواقل II-VI التي غالبا ما تكون أكاسيد المعادن (ZnO, CdO, MgO...). كما أنها تكون أنصاف نواقل نوع n مع وجود نطاق طاقة كبير، وتعتبر واحدة من المركبات الواعدة للتطبيقات الكهروضوئية بسبب الناقلية الكهربائية العالية، و التمرير الضوئي في النطاق المرئي من الطيف الشمسي.

لقد زاد الاهتمام بدراسة أكسيد الكادميوم (CdO) و أكسيد الزنك (ZnO) للتطبيقات الضوئية بشكل ملحوظ بسبب خصائصهما الكهربائية والضوئية الواعدة. تظهر الخلايا الشمسية الحقيقية CdO/p-Si و ZnO/p-Si غير متجانسة البنية ضعف في الأداء الكهروضوئي. في هذا العمل نستخدم المحاكاة العددية لتوضيح هذا الأداء الضعيف من خلال النظر في حالتين. أولا باعتبار CdO و ZnO أنصاف نواقل بلورية مثالية. ثانيا باعتبار CdO و ZnO أنصاف نواقل ذوات توزيع مستمر لحالات العيوب في نطاق الطاقة، كما هو الحال في نصف ناقل غير متبلور، متكون من عصابتين من ذيل عصابة الطاقة (شبه مانحات وشبه مستقبلات) و من عصابتين من توزيع جاوس في المستوى العميق (شبه مانحات وشبه مستقبلات). يتضح بأن الحالة الأولى أعطت نتائج بعيدة عن الواقع. و في الحالة الثانية، وبطريقة ما، وعن طريق تعديل مقومات حالات عصابة نطاق الطاقة، كنا قادرين على الحصول على توافق جيد بين المحاكاة العددية والقياسات لهذه الخلايا الشمسية.

Abstract

Solar energy is one of the promising sectors as an alternative to conventional energy sources. But the efficiencies of solar panels today are far from conclusive for the choice of this sector. The basic component of this industry is the solar cell. The latter can be carried out by various semiconductor materials such as silicon. The monocrystalline silicon is very expensive. A cheaper alternative is solar cells in thin layers. The best compromise performance-cost amorphous silicon are the chains (a-Si) and II-VI semiconductors (CdO, CdTe, CdS, ZnO, ZnTe, ZnS ...). The transparent conductive oxides (TCO: Transparent Conducting Oxides) thin films have great importance in applications of electronic devices. They are based on II-VI semiconductors which are often metal oxides (ZnO, CdO, MgO...). They are n-type semiconductors with a high energy gap and it is considered one of promising materials for photovoltaic applications due to its high electrical conductivity and optical transmission in the visible region of solar spectrum. The interest in the study of Cadmium oxide (CdO) and Zinc oxide (ZnO) for photonic applications has increased significantly because of their promising electrical and optical properties. Real solar cells based on CdO/p-Si and ZnO/p-Si heterostructures show a poor photovoltaic performance. However, in this work numerical simulation is used to elucidate this poor performance by considering two cases. CdO and ZnO are firstly considered as perfect crystalline semiconductors. The second case models CdO and ZnO as semiconductors with continuous distribution of defects states in their band gaps, similar to an amorphous semiconductor, made of two tail bands (donor-like and acceptor-like) and two Gaussian distribution deep level bands (acceptor-like and donor-like). Evidently the first case produced results far from reality. In the second case, however, and by adjusting the constituents of the band gap states we were able to reproduce a good agreement between simulation and measurements of these solar cells.

Résumé

L'énergie solaire est l'une des filières très prometteuse comme alternatif aux sources d'énergie classique. Mais le rendement des panneaux solaires aujourd'hui sont loin d'être concluantes pour le choix de cette filière. Le composant de base de cette filière est la cellule solaire. Cette dernière peut être réalisée par différents matériaux semi-conducteurs comme le silicium. Le Silicium monocristallin s'avère très couteux. Une alternative moins chère est les cellules solaires en couches minces. Les meilleurs compromis rendement-cout sont les filières silicium amorphe (a-Si) et les semiconducteurs II-VI (CdO, CdTe, CdS, ZnO, ZnTe, ZnS…). Les oxydes conducteurs transparent (TCO : Transparent Conducting Oxides) des films minces ont une grande importance dans des applications de dispositifs électroniques. Ils sont basés sur les semiconducteurs II-VI qui sont souvent des oxydes métalliques (ZnO, CdO, MgO...). Ils sont des semiconducteurs de type n avec un gap d'énergie élevée et il est considéré comme l'un des matériaux prometteurs pour les applications photovoltaïques en raison de sa grande conductivité électrique et la transmission optique dans la région visible du spectre solaire. L'intérêt pour l'étude d'oxyde de Cadmium (CdO) et d'oxyde de Zinc (ZnO) pour les applications photoniques a augmenté considérablement en raison de ses propriétés électriques et optiques prometteuses. Des cellules solaires réelles à base d'hétérostructures CdO/p-Si et ZnO/p-Si présentent cependant une faible performance photovoltaïque. Dans ce travail, la simulation numérique est utilisée pour élucider cette mauvaise performance en considérant deux cas. Le CdO et le ZnO sont tout d'abord considérés comme des semi-conducteurs cristallins parfaits. Le deuxième cas modélise CdO et ZnO en tant que semiconducteurs avec une distribution continue d'états de défauts dans leurs band-gaps, semblable à un semi-conducteur amorphe, constitué de deux bandes de queue (accepteurs et donneurs) et deux bandes Gaussiennes de niveau profond (accepteurs et donneurs). Évidemment, le premier cas a produit des résultats loin de la réalité. Dans le second cas, cependant, et en ajustant les constituants des états de band-gap, nous avons pu reproduire un bon accord entre la simulation et les mesures de ces cellules solaires.

Table of contents

ملخص .... **i**

Abstract .... **ii**

Résumé .... **iii**

Table of contents .... **iv**

List of figures .... **vii**

List of tables .... **x**

Chapter 1: Introduction **2**

Chapter 2: Semiconductors **5**

2.1. Introduction: 5

2.2. Materials classification: 5

2.2.1. Conductors: 8

2.2.2. Insulators: 8

2.2.3. Semiconductors: 9

2.3. Semiconductors: 9

2.3.1. The Fermi-Dirac distribution function and Fermi level: 9

2.3.2. Intrinsic semiconductors: 10

2.3.3. Extrinsic semiconductors: 11

2.4. Semiconductor types: 14

2.4.1. Elemental semiconductors: 14

2.4.2. Binary semiconductors: 15

2.5. Defects in crystals: 18

2.5.1. Point defects: 19

2.5.2. Line defects: 21

2.5.3. Surface defects: 22

2.5.4. Volume defects: 24

2.5.5. ZnO defects: 24

2.5.6. CdO defects: 25

2.6. Basic semiconductor equations: 26

2.6.1. Poisson's equation: 26

2.6.2. Carrier continuity equations: 26

2.6.3. The transport equations: 27

Chapter 3: Solar cells 30

3.1. Introduction: 30

3.2. Typical solar cell structures: 30

3.2.1. The p-n junction: 30

3.2.2. The p-n junction solar cell: 31

3.2.3. Homojunction and Heterojuction: 33

3.3. Electrical characteristics: 35

3.3.1. The ideal solar cell: 35

3.3.2. Reel solar cell characteristics: 37

3.4. The quantum efficiency: 39

3.5. II-VI thin film solar cells: 40

3.5.1. The use of II-VI thin films in solar cells: 40

3.5.2. Characterization of II-VI thin film solar cells: 41

Chapter 4: Experimental and simulation methods 43

4.1. Introduction: 43

4.2. Experimental method: 43

4.2.1. Sol-gel: 43

4.2.2. CdO thin film: 45

4.2.3. ZnO thin film: 46

4.2.4. Characterization equipment 47

4.3. Simulation method: 50

4.3.1. ATLAS (by SILVACO): 50
4.3.2. Atlas inputs and outputs: 50
4.3.3. Modes of operation: 51
4.3.4. Atlas commands: 52
Chapter 5: Results and discussion 62
5.1. Introduction: 62
5.2. Experimental results: 62
5.2.1. Characterization of CdO thin film: 62
5.2.2. Characterization of CdO/p-Si solar cell: 64
5.2.3. Characterization of ZnO thin film: 66
5.2.4. Characterization of ZnO/p-Si solar cell: 71
5.3. Simulation results: 72
5.3.1. Important equations for simulation: 72
5.3.2. CdO modelling: 75
5.3.3. ZnO modelling: 86
5.4. Conclusion: 89
Chapter 6: Conclusion and perspectives 91
6.1. Conclusion: 91
6.2. Perspectives: 92
References 94
Publications and communications 103

List of figures

Figure 2.1: The splitting of energy state into a band of allowed energies. r_0 is the equilibrium interatomic distance in the crystal. 6
Figure 2.2: Schematic showing the splitting of three energy states into allowed bands of energies. 7
Figure 2.3: Formation the allowed and forbidden energy bands. 7
Figure 2.4: The energy band positions in a semiconductor at 0 K. 8
Figure 2.5: Difference between energy bands of (a) conductors, (b) insulators and (c) semiconductors. 9
Figure 2.6: Structure of extrinsic semiconductors, n-doped and p-doped. 12
Figure 2.7: Elemental Semiconductors Silicon and Germanium. 15
Figure 2.8: II-VI semiconductor compounds. 16
Figure 2.9: Zinc oxide crystal structure. 17
Figure 2.10: Cadmium oxide crystal structure. 18
Figure 2.11: Schematic for vacancy and self-interstitial defects. 20
Figure 2.12: Schematic for Substitution and Interstitial defects. 20
Figure 2.13: Schematic for Frenkel and Schottky defects. 21
Figure 2.14: Schematic for line defects screw and edge dislocation. 22
Figure 2.15: Schematic of orientation change across the grain boundary. 23
Figure 2.16: Energy levels of native defects in ZnO. 24
Figure 2.17: Formation energies as a function of the Fermi level in CdO 25
Figure 3.1: The bulk of the cell is formed by a thick p-type base where most of the incident light is absorbed and most power is generated. 30
Figure 3.2: Formation of a PN junction in the Schottky approximation. (a) space-charge distribution due to fixed ionized dopants; (b) electric field obtained by integration of the Poisson equation; (c) a second integration step results in the electrostatic potential. 31
Figure 3.3: The p-n junction at open circuit. 33
Figure 3.4: The three types of semiconductor Heterojuction organized by band alignment. 34
Figure 3.5: Band diagrams for straddling-gap Heterojuction. 35

Figure 3.6: The equivalent circuit of an ideal solar cell (full lines). Non-ideal components are shown by the dotted line. 35
Figure 3.7: The I-V characteristics of a solar cell. The power generated at the maximum power point is equal to the shaded rectangle. 36
Figure 3.8: The power produced by solar cell. 37
Figure 3.9: The superposition principle for solar cells..37
Figure 3.10: The I-V characteristic of the solar cell in the two diode model for three values of the ratio I_{02}/I_{01}..38
Figure 3.11: The effect of the series resistance (a) and parallel resistance (b) on the I-V characteristic of the solar cell. 38
Figure 3.12: The dark I-V characteristic of a solar cell for the two-diode model including the series resistance.The shunt resistance has a similar effect to the second diode. 39
Figure 4.1: Schematic of spin coating process. 44
Figure 4.2: Schematic of dip coating process. 44
Figure 4.3: A two dimensional schematic representation of the cross-section of the Al/CdO/p-Si/Al solar cell. 46
Figure 4.4: A two dimensional schematic representation of the cross-section of the ZnO/p-Si/Al diode. 47
Figure 4.5: Schematic diagram of a dual beam spectrophotometer operating in transmittance mode..49
Figure 4.6: Shimadzu UV–vis–NIR 3600 spectrophotometer...............................49
Figure 4.7: Atlas inputs and outputs. 51
Figure 4.8: Non-uniform mesh creation using Atlas syntax. 53
Figure 4.9: Analytical specification of a 2D Profile. 55
Figure 5. 1: Plots of transmittance and $(\alpha h\nu)^2$ vs. $h\nu$ for the nanostructure CdO film [4]. 63
Figure 5. 2: Characteristics of the Al/CdO/p-Si/Al solar cell [4]. 65
Figure 5.3: Plots of Isc and Voc vs. P of the Al/CdO/p-Si/Al solar cell [4]. 65
Figure 5. 4: Optical transmittance (T) as function of wavelength. 66
Figure 5. 5: Optical reflectance (R) as function of wavelength. 67
Figure 5. 6: Absorption coefficient (α) as function of wavelength. 68
Figure 5. 7: $(\alpha h\nu)^2$ as function of wavelength. 68
Figure 5. 8: Refractive index (n) as function of wavelength. 69

Figure 5. 9: Extinction coefficient (k) as function of wavelength. 70
Figure 5. 10: Real dielectric constant (ε_1) as function of photon energy. 71
Figure 5. 11: Imaginary dielectric constant (ε_2) as function of photon energy. 71
Figure 5. 12: Characteristics of the ZnO/p-Si solar cell [5]. 72
Figure 5.13: The simulated J-V characteristics of the ideal Al/n-CdO/p-Si/Al solar cell under AM1.5 spectrum. 76
Figure 5.14: The density of states (Gaussian and tail) in the nergy gap of CdO. 78
Figure 5.15: The simulated J-V characteristics of the non-ideal Al/CdO/p-Si/Al solar cell under AM1.5 spectrum for variable acceptor-like and donor-like deep Gaussian bands in the CdO film. 79
Figure 5.16: The effect of deep level Gaussian bands in the CdO film on the solar cell performance parameters under AM1.5 spectrum. 80
Figure 5.17: The simulated J-V characteristics of the non-ideal Al/CdO/p-Si/Al solar cell under AM1.5 spectrum for variable acceptor-like and donor-like deep tail states in the CdO film. 81
Figure 5.18: The effect of the density of the tail states at the conduction and valence band edges in the CdO film on the solar cell performance parameters under AM1.5 spectrum. 82
Figure 5.19: The simulated J-V characteristics of the non-ideal Al/CdO/p-Si/Al solar cell under AM1.5 spectrum for variable p-type doping of......................83
Figure 5.20: The extracted figures of merit extracted from the simulated J-V characteristics of the non-ideal Al/CdO/p-Si/Al solar cell under AM1.5 spectrum for variable p-type doping of Silicon. 84
Figure 5.21: Comparison of simulated and measured J-V characteristics of the Al/CdO/p-Si/Al solar cell diode for different illumination power intensities. ..85
Figure 5.22: Comparison of the Al/CdO/p-Si/Al solar cell parameters extracted from the simulated and measured J-V characteristics of Figure 5.21 for different illumination power intensities. 86
Figure 5.23: Comparison of simulated and measured J-V characteristics of the ZnO/p-Si solar cell. 88

List of tables

Table 2.1: Some properties of CdO and ZnO thin films 18
Table 4.1: The order of Atlas commands 52
Table 5.1: Parameters used to simulate the CdO film of the ideal Al/CdO/p-Si/Al solar cell..75
Table 5.2: Parameters used to simulate silicon of the ideal Al/CdO/p-Si/Al solar cell. 76
Table 5.3: Parameters of the DOS used to simulate the CdO film of the Al/CdO/p-Si/Al solar cell. 77
Table 5.4: Parameters used to simulate the ZnO film of the ideal ZnO/p-Si/Al solar cell. 87
Table 5.5: Parameters of the DOS used to simulate the ZnO film of the ZnO/p-Si/Al solar cell..87
Table 5.6: Table gathers all parameter values which gave comparable simulation and measurement of both CdO/p-Si and ZnO/p-Si solar cells..........................88

Chapter 1: Introduction

Chapter 1: Introduction

A solar cell, or photovoltaic (PV) cell, is an electrical device that converts the energy of light directly into electricity by the photovoltaic effect. It is a form of photoelectric cell, defined as a device whose electrical characteristics vary when exposed to light.

The primary objective of the worldwide PV solar cell research and development is to reduce the cost to a level that it will be a viable alternative to conventional ways of generating electric power. PV technology in the marketplace today is dominated by crystalline silicon. It is generally believed that even with greatly increased market and production volume, the price of crystalline or polycrystalline silicon cannot be reduced to meet the long-term cost goal for large-scale power production. In fact, various analyses suggest that thin film solar cells are the only viable alternative that has the potential to meet this long-term cost goal. If one accepts this rationale, it is instructive to analyze whether thin film technology can realistically meet these goal. There is reason to be very optimistic, particularly in view of the remarkable progress that has been made in recent years, both in terms of cell efficiency and long-term stability in several thin film solar cell technologies [1].

II-VI compounds are one of the common thin films which have technologically important applications. They have higher bandgap energy than the corresponding III-V compounds due to the larger ionicity in II-VI compounds. Because of their large optical absorption coefficients at above bandgap wavelengths, a II-VI semiconductor of about 1 pm thickness is sufficient to absorb 99% of the impinging radiation with photon energy higher than the bandgap energy. Thus, they are well-suited for thin film optical devices. II-VI compounds also have the advantage that they can be prepared in the form of high quality polycrystalline films from inexpensive raw materials by several low-cost methods. Thus, the use of thin film II-VI compounds is an economically viable approach to the terrestrial utilization of solar energy [2].

II-VI Metal-oxide-semiconductors such as CdO and ZnO, have been used extensively for solar cell applications as transparent conducting oxide (TCO) thin films. Cadmium oxide (CdO) and Zinc Oxide (ZnO) are n-type semiconductors with band gaps of 2.5 eV and 3.37 eV, respectively, which can be used as well as emitters of the p-n junctions [6-8]. However, CdO/p-

Si and ZnO/p-Si heterojunction solar cells which were fabricated by sol-gel method show poor photovoltaic performance [4], [5].

In this work, sol-gel method is used, at Firat University, Elazig-Turkey, to fabricate the CdO and ZnO thin films then numerical simulation software, ATLAS Silvaco, is used to model the aforementioned solar cells and to elucidate their poor performance based on input files include the experimental properties of the prepared CdO and ZnO.

The same CdO/p-Si and ZnO/p-Si heterostructure solar cells have been simulated with considering the CdO and ZnO as semiconductors with continuous distribution of states in their band gaps similar to an amorphous semiconductor. The density of states model used here is composed of four bands: two tail bands and two Gaussian distribution deep level bands. Good comparison between experimental and simulation results were obtained.

This thesis is divided into five parts presented as chapters.

Chapter 1: In this chapter, we present general introduction includes an overview, experimental and simulation methods and aim and objectives of this thesis.

Chapter 2: Contains a description of the fundamental concepts of semiconductors, crystal structure, summary about defects in semiconductors, the properties of II-VI semiconductors and its defects, namely CdO and ZnO.

Chapter 3: Contains some definitions and principles of photovoltaic solar cells including II-VI thin film solar cells.

Chapter 4: Includes definition and description of the experimental technique, Sol-gel, and the simulation software, SILVACO, were used in this study.

Chapter 5: In this chapter where we summarized all experimental and simulation results and discussions of the thin films and the solar cells. In the first case, the CdO and ZnO films will be considered as a crystalline semiconductor (absence of defects). In the second case, the CdO and ZnO films will be considered as an amorphous semiconductor, i.e contains a continuously distributed energy states in its band-gap due to the presence of defects. The results and discussion of solar cell performances are based on the open circuit voltage V_{oc}, short circuit current J_{sc} , efficiency η and Fill Factor FF.

Chapter 6: Concludes the thesis with a summary and recommendations for future work.

Chapter 2: Semiconductors

Chapter 2: Semiconductors

2.1. Introduction:

In most of today solar cells the absorption of photons, which results in the generation of the charge carriers, and the subsequent separation of the photo-generated charge carriers take place in semiconductor materials. Therefore, the semiconductor layers are the most important parts of a solar cell. There are a number of different semiconductor materials that are suitable for the conversion of energy of photons into electrical energy, each having advantages and drawbacks. These details are illustrated in this chapter in five important parts

The first part: discusses the materials classification, conductors, insulators and semiconductors.

The second part: explains the most important concepts of semiconductors.

The third part: includes brief definitions of elementary and binary semiconductors such as CdO and ZnO which were used to fabricate the studied solar cells in this work.

The fourth part: consists of some types of semiconductor defects of studied semiconductors.

The fifth part: contains the basic semiconductor equations.

2.2. Materials classification:

According to the Bohr atomic model, in an isolated atom the energy of any of its electrons is decided by the orbit in which it revolves. But if we somehow start with a regular periodic arrangement of atoms that are initially very far apart, and begin pushing them together, the initial quantized energy level will split into a band of discrete energy levels, Figure 2.1 [6], [7].

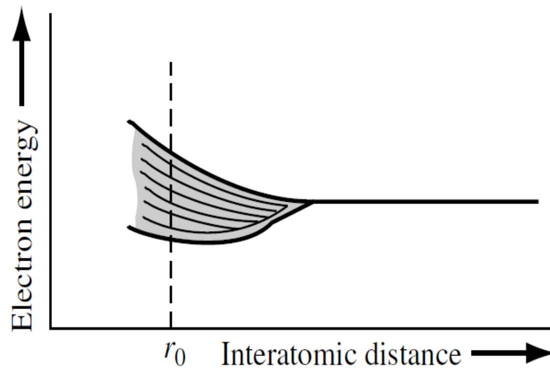

Figure 2.1: The splitting of energy state into a band of allowed energies. r_0 is the equilibrium interatomic distance in the crystal.

At the equilibrium interatomic distance, there is a band of allowed energies, but within the allowed band, the energies are at discrete levels. The Pauli Exclusion Principle states that the joining of atoms to form a system (crystal) does not alter the total number of quantum states regardless of size. However, since no two electrons can have the same quantum number, the discrete energy must split into a band of energies in order that each electron can occupy a distinct quantum state [7].

Consider again a regular periodic arrangement of atoms, in which each atom contains more than one electron. If the atoms are initially very far apart, the electrons in adjacent atoms will not interact and will occupy the discrete energy levels. If these atoms are brought closer together, the outermost electrons in the $n = 3$ energy shell will begin to interact initially, so that this discrete energy level will split into a band of allowed energies. If the atoms continue to move closer together, the electrons in the $n = 2$ shell may begin to interact and will also split into a band of allowed energies. Finally, if the atoms become sufficiently close together, the innermost electrons in the $n = 1$ level may interact, so that this energy level may also split into a band of allowed energies. The splitting of these discrete energy levels is qualitatively shown in Figure 2.2 [7].

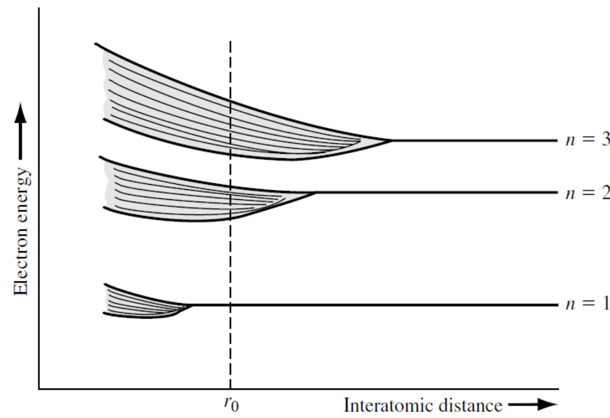

Figure 2.2: Schematic showing the splitting of three energy states into allowed bands of energies.

If the equilibrium interatomic distance is r_0, then we have bands of allowed energies that the electrons may occupy separated by bands of forbidden energies. This energy-band splitting and the formation of allowed and forbidden bands is the energy-band theory of single-crystal materials. The actual band splitting in a crystal is much more complicated than indicated in Figure 2.2. Figure 2.3 shows the band splitting of silicon. We need only consider the $n = 3$ level for the valence electrons, since the first two energy shells are completely full and are tightly bound to the nucleus. The 3s state corresponds to $n = 3$ and $l = 0$ and contains two quantum states per atom. This state will contain two electrons at $T = 0$ K. The 3p state corresponds to $n = 3$ and $l = 1$ and contains six quantum states per atom. This state will contain the remaining two electrons in the individual silicon atom. As the interatomic distance decreases, the 3s and 3p states interact and overlap. At the equilibrium interatomic distance, the bands have again split, but now four quantum states per atom are in the lower band and four quantum states per atom are in the upper band [7].

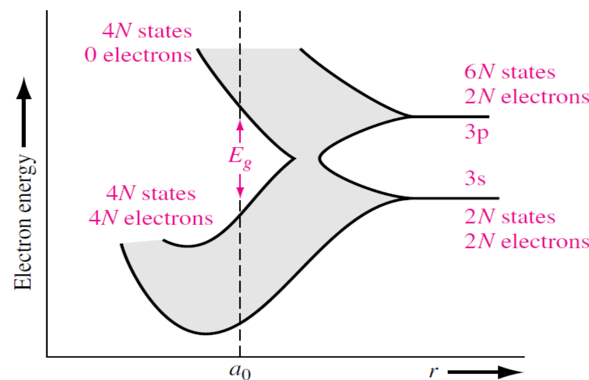

Figure 2.3: Formation the allowed and forbidden energy bands.

At T = 0 K, electrons are in the lowest energy state, so that all states in the lower band (the valence band) will be full and all states in the upper band (the conduction band) will be empty. The lowest energy level in the conduction band is shown as E_C and highest energy level in the valence band is shown as E_V. Above E_C and below E_V there are a large number of closely spaced energy levels. The gap between the top of the valence band and bottom of the conduction band is called the energy band gap (Eg). It may be large, small, or zero, depending upon the material [6]. These different situations are depicted in Figure 2.4 and discussed below:

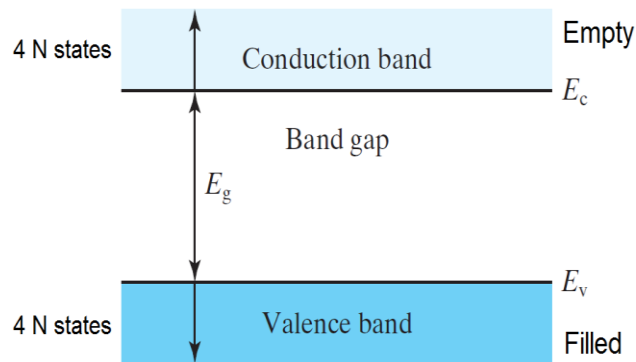

Figure 2.4: The energy band positions in a semiconductor at 0 K.

2.2.1. Conductors:

As shown in Figure 2.5(a), the conduction band is partially filled and the balanced band is partially empty or the conduction and the valence bands overlap. When there is overlap, electrons from valence band can easily move into the conduction band. This makes a large number of electrons available for electrical conduction. If the valence band is partially empty, electrons from its lower level can move to higher level making conduction possible [6].

2.2.2. Insulators:

As shown in Figure 2.5(b), a large energy band gap (Eg >3 eV) exists. There are no electrons in the conduction band, and therefore no electrical conduction is possible. In case of insulators, the energy gap is very large that electrons cannot be excited from the valence band to the conduction band by thermal excitation [6].

2.2.3. Semiconductors:

As shown in Figure 2.5(c), a finite but small energy band gap (Eg < 3 eV) exists. At room temperature and due to the small band gap, some electrons from valence band can acquire enough energy to cross the energy gap to enter the conduction band. These electrons (though small numbers) can move in the conduction band [6].

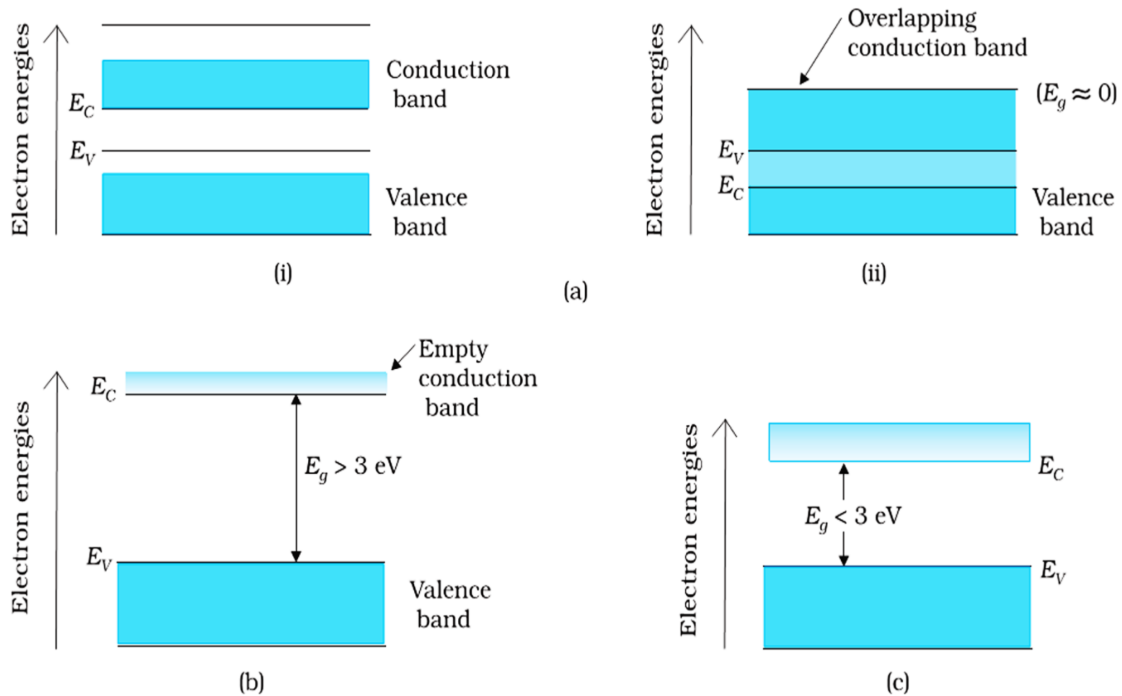

Figure 2.5: Difference between energy bands of (a) conductors, (b) insulators and (c) semiconductors.

2.3. Semiconductors:

2.3.1. The Fermi-Dirac distribution function and Fermi level:

The conduction band in a piece of semiconductor consists of many available, allowed, empty energy levels.

When calculating how many electrons will fill these levels and thus be counted in n, contributing to conductivity, we consider two factors:

- How many energy levels are there within a given range of energy?

and

- How likely is it that each level will be populated by an electron?

The likelihood in the second item is given by a probability function called the *Fermi-Dirac* distribution function. f(E) is the probability that a level with energy E will be filled by an electron, and the expression is:

$$f(E) = \frac{1}{1 + exp(\,(E - E_F\,)/(k_B T)\,)} \qquad (2.1)$$

Since *f(E)* is the probability that the energy level E will be filled by an electron, *(1-f(E))* is the probability that the energy level E will be empty (have a hole).

f(E) around E_F can be easily shown that

$$f(E_F + E) = 1 - f(E_F - E) \qquad (2.2)$$

2.3.2. Intrinsic semiconductors:

An intrinsic semiconductor is pure undoped semiconductor i.e. there is no foreign atom in its crystal lattice and no mobile carriers at 0° K. When an electron in an intrinsic semiconductor gets enough energy (T > 0° K), it can go to the conduction band and leave behind a hole. This process is called electron hole pair creation.

2.3.2.1. Carrier concentration:

For the intrinsic material, since electrons and holes are always created in pairs,

$$n = p = n_i \qquad (2.3)$$

where n_i is the intrinsic carrier concentration.

2.3.2.2. Fermi level:

In an intrinsic semiconductor, *n=p*. If we use the band-symmetry approximation, which assumes that there are equal number of states in equal-sized energy bands at the edges of the conduction and valence bands, *n=p* implies that there is an equal chance of finding an electron at the conduction band edge as there is of finding a hole at the valence band edge:

$$f(E_C) = 1 - f(E_V\,) \qquad (2.4)$$

From Eq. 2.2 we can deduce that the Fermi level E_F must be in the middle of the bandgap for an intrinsic semiconductor. In fact, this level is called the "intrinsic Fermi level" and shown by E_{Fi}:

$$E_{Fi} = E_C - \frac{Eg}{2} = E_V + \frac{Eg}{2} \qquad (2.5)$$

where *Eg* is the bandgap energy.

2.3.3. Extrinsic semiconductors:

The intrinsic semiconductor can be modified into an extrinsic semiconductor by adding impurities, called dopant atoms, to improve its carrier concentration and this improving in electrical conductivity.

We can get two types of extrinsic material n-type and p-type:

a- **n-type:**

If one of the atoms of the semiconductor crystal is replaced by a pentavalent, donor, atom (phosphorus (P), arsenic (As) or antimony (Sb)), only four of the electrons are used for the formation of the covalent bonds with a neighbouring atoms, while the fifth is not bonded to any specific atom and it can easily, At room temperature, jump to the conduction band, leaving a positively charged atom behind. This additional electron is free for conduction. This process is sometimes called activation or ionization of the donor atoms [8].

The positively charged donor atom that is left behind after ionization is immobile and does not contribute to conduction. The electron leaving the atom by ionization does, and is counted in the electron concentration n. Because the activation energy is low, at room temperature almost all of the donor atoms included in the crystal will give an electron to the conduction band. So if N_D is the donor concentration, for an n-type material at equilibrium:

$$n_0 \approx N_D \; [cm^{-3}] \qquad (2.6)$$

b- **p-type:**

The dopant atoms in this case are acceptor atoms.

For silicon, we can use boron (B), Aluminum (Al) and Gallium (Ga) as acceptors. These are column III elements, with three electrons in their outermost shell. When these atoms are included in the silicon crystal, one of the electrons in the silicon valence band can easily jump to the valence shell of one of the acceptor atoms, leaving a hole behind and making the acceptor atom negatively charged [8].

The negatively charged acceptor atom after an electron joins its valence shell is immobile and does not contribute to conduction. The hole left behind by that electron does, and is counted in the hole concentration p. Because the activation energy is low, at room temperature almost all of the acceptor atoms included in the crystal will accept an electron from the valence band. So if N_A is the acceptor concentration, for a p-type material at equilibrium:

$$p_0 \approx N_A \; [cm^{-3}] \qquad (2.7)$$

Both types, n-type and p-type, of extrinsic semiconductors can be explained by illustrated structure in Figure 2.6.

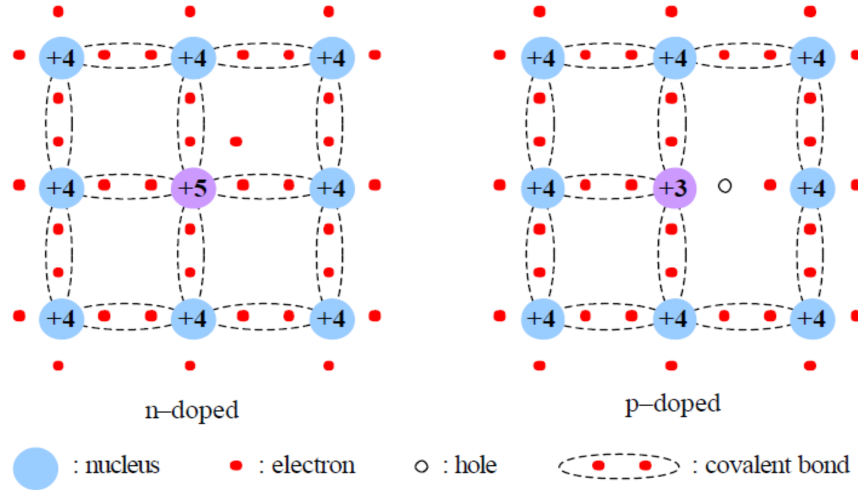

Figure 2.6: Structure of extrinsic semiconductors, n-doped and p-doped.

2.3.3.1. Carrier concentration:

If the concentration of donor atoms (N_D) is greater than the concentration of acceptor atoms (N_A), then the semiconductor material is n-type, (n) is greater than (p):

$$n = N_D - N_A \quad \text{where} \quad p = \frac{n_i^2}{n} \qquad (2.8)$$

If $N_A > N_D$, then the semiconductor material is p-type, because p > n: *f*

$$p = N_A - N_D \quad \text{where} \quad n = \frac{n_i^2}{p} \qquad (2.9)$$

To comprehend the behavior of semiconductors, we need to explore what we mean by the electron and hole densities in the conduction and valence bands, respectively. the notion of energy density of states N(E) is a parameter gives the number of states (per unit volume and per unit energy) between E and E+dE: $N_C(E)$ (respectively, $N_V(E)$) physically represents the "room" available for electrons (resp. holes) in the conduction band (resp. valence band). For energies that are close to the extreme of these two bands, the density of states has a quadratic dependence with E:

$$N_c(E) = \frac{1}{2\pi^2}\left(\frac{2m_c}{\hbar^2}\right)^{3/2}\sqrt{E - E_c} \quad cm^{-3}/eV \qquad (2.10)$$

$$N_v(E) = \frac{1}{2\pi^2}\left(\frac{2m_c}{\hbar^2}\right)^{3/2}\sqrt{E_v - E_c} \quad cm^{-3}/eV \qquad (2.11)$$

where $\hbar$=h/2π is the normalized Planck constant and m_C (resp. m_V) is the average effective mass of the conduction band (resp. of the valence band). For a direct gap semiconductor, m_C (resp. m_V) is the effective mass of an electron m_e (resp. a hole m_h) in the crystal. The density of states is not the only information that we need to identify the number of electrons and holes present in each band. Furthermore, we have to know the probability for an electron to occupy a level with a given energy E. This probability is given by the Fermi-Dirac distribution function:

$$f(E) = \frac{1}{1 + exp[(E - E_F)/k_B T]} \qquad (2.12)$$

where k_B is the Boltzmann constant, T the absolute temperature (K) and E_F the Fermi energy.

1-f(E) gives The probability for a hole to occupy a level of energy E because a hole, in definition, is the absence of an electron. The electron density n [cm^{-3}] (resp. the hole density p) in the conduction band(valance band) is obtained by integrating, over the range of energies accessible by electrons in the band, the number of states that may be occupied by electrons of energy E, weighted by the probability to "find" an electron having this given energy :

$$n = \int_{E_c}^{+\infty} N_c\,(E) f(E) dE \qquad (2.13)$$

$$p = \int_{-\infty}^{E_v} N_v\,(E)\big(1 - f(E)\big) dE \qquad (2.14)$$

In a p-type semiconductor at thermal equilibrium there are a lot of free holes in other word (p) is approximately equal to the density of doped acceptor impurities, giving rise to the p-type conductivity. The hole concentration p is given by

$$p = N_v exp\left(\frac{E_v - E_F}{KT}\right) \qquad (2.15)$$

As the acceptor density increases, E_F tends towards E_V. In addition, there is a very small amount of free electrons with concentration given by

$$n = N_c exp\left(-\frac{E_c - E_F}{KT}\right) \qquad (2.16)$$

The product p.n is independent of both the type and the density of impurities, since (E_C–E_V) is the forbidden band gap E_g of the semiconductor, that is, an intrinsic property. The square root of the product is therefore referred to as intrinsic concentration n_i defined as:

$$n_i = \sqrt{np} = \sqrt{N_c N_v} exp\left(-\frac{E_g}{2KT}\right) \qquad (2.17)$$

2.3.3.2. Fermi level:

For an n-type semiconductor, there are more electrons in the conduction band than there are holes in the valence band. This also implies that the probability of finding an electron near the conduction band edge is larger than the probability of finding a hole at the valence band edge. Therefore, the Fermi level is closer to the conduction band in an n-type semiconductor:

$$n - type: f(E_C) > (1 - f(E_V)) \qquad E_F > E_{Fi} \qquad (2.18)$$

For a p-type semiconductor, there are more holes in the valence band than there are electrons in the conduction band. This also implies that the probability of finding an electron near the conduction band edge is smaller than the probability of finding a hole at the valence band edge. Therefore, the Fermi level is closer to the valence band in an n-type semiconductor.

The following relationships summarize these last points:

$$p - type: f(E_C) < (1 - f(E_V)) \qquad E_F < E_{Fi} \qquad (2.19)$$

2.4. Semiconductor types:

There are several types of semiconductors; in this work we will study two types, elemental and binary semiconductors.

2.4.1. Elemental semiconductors:

The best-known semiconductor is of course the element silicon (Si). Together with germanium (Ge), it is the prototype of a large class of semiconductors with similar crystal structures. The crystal structure of Si and Ge is the same as that of diamond as shown in Figure 2.7. In this structure each atom is surrounded by four nearest neighbor atoms, forming a tetrahedron. These tetrahedrally bonded semiconductors form the mainstay of the electronics industry and the cornerstone of modern technology [9].

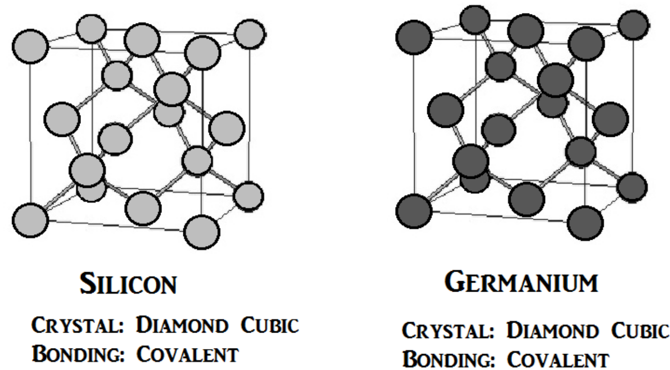

Figure 2.7: Elemental Semiconductors Silicon and Germanium.

2.4.2. Binary semiconductors:

Compounds formed from two elements of the periodic table, normally groups III and V, II and VI or I and VII etc. They have properties very similar to their group IV counterparts.

In going from the group IV elements to the III–V compounds such as GaAs, the bonding becomes partly ionic due to transfer of electronic charge from the group III atom to the group V atom. The ionicity causes significant changes in the semiconductor properties. It increases the Coulomb interaction between the ions and also the energy of the fundamental gap in the electronic band structure. The ionicity becomes even larger and more important in the II–VI compounds such as ZnS. Most of the II–VI compound semiconductors have bandgaps larger than 1 eV. The exceptions are compounds containing the heavy element mercury (Hg). Mercury telluride (HgTe) is actually a zerobandgap semiconductor (or a semimetal). While the large bandgap II-VI compound semiconductors have potential applications for displays and lasers, the smaller bandgap II–VI semiconductors are important materials for the fabrication of infrared detectors. The I–VII compounds (e. g., CuCl) tend to have even larger bandgaps (3 eV) as a result of their higher ionicity. Many of them are regarded as insulators rather than semiconductors [10], [11].

2.4.2.1. II-VI Semiconductors:

II-VI semiconductor compounds are compounds composed of a metal from either group 2 or 12 of the periodic table (the alkaline earth metals and group 12 elements, formerly called groups IIA and IIB) and a nonmetal from group 16 (the chalcogens, formerly called group VI), as shown in Figure 2.8.

The II–VI semiconductors such as ZnO, ZnS, ZnSe, ZnTe, CdO, CdS, CdSe, and CdTe crystallize principally in the zinc blende and wurtzite structures and polymorphic modifications

between the two [12]. Bonding in II–VI compounds is a mixture of covalent and ionic types. This is because group-VI elements are considerably more electronegative than group II elements. The ionic character has the effect of binding the valence electrons rather tightly to the lattice atoms. Thus, the bandgaps of these compounds are larger than those of the covalent semiconductors of comparable atomic weights. Some of the II-VI compounds have n-type conductivity, others have p-type conductivity, and another set can have both types of conductivity. ZnO, CdO, CdS, CdSe and ZnS are of the n-type binary II–VI compounds ZnTe can be easily grown with p-type conductivity, while CdTe and ZnSe can be produced with both types of conductivity (n and p-type). The production of n-type CdTe is easy, while the production of p-type CdTe is not easy, and the production of n-ZnSe is difficult [13]–[16].

A major motivation to study II–VI semiconductors is their broad range of band gaps, and high effective mass. Most group II–VI materials are direct bandgap semiconductors with high optical absorption and emission coefficients. So a II-VI semiconductor of about 1 µm thickness is sufficient to absorb 99% of the impinging radiation with photon energy higher than the bandgap energy. Thus, they are well-suited for thin film optical devices, and the use of thin film II-VI compounds is an economically viable approach to the terrestrial utilization of solar energy [17].

Group → / ↓ Period	12	13	14	15	16
2		5 B	6 C	7 N	8 O
3		13 Al	14 Si	15 P	16 S
4	30 Zn	31 Ga	32 Ge	33 As	34 Se
5	48 Cd	49 In	50 Sn	51 Sb	52 Te
6	80 Hg	81 Tl	82 Pb	83 Bi	84 Po
7	112 Cn	113 Uut	114 Uuq	115 Uup	116 Uuh

Figure 2.8: II-VI semiconductor compounds.

2.4.2.2. Zinc oxide:

Zinc Oxide (ZnO) is a member of the II–VI semiconductor family with a hexagonal (wurtzite) structure as shown in Figure 2.9. It has large bandgap energy of 3.37 eV at room temperature, which makes it suitable for UV optoelectronic devices [3], it is easy to dope using various elements, it is thermally stable when doped with group III elements such as B [18], Al [19], Ga [20], and In [21] can be readily used as cation dopants to improve the optical properties of ZnO thin films. Among the various kinds of doped ZnO, B-doped ZnO (BZO) has recently been

extensively investigated because of its utilitarian application as a transparent conductive oxide [22] and its ferromagnetic properties [23].

Several methods such as metalorganic chemical vapour deposition [24] , molecular beam epitaxy [25], pulsed laser deposition [26], spray pyrolysis [27] and sol–gel spin coating [28] have been used to grow ZnO thin films. Among these, the sol–gel process presents an easy way to integrate ZnO devices into the Si technology, since it offers the possibility of excellent compositional control, multicomponent oxide layers of many compositions on substrate, simplicity, homogeneity, lower crystallization temperature and low production costs.

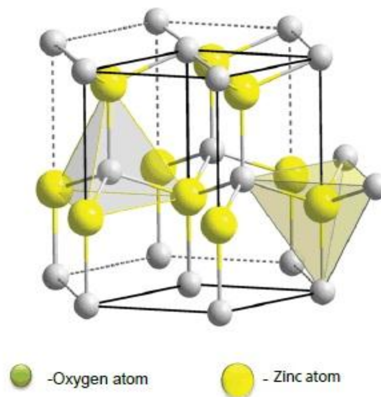

Figure 2.9: Zinc oxide crystal structure.

2.4.2.3. Cadmium oxide:

Cadmium oxide (CdO) is considered a promising material for photovoltaic applications due to its high electrical conductivity and optical transmittance in the visible region of solar spectrum [29]. CdO is one of the II–VI semiconductor family with cubic one structure (NaCl type), as shown in Figure 2.10, and a lattice parameter of 4.695 A and density 8000 kg/m^3. CdO is an n-type semiconductor with wide band gap, 2.5 eV [25, 26]. CdO optoelectrical properties can be controlled through doping with different metallic ions like In, Sn. Al, Sc, Tl, etc., which improves its electrical conduction and increases its optical bandgap [31]–[36].

CdO thin films have been prepared by various techniques such as sol–gel, DC magnetron sputtering, radio-frequency sputtering, spray pyrolysis, pulsed laser deposition, chemical vapor deposition, and chemical bath deposition [37]–[43].

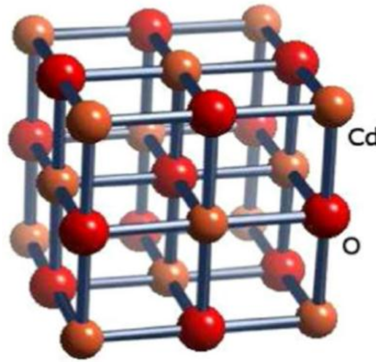

Figure 2.10: Cadmium oxide crystal structure.

Some structural optical and electrical properties are presented in Table 2.1.

Table 2.1: Some properties of CdO and ZnO thin films

Material	CdO		ZnO	
Structural properties:				
Crystal structure	Cubic (Rocksalt)	[44]	(Hexagonal Wurtzite)	[44]
Lattice constant :				
a (Å)	4.686	[44]	3.2495	[44]
c (Å)			5.2069	[44]
Grain size (nm)	18-20	[45]	28	[28]
Crystal density (g/cm^3)	6.252	[44]	6.05	[44]
Energy-band structure:				
Energy-band Gaps Eg(eV)	2.27	[4]	3.3	[28]
Effective Masse m^*/m_0	0.121	[46]	0.21	[48]
Electron Affinity	4.51	[47]	4.35	[49]
Electrical properties				
Carrier concentration n(cm^{-3})	4.4×10^{19}	[50]	5×10^{19}	[51]
Electrical resistivity	20×10^{-3}	[50]	5-10	[49]
Sheet resistance	3×10^{3}	[45]	10^{14}	[52]
Electron mobility	7.03	[50]	8	[2]

2.5. Defects in crystals:

A perfect crystal is an idealization; there is no such thing in nature. Atom arrangements in real materials do not follow perfect crystalline patterns. Nonetheless, most of the materials that are

useful in engineering are crystalline to a very good approximation. There is fundamental physical reason for this. The preferred structures of solids at low temperature are those that minimize the energy. The low-energy atomic configurations are almost invariably crystalline since the regular pattern of the crystal lattice repeats whatever local configuration is most favorable for bonding. There is also a fundamental physical reason why the crystal is imperfect. While a perfect crystalline structure may be preferred energetically, at least in the limit of low temperature, atoms are relatively immobile in solids and it is, therefore, difficult to eliminate whatever imperfections are introduced into the crystal during its growth, processing or use [53].

It is useful to classify crystal lattice defects by their dimension. The 0-dimensional defects affect isolated sites in the crystal structure, and are hence called point defects. An example is a solute or impurity atom, which alters the crystal pattern at a single point. The 1-dimensional defects are called dislocations. They are lines along which the crystal pattern is broken. The 2-dimensional defects are surfaces, such as the external surface and the grain boundaries along which distinct crystallites are joined together. The 3-dimensional defects change the crystal pattern over a finite volume. They include precipitates, which are small volumes of different crystal structure, and also include large voids or inclusions of second-phase particles [53].

2.5.1. Point defects:

Point defects (0-dimensional defects) are where an atom is missing or is in an irregular place in the lattice structure. Point defects are broadly classified into:

a. **Vacancies (intrinsic point defect):** are empty spaces where an atom should be, but is missing as shown in Figure 2.11. They are common, especially at high temperatures when atoms are frequently and randomly change their positions leaving behind empty lattice sites. In most cases diffusion (mass transport by atomic motion) can only occur because of vacancies [54].

b. **Self-interstitial (intrinsic point defect)**: is an extra atom that has crowded its way into an interstitial void in the crystal structure as shown in Figure 2.11. Self-interstitial atoms occur only in low concentrations in metals because they distort and highly stress the tightly packed lattice structure [54].

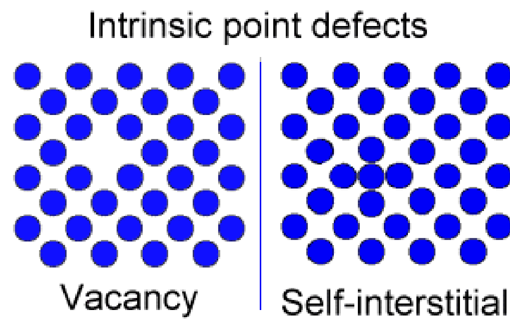

Figure 2.11: Schematic for vacancy and self-interstitial defects.

c. **Substitution impurity (extrinsic point defect)**: is an atom of a different type than the bulk atoms, foreign atom, which has replaced one of the bulk atoms in the lattice as shown in Figure 2.12. Substitutional impurity atoms are usually close in size (within approximately 15%) to the bulk atom. An example of substitutional impurity atoms is the zinc atoms in brass. In brass, zinc atoms with a radius of 0.133 nm have replaced some of the copper atoms, which have a radius of 0.128 nm [54].

d. **Interstitial impurity (extrinsic point defect):** are foreign atoms much smaller than the atoms in the bulk matrix as shown in Figure 2.12. Interstitial impurity atoms fit into the open space between the bulk atoms of the lattice structure. For example, Carbon atoms, with a radius of 0.071 nm, fit nicely in the open spaces between the larger (0.124 nm) iron atoms [54].

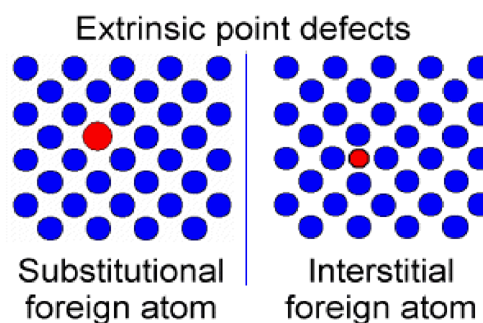

Figure 2.12: Schematic for Substitution and Interstitial defects.

a. **Frenkel defect:** When an ion is displaced from a regular lattice site to an interstitial site is called Frenkel defect as shown in Figure 2.13. Generally cations which are small in size are displaced to an interstitial site as the interstitial space is small .A Frenkel imperfection does not change the overall electrical neutrality of the crystal [54].

b. **Schottky defect:** A pair of one cation and one anion missing from the original lattice site on to the surface of the crystal so that charge neutrality is maintained in the crystal is called Schottky defect as shown in Figure 2.13 [54].

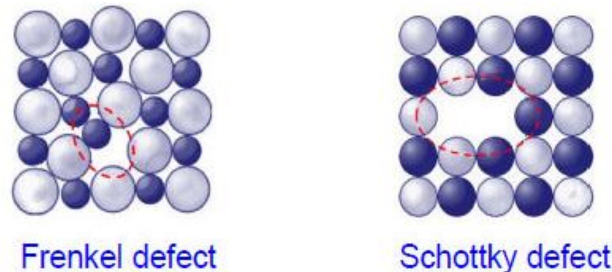

Figure 2.13: Schematic for Frenkel and Schottky defects.

2.5.2. Line defects:

Linear defects (1-dimensional defects) are defined as disturbed region between two perfect parts of a crystal. Linear defects are commonly called dislocations.

a. **Edge dislocation:**

A perfect crystal is composed of several parallel vertical planes which are extended from top to bottom completely and parallel to side faces as shown in Figure 2.14 (a). The atoms are in equilibrium positions and the bond lengths are in equilibrium value. If one of the vertical planes does not extend from top to bottom face of the crystal, but ends in midway within the crystal, then crystal suffers with a dislocation called edge dislocation. In imperfect crystal all the atoms above the dislocation plane are squeezed together and compressed there by the bond length decreases and all the atoms below the dislocation plane are elongated by subjecting to the tension and thereby the bond length increases [54].

b. **Screw dislocation:**

Atoms are displaced in two separate planes perpendicular to each other or defects forming a spiral around the dislocation line as shown in Figure 2.14 (b). A screw dislocation marks the boundary between slipped and unslipped parts of the crystal that can be produced by cutting the crystal partway and then sheering down one part relative to the other by atomic spacing horizontally [54].

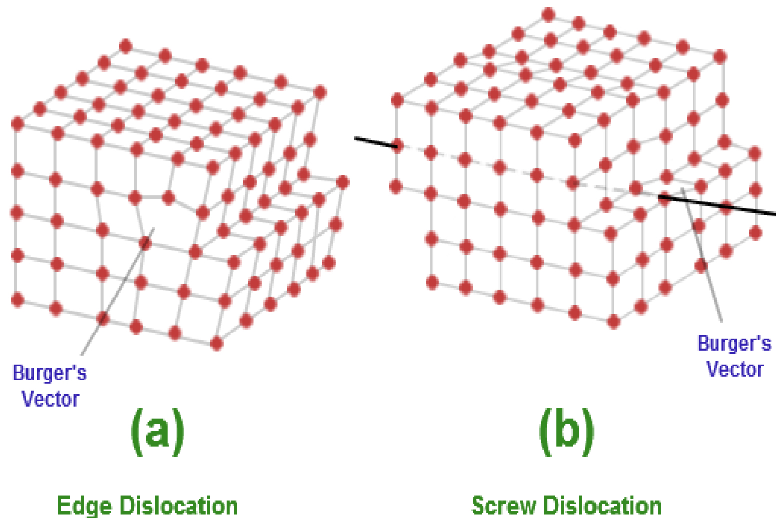

Figure 2.14: Schematic for line defects screw and edge dislocation.

2.5.3. Surface defects:

Surface defects (2-dimentinal defects) include external surfaces, grain boundaries, twins etc.

a. **External surface**: atoms on the surface are bonded to other atoms only on one side. Therefore the surface atoms have lower number of neighbours hence they have higher energy level. This makes it susceptible to erosion and corrosion [53], [54].

b. **Twin**: is defined as a region in which a mirror image for the structure exists across a plane or a boundary. This occurs when permanent deformation has taken place or during recrystallization (repositioning). Twin boundaries tend to strengthen a material [53], [54].

c. **Grain boundary:** are surface imperfections that separate grains of different orientations as shown in Figure 2.15. The grain boundary itself is a narrow region between two grains of about two to five atomic diameters in width and is a region of lower atomic packing because of atomic mismatch. Some atoms may also be in strained positions that raise the energy level at the boundary. The higher energy level makes it susceptible to nucleation and growth of precipitates. The lower atomic packing of the grain boundaries allows for more rapid diffusion of atoms in the grain boundary region [53].

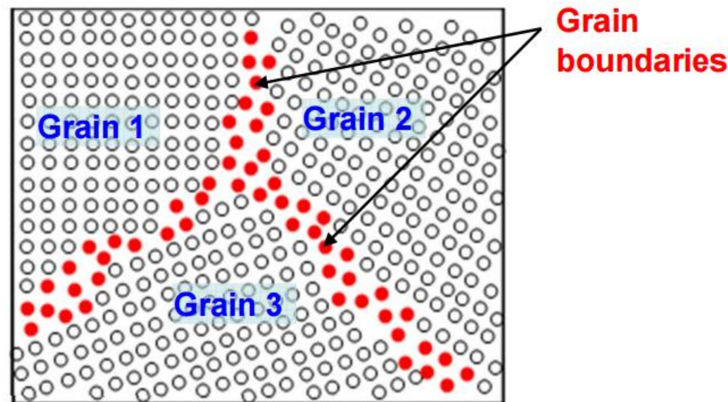

Figure 2.15: Schematic of orientation change across the grain boundary.

Polycrystalline semiconductor thin films usually consist of micrometer-sized columnar grains joined together at grain boundaries. The individual grains may or may not have a preferred crystallographic orientation which usually has no pronounced effects on the photovoltaic characteristics of the solar cell. The structural perfection of the grains depends on the condition of formation. Under optimized conditions, the interior of the grains is usually of good structural perfection with relatively low density of defects, such as dislocations and stacking faults. These defects at densities do not act as recombination centers and have negligible effects on junction characteristics and photovoltaic performance. However, the grain boundaries are highly disordered, and the periodicity in the crystal lattice is interrupted at the grain surface giving rise to a potential barrier. The potential barriers may affect the series resistance and open circuit voltage of the solar cell. Atoms at the grain surface may be bonded to impurities giving rise to a high density of surface states, which are effective recombination centers. The impurities along the grain boundaries may reduce the shunt resistance of the solar cell [2].

In thin film II-VI solar cells the photogeneration of carriers occurs mainly in the depletion region of the absorber due to the short optical absorption length and low carrier concentration in the absorber. In general, carriers generated closer to a grain boundary than the junction will have a much higher probability of recombination at the boundary than those generated closer to a junction. In II-VI compounds, the grain boundaries can be passivated, at least partially, by chemical treatments such as oxidation. Since the oxidation products are usually of n-type conductivity due to oxygen deficiencies, the surface of p-absorber grains are converted to n-type conductivity [2].

2.5.4. Volume defects:

Volume or Bulk defects (3-dimentinal defects) are introduced, usually, during processing and fabrication operations like casting, forming etc. E.g.: Pores, Cracks, Foreign particle. These defects act like stress raisers, thus affecting the mechanical properties of the parent solids. In some instances, foreign particles are added to strengthen the solid. Particles added act as hindrances to movement of dislocations thus increasing the strength [53], [54].

2.5.5. ZnO defects:

Before considering the defect structure of ZnO in more detail, it is important to realize that ZnO has a relatively open structure, with a hexagonal close packed lattice where Zn atoms occupy half of the tetrahedral sites. All the octahedral sites are empty. Hence, there are plenty of sites for ZnO to accommodate intrinsic (namely Zn interstitials) defects and extrinsic dopants [55].

The electronic energy levels of native imperfections in ZnO are illustrated in Figure 2.16. There are a number of intrinsic defects with different ionization energies. The Kröger Vink notation uses: i = interstitial site, Zn = Zinc, O = Oxygen and V = vacancy. The terms indicate the atomic sites, and superscripted terms indicate charges, where a dot indicates positive charge, a prime indicates negative charge, and a cross indicates zero charge, with the charges in proportion to the number of symbols [55].

Figure 2.16 shows that there are a number of defect states within the bandgap of ZnO. The donor defects are: $Zn_i^{\bullet\bullet}$, $Zn_i^{\bullet}$, Zn_i^{X}, $V_O^{\bullet\bullet}$, $V_O^{\bullet}$, V_0 and the acceptor defects are: V_{Zn}'', V_{Zn}'. The defect ionization energies vary from ~0.05-2.8 eV [56]. Zn interstitials and oxygen vacancies are known to be the predominant ionic defect types. However, which defect dominates in native, undoped ZnO is still a matter of great controversy [57].

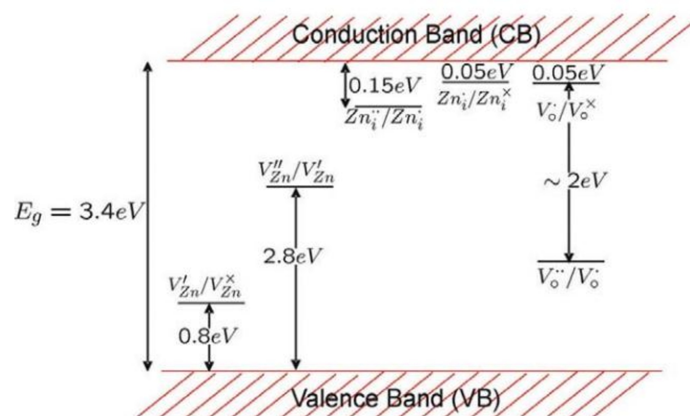

Figure 2.16: Energy levels of native defects in ZnO. The donor defects are $Zn_i^{\bullet\bullet}$, $Zn_i^{\bullet}$, Zn_i^{X}, $V_O^{\bullet\bullet}$, $V_O^{\bullet}$, V_O and the acceptor defects are V_{Zn}'', V_{Zn}'. (Adapted from Kröger [58]).

2.5.6. CdO defects:

It was found recently, based on experimental studies on the formation of defects in CdO, that, in contrast to ZnO, native defects are most likely oxygen vacancies [59], [60]. Furthermore, it was claimed that the electrical behavior of these defects is unified by a single energy level, the charge neutrality level, an idea which was already introduced in the late eighties [61]. At this energy level, the formation energy for creating donor and acceptor native defects is equal [62].

However, the vacancies in the experiment are not realized during the growth of the CdO sample, but by bombarding the sample with ions [59], [60]. The knocked-out oxygen and cadmium atoms form interstitial defects. The defect formation description that comes closer to the experimental situation is considering the formation energy of the co-formation of a cadmium vacancy, a cadmium interstitial and an oxygen vacancy together with an oxygen interstitial [62]. Therefore, the interstitial atoms will cluster together [60], the formation energy of a cadmium vacancy in its ground state (V_{Cd}^{2-}) together with a neutral Cd_i, and an oxygen vacancy in its ground state (V_O^{2+} and V_O^{+}, depending on E_F) together with a neutral oxygen interstitial, O_i. The formation energies as a function of the Fermi level are shown in Figure 2.17. The crossing between these different charge states of these double defects is found to be at 0.61 eV above the conduction band minimum [62].

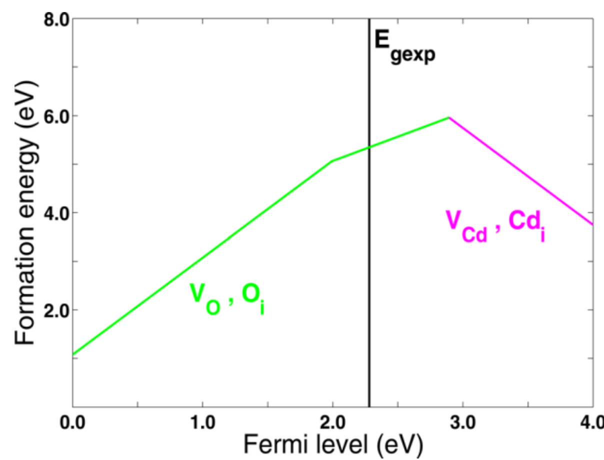

Figure 2.17: Formation energies as a function of the Fermi level in CdO for $V_O + O_i$ and $V_{Cd} + Cd_i$.

2.6. Basic semiconductor equations:

Years of research into device physics have resulted in a mathematical model that operates on any semiconductor device. This model consists of a set of fundamental equations, which link together the electrostatic potential and the carrier densities, within some simulation domain. These equations, which are solved inside any general purpose device simulator, have been derived from Maxwell's laws and consist of Poisson's Equation, the continuity equations and the transport equations. Poisson's Equation relates variations in electrostatic potential to local charge densities. The continuity and the transport equations describe the way that the electron and hole densities evolve as a result of transport processes, generation processes, and recombination processes.

2.6.1. Poisson's equation:

In a region where space charge exists (for example, in the junction), the *Poisson equation* is needed to link the electrostatic potential with the space charge density

$$div(\varepsilon \nabla \psi) = -\rho \qquad (2.20)$$

where ψ is the electrostatic potential, ε is the local permittivity, and ρ is the local space charge density.

The local space charge density is the sum of contributions from all mobile and fixed charges, including electrons, holes, and ionized impurities.

$$\rho = -q(p - n + N_D^+ - N_A^-) \qquad (2.21)$$

The electric field is obtained from the gradient of the potential.

$$\vec{E} = -\nabla \psi \qquad (2.22)$$

2.6.2. Carrier continuity equations:

The continuity equations for electrons and holes are defined by equations:

$$\frac{\partial n}{\partial t} = \frac{1}{q} divJ_n + G - R_n \qquad (2.23)$$

$$\frac{\partial p}{\partial t} = -\frac{1}{q} divJ_p + G - R_p \qquad (2.24)$$

where n and $p$are the electron and hole concentration, J_n and J_p are the electron and hole current densities, G_n and G_p are the generation rates for electrons and holes, R_n and R_p are the recombination rates for electrons and holes, and q is the magnitude of the charge on an electron.

2.6.3. The transport equations:

The current density equations, or charge transport models, are usually obtained by applying approximations and simplifications to the Boltzmann Transport Equation. The simplest model of charge transport that is useful is the Drift-Diffusion Model.

The current densities, approximated by a drift-diffusion model, in the continuity equations are expressed in terms of the quasi-Fermi levels ϕ_n and ϕ_p as:

$$\overrightarrow{J_n} = -q\mu_n n \nabla\phi_n \qquad (2.25)$$

$$\overrightarrow{J_p} = -q\mu_p p \nabla\phi_p \qquad (2.26)$$

where μ_n and μ_p are the electron and hole mobilities. The quasi-Fermi levels are then linked to the carrier concentrations and the potential through the two Boltzmann approximations

$$n = n_i \exp\left[q\frac{(\psi - \phi_n)}{kT}\right] \qquad (2.27)$$

$$p = n_i \exp\left[q\frac{(\psi - \phi_p)}{kT}\right] \qquad (2.28)$$

where n_i is the effective intrinsic concentration and T is the lattice temperature. These two equations may then be re-written to define the quasi-Fermi potentials:

$$\phi_n = \psi - \frac{kT}{q} ln\frac{n}{n_i} \qquad (2.29)$$

$$\phi_p = \psi + \frac{kT}{q} ln\frac{p}{n_i} \qquad (2.30)$$

By substituting these equations into the current density expressions, the following adapted current relationships are obtained:

$$\overrightarrow{J_n} = qD_n\nabla n - q\mu_n n\nabla\psi - \mu_n n\big(KT\nabla(ln\, n_i)\big) \qquad (2.31)$$

$$\overrightarrow{J_p} = -qD_p\nabla p - q\mu_p p\nabla\psi + \mu_p p\big(KT\nabla(ln\, n_i)\big) \qquad (2.32)$$

The final term accounts for the gradient in the effective intrinsic carrier concentration, which takes account of bandgap narrowing effects. Effective electric fields are normally defined whereby:

$$\vec{E}_n = -\nabla\left(\psi + \frac{kT}{q} lnn_i\right) \qquad (2.33)$$

$$\vec{E}_p = -\nabla\left(\psi - \frac{kT}{q} lnn_i\right) \qquad (2.34)$$

Which then allows the more conventional formulation of drift-diffusion equations to be written

$$J_n = q\mu_n nE + qD_n\nabla n \qquad (2.35)$$

$$J_p = q\mu_p pE + qD_p\nabla p \qquad (2.36)$$

where D_n and D_p are the electron and hole diffusion constants, and E is the electric field. The first term in each equation is due to drift in the electric field E, and the second term corresponds to carrier diffusion.

It should be noted that this derivation of the drift-diffusion model has tacitly assumed that the Einstein relationship holds. In the case of Boltzmann statistics this corresponds to:

$$D_n = \frac{kT}{q}\mu_n \qquad (2.37)$$

$$D_p = \frac{kT}{q}\mu_p \qquad (2.38)$$

Chapter 3: Solar cells

Chapter 3: Solar cells

3.1. Introduction:

Photovoltaic energy conversion in solar cells consists of two essential steps. First, absorption of light generates an electron-hole pair. The electron and hole are then separated by the structure of the device, electrons to the negative terminal and holes to the positive terminal, thus generating electrical power as shown in Figure 3.1 [63].

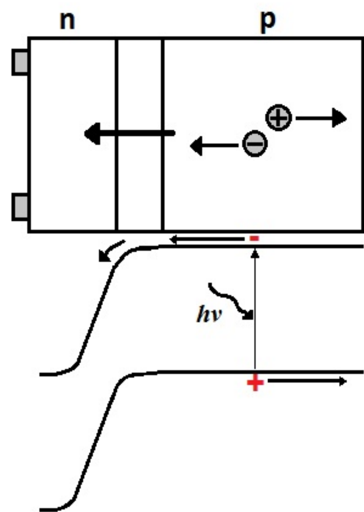

Figure 3.1: The bulk of the cell is formed by a thick p-type base where most of the incident light is absorbed and most power is generated.

3.2. Typical solar cell structures:

3.2.1. The p-n junction:

In order to understand all photovoltaic devices we require a basic understanding of the PN junction diode including the electrical contacts made to the diode. Originally the semiconductor diode was used to give current flow in one direction and current blocking in the other direction. PN junctions are formed by joining n-type and p-type semiconductor materials as shown in Figure 3.2. Since the n-type region has a high electron concentration and the p-type one has a high hole concentration, electrons diffuse from the n-type side to the p-type side. Similarly, holes

flow in the other side. In a PN junction, when the electrons and holes move to the other side of the junction, they leave behind exposed fixed charges on dopant atom sites. An electric field E forms between the n-type material and the p-type material and hence a "built in" potential V_{bi} is formed. A "depletion region" is formed since the electric field quickly sweeps free carriers out [9].

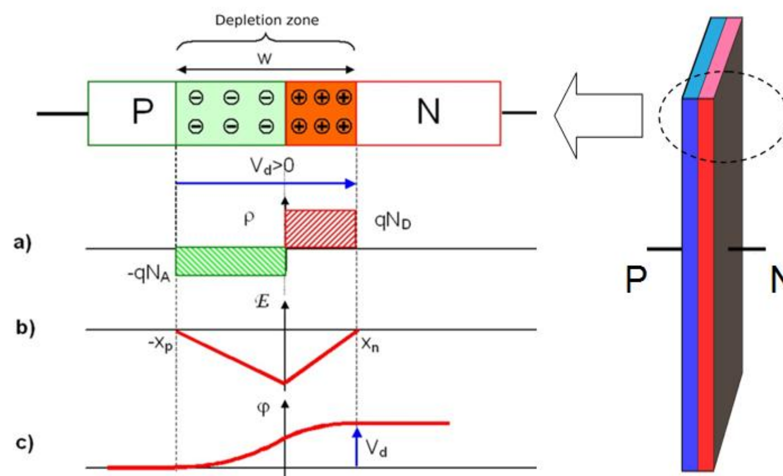

Figure 3.2: Formation of a PN junction in the Schottky approximation. (a) space-charge distribution due to fixed ionized dopants; (b) electric field obtained by integration of the Poisson equation; (c) a second integration step results in the electrostatic potential.

Even with the presence of a barrier created by the electric field, some carriers still cross the junction by diffusion. Some carriers will have a high velocity and travel in an enough net direction such that they cross the junction. Once a majority carrier crosses the junction, it becomes a minority carrier. It will continue to diffuse away from the junction and can travel a distance on average equal to the diffusion length before it recombines and caused the “diffusion current”. In the other hand minority carriers which attain the edge of the diffusion region are swept across it by the electric field in the depletion region and this is the “drift current”. As a result in equilibrium, the net current from the PN junction is zero [9].

3.2.2. The p-n junction solar cell:

The planar p-n junction solar cell under low injection is usually singled out for special analysis since realistic approximations exist that allow analytic solutions to be developed and used successfully for the description of practical devices. The success of this model is due, to a large

extent, on the clear way the cell can be divided into three regions - emitter, junction region and base - which serve a different purpose in solar cell operation. The emitter and base - which remain largely neutral during the cell operation - absorb the main part of the incident light and transport the photogenerated minority carriers to the junction. The p-n junction - which contains a strong electric field and a fixed space charge - separates the minority carriers that are collected from the emitter and base. The junction is effectively devoid of mobile charge carriers and is sometimes called the depletion region [63].

In operation, the Fermi level E_F splits into two quasi-Fermi levels E_F, and E_{Fp}, one each for the electrons and holes, with the corresponding potentials $\phi n = - q/E_{Fn}$, and $\phi p = -q/E_{Fp}$. Near the open circuit, the quasi-Fermi levels are parallel in the junction, their gradients are small, and their splitting is equal to the observed voltage at the junction, see Figure 3.3.

Under illumination or under applied bias in the dark, the electrostatic potential difference $\Delta\psi$ between the two sides of the junction is a difference of two terms: the equilibrium built-in voltage V_{bi} and the voltage V at the junction edges [63]:

$$\Delta\psi = V_{bi} - V \quad (3.1)$$

$$qV_{bi} = k_B T ln \frac{N_D N_A}{n_i^2} \quad (3.2)$$

Where N_A and N_D are the acceptor and donor concentrations on the p and n-sides of the junction, respectively. In the absence of resistive losses, V is equal to the voltage measured at the terminals of the cell. The junction width Wj is given by [63],

$$W_j = L_D \sqrt{\frac{2q\Delta\psi}{k_B T}} \quad (3.3)$$

Here, L_D is the Debye length [64],

$$L_D = \sqrt{\frac{\varepsilon k_B T}{q^2 N_B}} \quad (3.4)$$

where ε is the static dielectric constant.

In an ideal p-n junction solar cell, the junction (or depletion) region serves as a lossless mechanism for extracting and separating the minority carriers from the quasi-neutral regions - the base and the emitter. The function of the junction can then be summarised in the form of boundary conditions which link the majority carrier concentration on one side of the junction with the minority carrier concentration on the other [63].

The photogenerated and dark saturation currents for the cell are obtained by adding the relevant quantities for the base and the emitter:

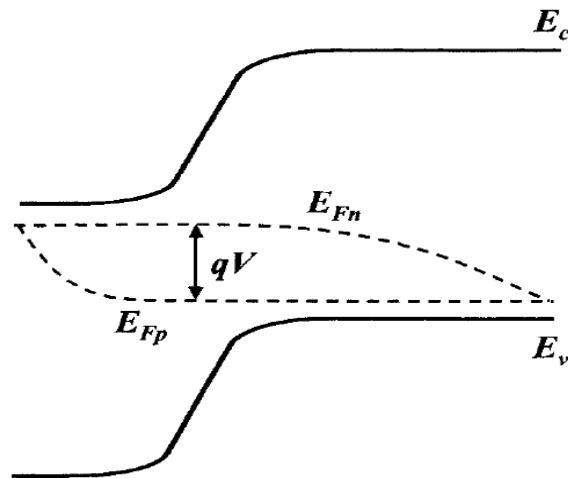

Figure 3.3: The p-n junction at open circuit.

$$I_{ph} = I_{ph} + I_{phe} \quad \text{and} \quad I_0 = I_{0b} + I_{0e} \tag{3.5}$$

No recombination occurs in an ideal p-n junction but the (small) light generated current produced here can be added to the first Eq. (3.5). Recombination is included in more realistic analytical theories: the original treatment uses the Shockley-Read-Hall model of recombination via defects; with the principal result that the current is reduced by a term of the form $I_{02}(\exp(qV/2k_BT) - 1)$ [65].

3.2.3. Homojunction and Heterojuction:

Junctions between two semiconductor materials can be classified into Homojunction, these are the PN junctions of identical semiconductors, and Heterojunction. This latter is formed by two different semiconducting materials with unequal band gaps. The behavior of a semiconductor junction depends crucially on the alignment of the energy bands at the interface [66]. Semiconductor interfaces can be organized into three types of Heteronjuction as shown in Figure 3.4 [64], [66].

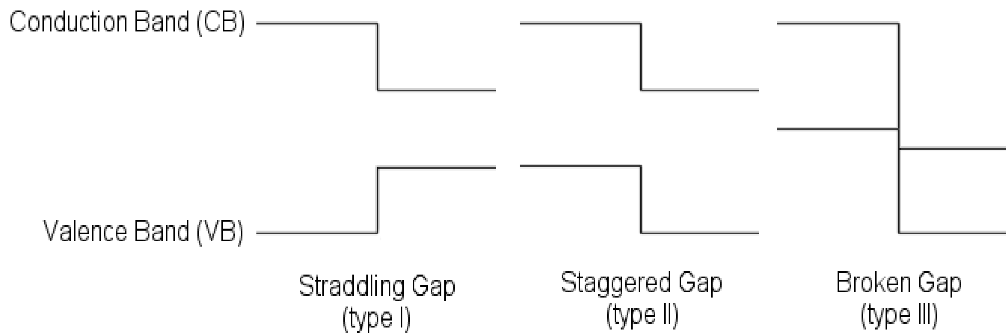

Figure 3.4: The three types of semiconductor Heterojuction organized by band alignment.

To construct the energy band diagrams of a Heteronjuction, we use the Anderson's rule called electron affinity rule. The vacuum levels of the two semiconductors on either side of the Heterojuction should be aligned (at the same energy). Once the vacuum levels are aligned it is possible to use the electron affinity and band gap values for each semiconductor to calculate the conduction band and valence band offsets. The electron affinity (χ) gives the energy difference between the lower edge of the conduction band and the vacuum level of the semiconductor. The band gap (E_g) gives the energy difference between the lower edge of the conduction band and the upper edge of the valence band. For semiconductor alloys it may be necessary to use Vegard's law to calculate these values see Figure 3.5. [63], [64], [66].

Anderson's rule allows the calculation of the band offsets of both the valence band (ΔE_V) and the conduction band (ΔE_C). After applying Anderson's rule and discovering the bands' alignment at the junction, Poisson's equation can then be used to calculate the shape of the band bending in the two semiconductors [66].

$$\Delta E_c = \chi_2 - \chi_1 \qquad (3.6)$$

Next, suppose that the band gap of semiconductor 2 is large enough that the valence band of semiconductor 1 lies at a higher energy than that of semiconductor 2. Then the valence band offset is given by [66]:

$$\Delta E_v = (\chi_1 + E_{g1}) - (\chi_2 + E_{g2}) \qquad (3.7)$$

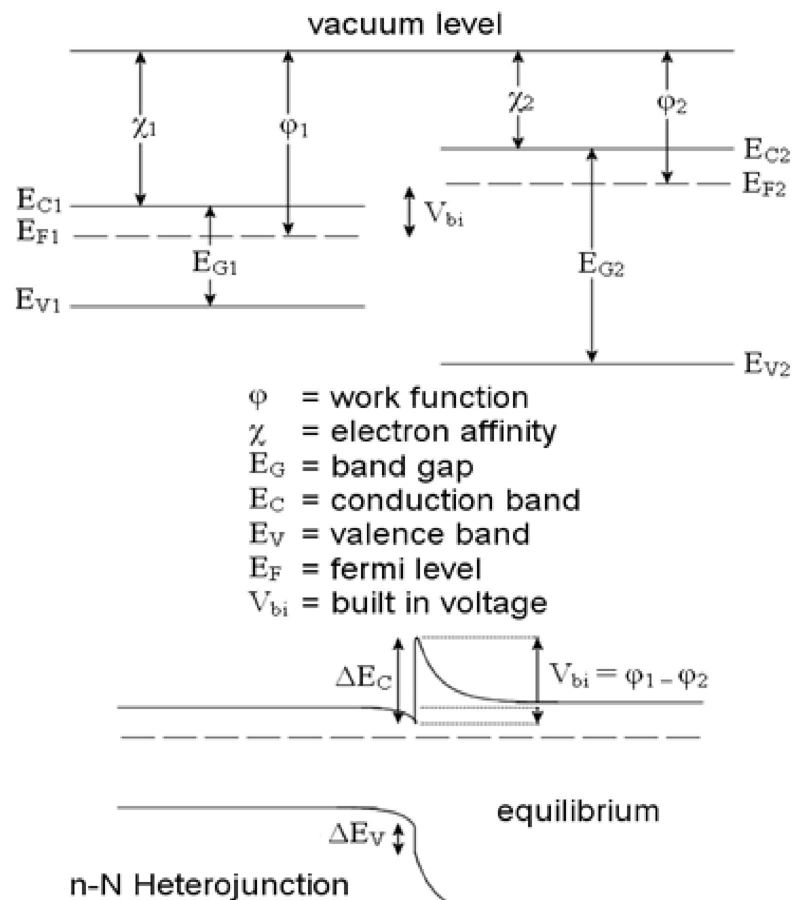

Figure 3.5: Band diagrams for straddling-gap Heterojuction.

3.3. Electrical characteristics:

3.3.1. The ideal solar cell:

An ideal solar cell can be represented by a current source connected in parallel with a rectifying diode, as shown in the equivalent circuit of Figure 3.6.

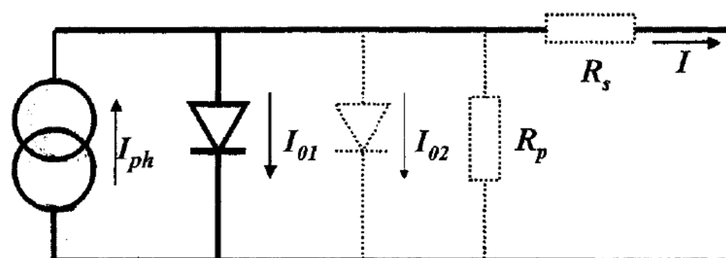

Figure 3.6: The equivalent circuit of an ideal solar cell (full lines). Non-ideal components are shown by the dotted line.

The corresponding I-V characteristic is described by the Shockley solar cell equation [63],

$$I = I_{ph} - I_0 \left(e^{\frac{qV}{k_B T}} - 1 \right) \quad (3.8)$$

where k_B is the Boltzmann constant, T is the absolute temperature, q (>0) is the electron charge, and V is the voltage at the terminals of the cell. I_0 is well known to electronic device engineers as the diode saturation current.

Figure 3.7 shows the I-V characteristics of a solar cell. In the ideal case, the short circuit current I_{sc} is equal to the photogenerated current I_{ph}, and the open circuit voltage V_{oc} is given by [63],

$$V_{oc} = \frac{k_B T}{q} ln\left(1 + \frac{I_{ph}}{I_0}\right) \quad (3.9)$$

The power P = IV produced by the cell is shown in Figure 3.8. The cell generates the maximum power P_{max} at a voltage V_m and current Ira, and it is convenient to define the fill factor FF by [64],

$$FF = \frac{I_m V_m}{I_{sc} V_{oc}} = \frac{P_{max}}{I_{SC} V_{OC}} \quad (3.10)$$

The fill factor FF of a solar cell with the ideal characteristic Eq. (3.8) will be furnished by the subscript 0. It cannot be determined analytically but it can be shown that FF_0 depends only on the ratio $v_{oc} = V_{oc}/k_B T$. FF_0 is determined, to an excellent accuracy, by the approximate expression [63],

$$FF_0 = \frac{v_{oc} - ln(v_{oc} + 0.72)}{v_{oc} + 1} \quad (3.11)$$

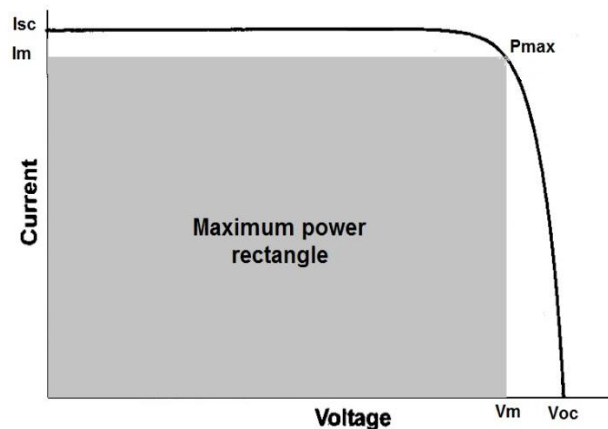

Figure 3.7: The I-V characteristics of a solar cell. The power generated at the maximum power point is equal to the shaded rectangle.

The power generated at the maximum power point is equal to the blue rectangle in Figure 3.8.

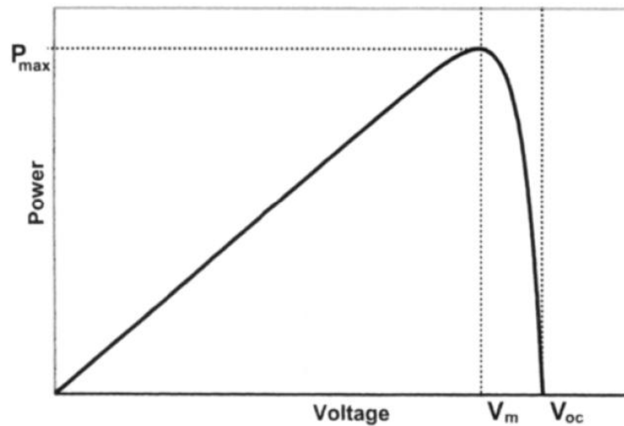

Figure 3.8: The power produced by solar cell.

The I-V characteristics of an ideal solar cell complies with the superposition principle; the functional dependence, Eq. (3.8), can be obtained from the corresponding characteristic of a diode in the dark by shifting the diode characteristic along the current axis by I_{ph} (Figure 3.9).

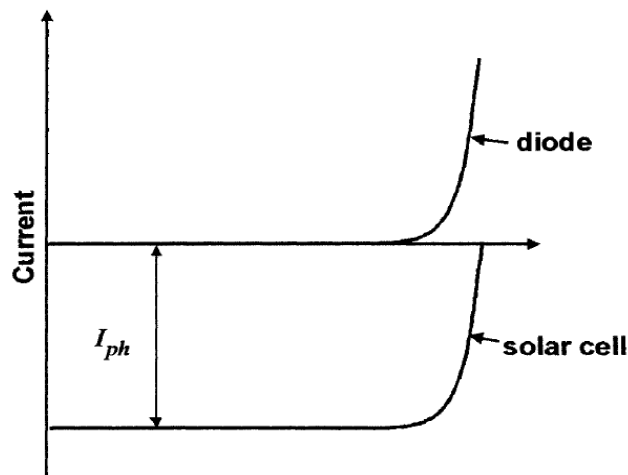

Figure 3.9: The superposition principle for solar cells.

3.3.2. Reel solar cell characteristics:

The I-V characteristic of a solar cell in practice usually differs to some extent from the ideal characteristic Eq. (3.8). A two-diode model is often used to fit an observed curve, with the second diode containing an ideality factor of 2 in the denominator of the argument of the exponential term.

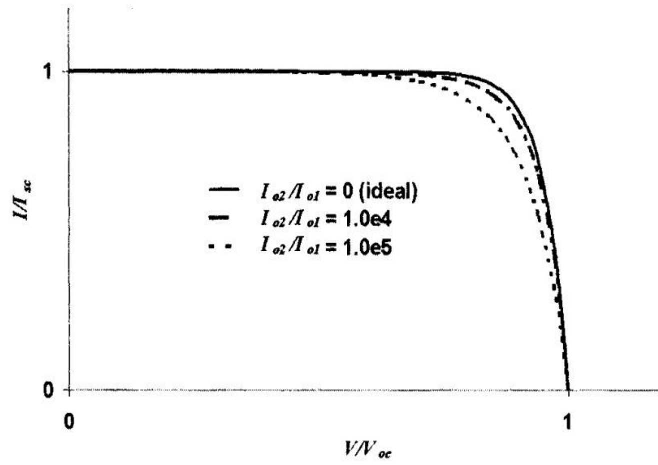

Figure 3.10: The I-V characteristic of the solar cell in the two diode model for three values of the ratio I_{02}/I_{01}.

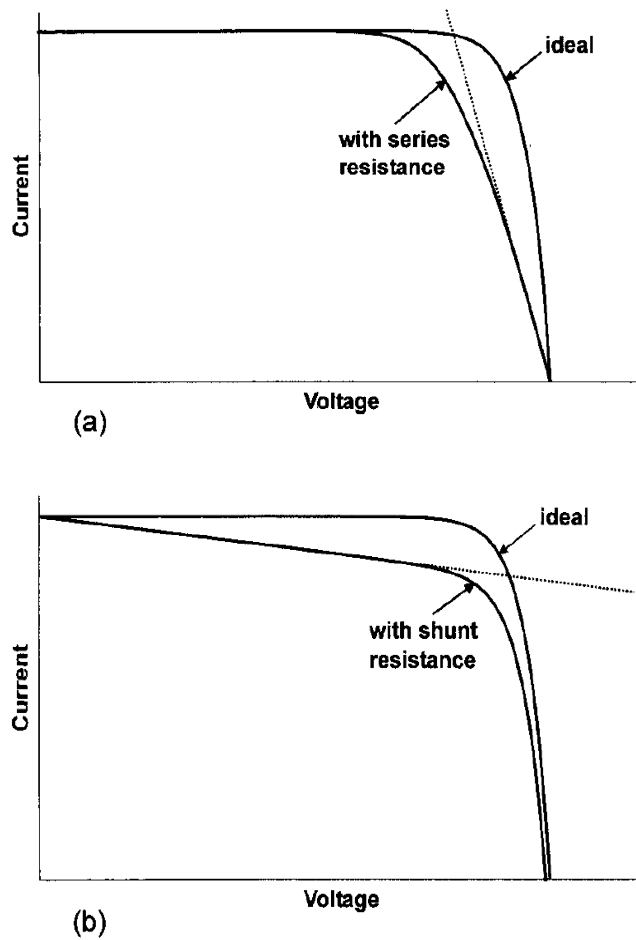

Figure 3.11: The effect of the series resistance (a) and parallel resistance (b) on the I-V characteristic of the solar cell.

The solar cell (or circuit) may also contain series (R_s) and parallel (or shunt, R_p) resistances, leading to a characteristic of the form [63],

$$I = I_{ph} - I_{01}\left\{exp\left(\frac{V+IR_s}{k_BT}\right) - 1\right\} - I_{02}\left\{exp\left(\frac{V+IR_s}{2k_BT}\right) - 1\right\} - \frac{V+IR_s}{R_p} \qquad (3.12)$$

where the light-generated current I_{ph} may, in some instances, depends on the voltage, as we have already noted. These features are shown in the equivalent circuit of Figure 3.6 by the dotted lines. The effect of the second diode, and of the series and parallel resistances, on the I-V characteristic of the solar cell is shown in Figures 3.10 and 3.11, respectively. The effect of the series resistance on the fill factor can be allowed for by writing [63],

$$FF = FF_0(1 - r_s) \qquad (3.13)$$

where $r_s = R_s\, I_{sc}/V_{oc}$. An analogous expression exists also for the parallel resistance.
Further information about these parameters can be obtained from the dark characteristic (Figure 3.12).

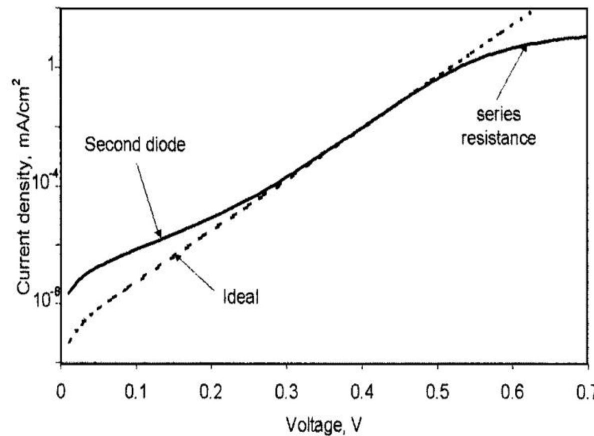

Figure 3.12: The dark I-V characteristic of a solar cell for the two-diode model including the series resistance.The shunt resistance has a similar effect to the second diode.

3.4. The quantum efficiency:

The quantum efficiency of a solar cell is defined as the ratio of the number of electrons in the external circuit produced by an incident photon of a given wavelength. Thus, one can define external and internal quantum efficiencies (denoted by *EQE(λ)* and *IQE(λ),* respectively). They differ in the treatment of photons reflected from the cell: all photons impinging on the cell

surface are taken into account in the value of the *EQE* but only photons that are not reflected are considered in the value of *IQE* [63].

If the internal quantum efficiency is known, the total photogenerated current is given by,

$$I_{ph} = q \int_{(\lambda)} \Phi(\lambda)\{1 - R(\lambda)\} IQE(\lambda) d\lambda \qquad (3.14)$$

where $\Phi(\lambda)$ is the photon flux incident on the cell at wavelength λ, $R(\lambda)$ is the reflection coefficient from the top surface and the integration is carried out over all wavelength λ of light absorbed by the solar cell. The values of the internal and external quantum efficiency are routinely measured to assess the performance of a solar cell by using interference filters or monochromators.

3.5. II-VI thin film solar cells:

3.5.1. The use of II-VI thin films in solar cells:

II-VI thin film solar cells have been under investigation for about 40 years. All efficient devices are of the heterojunction configuration because of the difficulty in forming a very shallow junction (less than 0.1 μm) with a high conductivity surface layer, and the surface recombination effects. The two semiconductors of opposite conductivity type in a heterojunction solar cell are usually referred to as the "absorber" (bandgap energy Eg_1), and "collector" or "window" (bandgap energy Eg_2), respectively, with $Eg_2 > Eg_1$. The radiation is incident on the surface of the window, and the generation of hole-electron pairs by photons with energies between Eg_2 and Eg_1, occurs in the absorber. A portion of the radiation with photon energy greater than Eg_2 may also reach the absorber, depending on the thickness and absorption coefficient of the window. Since the wide gap semiconductors for windows are usually of n-type conductivity, the absorber is p-type. The photocurrent consists predominately of the electrons generated in the depletion region in the absorber. In practice, the heterojunction solar cells may be classified into frontwall cells and backwall cells according to the manner in which the solar radiation impinges on the cell [2].

A number of binary and ternary II-VI compounds have been used as windows and as absorbers in thin film solar cells. On the basis of the bandgap energy, CdO, CdS, ZnO, ZnS, ZnSe and certain ternaries are potential window materials, and CdSe, CdTe, and some ternaries, may be used as absorbers [2].

3.5.2. Characterization of II-VI thin film solar cells:

To characterize a II-VI thin film solar cell, all important diode and photovoltaic parameters should be evaluated. Shunt resistance (R_{sh}), series resistance (R_s), and diode quality factor (*A*) are most important parameters affecting the photovoltaic characteristics. These parameters are all illumination dependent. Low R_{sh} leads to reduction in V_{oc}, and FF. Large R_s, results in decreased FF and V_m. Large A value leads to reduction in V_{oc}, and FF. The A value of thin film cells is always greater than unity in the dark due to carrier recombination; it increases under illumination and increases with decreasing temperature . R_{sh}, and R_s, can be deduced from the J-V relation of the solar cell at low bias and high bias, respectively. From the R_{sh}, and R_s, measured in the dark, A and J_0, can be deduced from the diode equation. Under illumination, A can be deduced from the photodiode equation using the technique developed by Sites and Mauk [67].

Chapter 4: Experimental and simulation methods

Chapter 4: Experimental and simulation methods

4.1. Introduction:

The reliability and validity of simulation results must be performed by comparing them with those obtained in experimental studies. Otherwise, obtained simulation results are undermined and called into question, and it is neither possible nor feasible to reuse them in constructing real devices such as solar cells. In that reason, we will model the studied materials by using our own experimental results. In this section we will illustrate, briefly, the experimental method used to prepare the studied materials then the simulation method which used to model them.

4.2. Experimental method:

There is a great deal of work reported for II-VI thin films formation using various techniques, including DC magnetron sputtering, chemical vapor deposition, molecular beam epitaxy, pulsed laser deposition, radio-frequency sputtering, spray pyrolysis and sol–gel [20–24, 33–39]. Among these techniques, the sol–gel method is considered to be one of the simplest and most economical for thin film fabrication [68].

4.2.1. Sol-gel:

Sol-gel process is a method for producing solid materials from small molecules. The method is used for the fabrication of thin films, especially metal oxides. Spin coating and dip coating are two basic techniques used to deposit sol-gel coatings. Spin coating produces a one-sided coating, while dip coating yields a double-sided coating. Both techniques are used in manufacturing to make different coatings and thin films [69], [70].

4.2.1.1. Spin coating:

Spin coating is used for many applications where relatively flat substrates or objects are coated with thin layers of material. For example, several cathode ray tube (CRT) manufacturers use the spin coating method to make anti-glare or anti-reflection coatings. In spin coating, the material to

be made into coating is dissolved or dispersed into a solvent, and this coating solution is then deposited onto the surface and spun off to leave a uniform layer for subsequent processing stages and ultimate use [71].

There are four key stages in spin coating process, as shown in Figure 4.1;

1. Deposition: The deposition of the coating fluid onto the substrate
2. Spin-up: Aggressive fluid expulsion from the substrate surface by the rotational motion
3. Spin-off: Gradual fluid thinning
4. Evaporation: Coating thinning by solvent evaporation

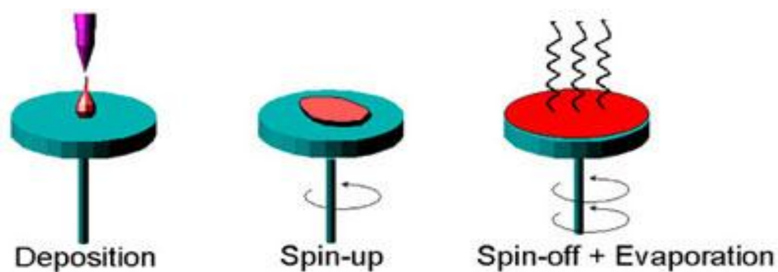

Figure 4.1: Schematic of spin coating process.

4.2.1.2. Dip Coating:

Dip coating is a process where the substrate to be coated is immersed in a liquid and then withdrawn with a well-defined withdrawal speed under controlled temperature and atmospheric conditions. Vibration-free mountings and very smooth movement of the substrate is essential for dip systems. An accurate and uniform coating thickness depends on precise speed control and minimal vibration of the substrate and fluid surface [71]. The coating thickness is mainly defined by the withdrawal speed, the solid content and the viscosity of the liquid as shown in Figure 4.2.

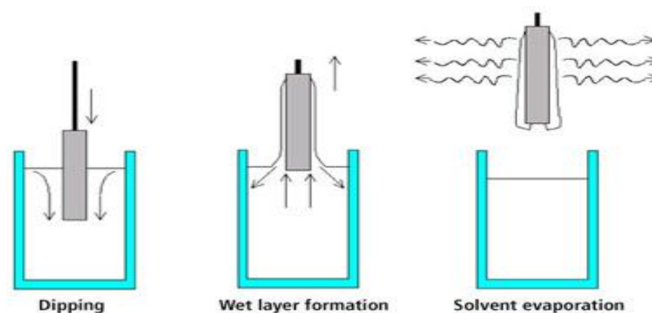

Figure 4.2: Schematic of dip coating process.

The studied CdO and ZnO thin films were prepared by sol gel technique at Firat University, Elazig, Turkey.

4.2.2. CdO thin film:

4.2.2.1. Preparation of CdO thin film:

For the synthesis the cadmium oxide thin films, 0.5M of cadmium acetate dehydrate ($Cd(CH_3COO)_2.2H_2O$) was firstly dissolved in 2-metoxyethanol for 2h at room temperature and then, the monoethanolamine was added to this solution. The molar ratio of monoethanolamine to cadmium acetate dehydrate was taken as 1.0. The prepared mixture was stirred using magnetic stirrer for about 30 min to obtain clear homogeneous solution and then sol was kept for aging for 24h prior to film deposition. In order to remove the native oxide on surface, the substrate was etched by HF and then it was rinsed in deionized water using an ultrasonic bath for 10–15 min. After cleaning process, CdO film was deposited on the substrate by sol–gel method and then, the film was dried at 150◦C for 10 min onto a hot plate to evaporate the solvent and remove organic residuals. The prepared CdO film was annealed at 450◦C for 1h in a furnace [4].

4.2.2.2. Fabrication of CdO/p-Si solar cell:

The semiconductor used to fabricate the diode in this study was p-type single crystal silicon with a thickness of 600 μm, and a resistivity of 5–10 Ωcm. CdO film was deposited on p-type-silicon by sol–gel dip coating method. The thickness of the CdO film was determined to be 187 nm using atomic force microscopy. Al metal front contacts were formed on CdO film in the form of circular dots of 2 mm in diameter and 100 nm in thickness. The back ohmic contact was formed by evaporating Al metal on the back of Si wafer. The cross-section of Al/CdO/p-Si/Al diode is shown in Figure 4.3. It has to be mentioned that the CdO film plays a double role: as a TCO window as well as the emitter of the n-p junction. Further details of the fabrication process and electrical and optical characterization of the solar cell material and device can be found in [4].

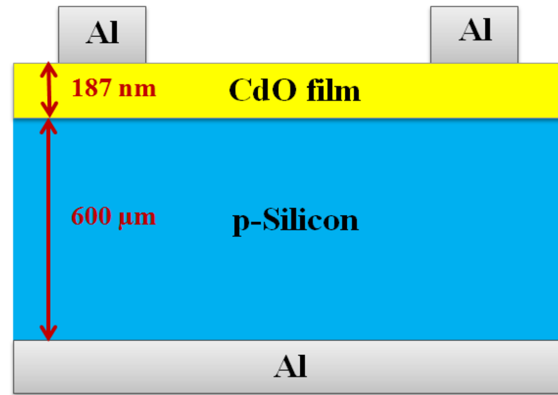

Figure 4.3: A two dimensional schematic representation of the cross-section of the Al/CdO/p-Si/Al solar cell.

4.2.3. ZnO thin film:

4.2.3.1. Preparation of ZnO thin film:

ZnO thin films were developed by sol–gel spin coating method. Before forming a ZnO layer on the glass substrate, the native oxide on the front surface of the substrate was removed in HF:H_2O (1:10) solution, then, the wafer was rinsed in DI water. To obtain the sol, the precursor zinc acetate dehydrate was first dissolved into 2-methoxyethanol as a solvent and by adding monoethanolamine, which acts as the stabilizer. Molar ratio of monoethanolamine to zinc acetate was maintained at 1:1 and the concentration of zinc acetate was 0.3M. After stirring for 1h, a clear and homogeneous solution was obtained. The substrate was placed on the sample holder and was rotated at a speed of 3000 rpm for 30 s. After each spin coating the substrate was dried in a furnace at 300 C for 10 min to evaporate the solvents. After this process was repeated 10 times, the ZnO film was annealed at 450 C for 1 h.

4.2.3.2. Fabrication of ZnO/p-Si solar cell:

Single crystal Si (100) substrate was used for deposition of ZnO thin film. An ultrasonic bath for 20 min with acetone and 20 min with IPA was given to the substrates in order to make them free of any contamination and gas residues on the surface. Uniform thin film was deposited by spin coating at 3,000 rpm for 30 s; thickness of around 150 nm was achieved in this way. The sample was dried at room temperature for 24 h and was then subjected to heat treatment at different temperatures for varying times. After solar cell was fabricated, Al was used as an ohmic contact

to p-type single crystal Si substrate. There was no grid contact at the front, rather the ZnO film was point- probed in order to measure the current-voltage characteristics of this device. The cross-section of ZnO/p-Si/Al diode is shown in Figure 4.4. It has to be mentioned that the ZnO film plays a double role: as a TCO window as well as the emitter of the n-p junction. Further details of the fabrication process and electrical and optical characterization of the solar cell material and device can be found in [5].

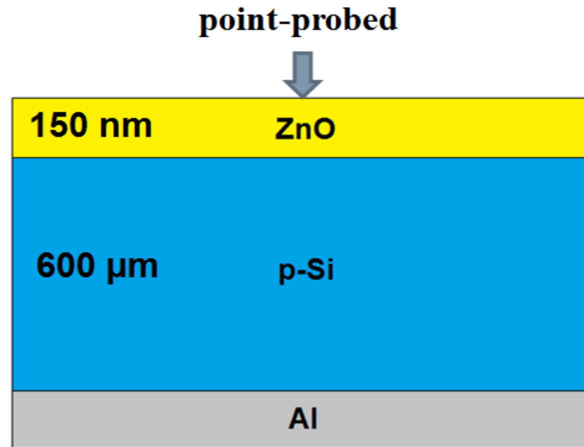

Figure 4.4: A two dimensional schematic representation of the cross-section of the ZnO/p-Si/Al diode.

4.2.4. Characterization equipment

The characterization of materials is important for understanding their properties and applications. The technique adopted to characterize the studied samples is UV-Vis-NIR Spectrophotometry.

4.2.4.1. Spectrophotometry (UV-Vis-NIR)

One of the most basic methods to investigate the properties of materials through their interaction with light, also the most natural to us, is to measure how much light is reflected, transmitted or absorbed by that material. A material absorbs light when the incident photons create atomic or charge movements in the material. If we measure that absorption as a function of photon energy, we can get an insight into its electronic and atomic structure. Note that morphology, stress, temperature, contact with other materials, etc. all may affect the materials phonons and electrons transitions and will modify the materials light absorption in many cases. While this is useful,

allowing us to know more about the material's properties through the measurement of its absorption spectrum, all these variables must be controlled or monitored when performing the measurements. Spectrophotometry is one of the most popular modalities of spectroscopies that measure the intensity of transmitted and reflected light. The typical spectral range covered by high-end commercialspans fromthenear ultra-violet (λ~200 nm) to the near infra-red (λ~3 μm). This is the reason many use the term UV-VIS to designate spectrophotometry (the technique), or the spectrophotometer (the instrument) [72].

4.2.4.2. Instrumentation

There is a wide variety of spectrophotometers in the market, from cheaper single beam models with limited spectral range and measurement capabilities to expensive double beam models featuring multiple light sources and detectors, capable of a wider spectral range and supporting a more diverse set of accessories for a variety of experiments and different types of samples. The most commonly used higher end instruments consist, typically, of a couple light sources, a diffraction grating based monochromator, a sample chamber and one or more detectors. Shown in Figure 4.5 is the schematic diagram of a simple dual beam spectrophotometer. Several accessories are available for the higher end spectrophotometers, which enable performing different modalities of measurement on different types of samples, as for example, solid films, liquid solutions, powders, etc. Some of the modalities commonly available are transmittance, diffuse transmittance, diffuse and specular reflectance, and variable angle specular reflectance. Instruments equipped with two beams allow for the measurement of a reference sample simultaneously with the test sample. Even if no reference sample is used, the reference beam is useful to compensate for possible slow fluctuations of the source intensity or conditions of the detectors that could affect their response [72].

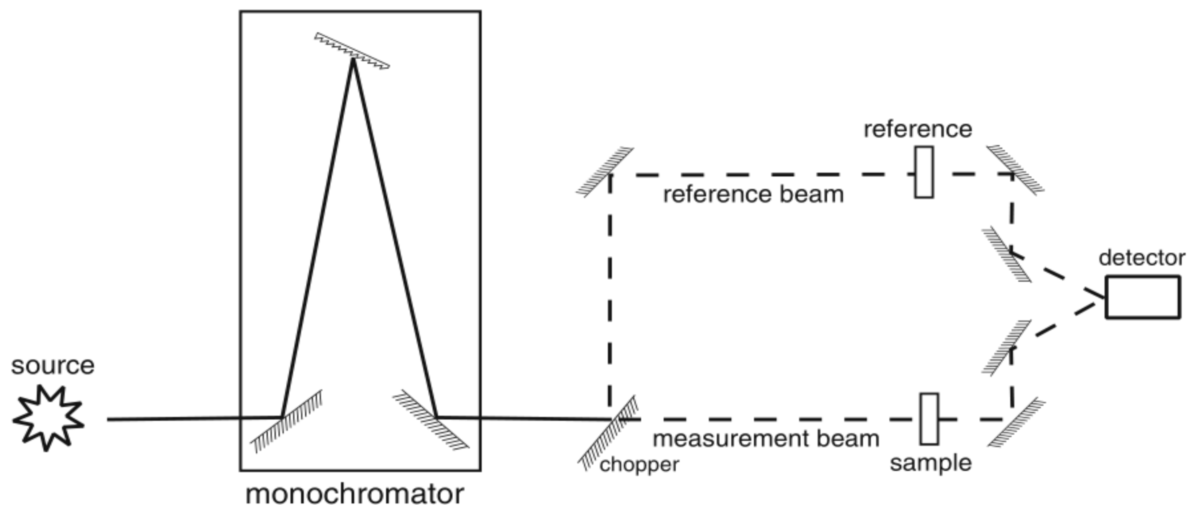

Figure 4.5: Schematic diagram of a dual beam spectrophotometer operating in transmittance mode

The optical transmittance spectra of the investigated samples, CdO and ZnO, were performed using a Shimadzu UV–vis–NIR 3600 spectrophotometer, Figure 4.6, at Firat University Elazig, Turkey.

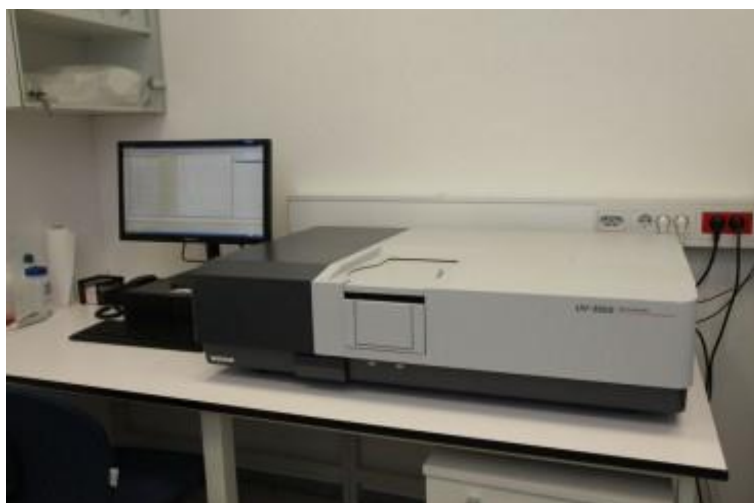

Figure 4.6: Shimadzu UV–vis–NIR 3600 spectrophotometer.

4.3. Simulation method:

Solar cell simulation and modeling are fundamental to a detailed understanding of the device operation, and a comprehensive model requires a detailed knowledge of the material parameters. Numerous computer programs that use the material parameters to model solar cell operation have been developed over the years, and several are now available commercially [63]:

- **PC1D** developed by P.A. Basore and colleagues at the University of New South Wales, Australia, is the standard one-dimensional simulator used by the PV community.

- **MEDICI** by Technology Modelling Associates models the two-dimensional distribution of potential and carrier concentration in a semiconductor device. It also includes an Optical device advanced application module where photogeneration can be computed for multi-spectral sources.

- **ATLAS**, a Device Simulation Software by SILVACO International, uses physical models in two and three dimensions. It includes the Luminous tool which computes ray tracing and response of solar cells. It allows the use of monochromatic or multi-spectral sources of light.

4.3.1. ATLAS (by SILVACO):

Atlas is a physically-based two and three dimensional device simulator. It predicts the electrical behavior of specified semiconductor structures and provides insight into the internal physical mechanisms associated with device operation [73].

4.3.2. Atlas inputs and outputs:

Figure 4.7 shows the types of information that flow in and out of Atlas. Most Atlas simulations use two input files. The first input file is a text file that contains commands for Atlas to execute. The second input file is a structure file that defines the structure that will be simulated [73].

Atlas produces three types of output files. The first type of output file is the run-time output, which gives you the progress and the error and warning messages as the simulation proceeds. The second type of output file is the log file, which stores all terminal voltages and currents from

the device analysis. The third type of output file is the solution file, which stores 2D and 3D data relating to the values of solution variables within the device at a given bias point [73].

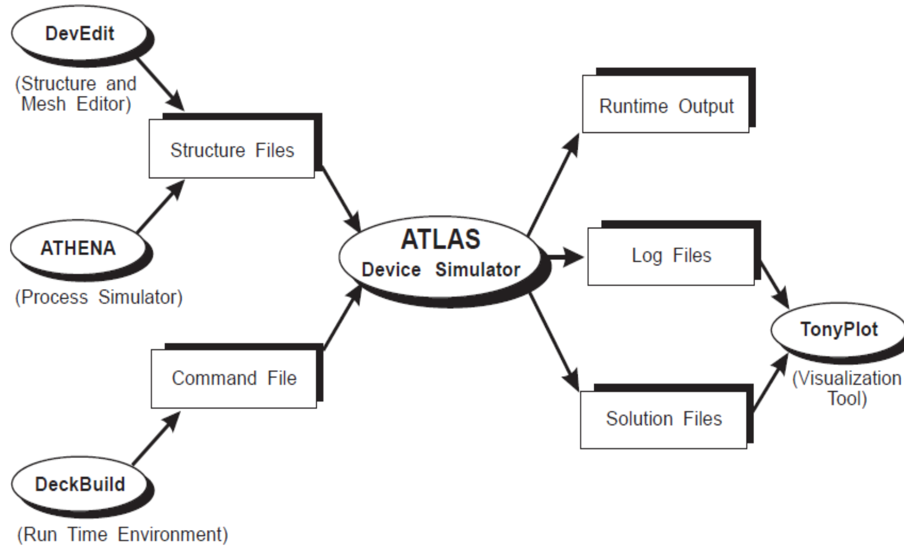

Figure 4.7: Atlas inputs and outputs.

4.3.3. Modes of operation:

Atlas is normally used in conjunction with the DeckBuild run-time environment, which supports both interactive and batch mode operation. It is always recommended to run Atlas within DeckBuild. This section presents the basic information to run Atlas in DeckBuild [73].

4.3.3.1. Running Atlas inside Deckbuild:

Each Atlas run inside DeckBuild should start with the line: `go atlas`

A single input file may contain several Atlas runs each separated with a go atlas line. Input files within DeckBuild may also contain runs from other programs such as Athena or DevEdit along with the Atlas runs [73].

4.3.3.2. The order of Atlas commands:

The order in which statements occur in an Atlas input file is important. There are five groups of statements that must occur in the correct order (see table 4.1). Otherwise, an error message will appear which may cause incorrect operation or termination of the program. For example, if the material parameters or models are set in the wrong order, then they may not be used in the

calculations. The order of statements within the mesh definition, structural definition, and solution groups is also important. Otherwise, it may also cause incorrect operation or termination of the program [73].

Table 4.1: The order of Atlas commands

Groups	Statements
1. Structure specification	MESH
	REGION
	ELECTRODE
	DOPING
2. Material and models specification	CONTACT
	MATERIAL
	INTERFACE
	MODELS
4. Numerical method selection	METHOD
5. Solution specification	SOLVE
	LOG
	SAVE
5. Results analysis	EXTRAC
	TONYPLOT

4.3.4. Atlas commands:

4.3.4.1. Structure specification:

There are three ways to define a device structure in Atlas. The first way is to read an existing structure from a file. The second way is to use the **Automatic Interface** feature from DeckBuild to transfer the input structure from Athena or DevEdit. The third way is create a structure by using the Atlas command language [73].

In order to define a device through the Atlas command language, you must first define a mesh. This mesh or grid covers the physical simulation domain. The mesh is defined by a series of horizontal and vertical lines and the spacing between them. Then, regions within this mesh are

allocated to different materials as required to construct the device. After the regions are defined, the location of electrodes is specified. The final step is to specify the doping in each region [73].

4.3.4.1.1. Mesh:

The first statement must be:

`MESH SPACE.MULT=<VALUE>`

This is followed by a series of `X.MESH` and `Y.MESH` statements.

```
X.MESH LOCATION=<VALUE> SPACING=<VALUE>
Y.MESH LOCATION=<VALUE> SPACING=<VALUE>
```

The `SPACE.MULT` parameter value is used as a scaling factor for the mesh created by the `X.MESH` and `Y.MESH` statements. The default value is 1. Values greater than 1 will create a globally coarser mesh for fast simulation. Values less than 1 will create a globally finer mesh for increased accuracy. The `X.MESH` and `Y.MESH` statements are used to specify the locations in microns of vertical and horizontal lines, respectively, together with the vertical or horizontal spacing associated with that line. You must specify at least two mesh lines for each direction. Atlas automatically inserts any new lines required to allow for gradual transitions in the spacing values between any adjacent lines. The `X.MESH` and `Y.MESH` statements must be listed in the order of increasing x and y. Both negative and positive values of x and y are allowed. Figure 4.8 illustrates how these statements work. On the left hand plot, note how the spacing of the vertical lines varies from 1 μm at x=0 and x=10 μm to 0.5 μm at x=5 μm. On the right hand plot, note how specifying the `SPACE.MULT` parameter to have a value of 0.5 has doubled the density of the mesh in both the X and Y directions [73].

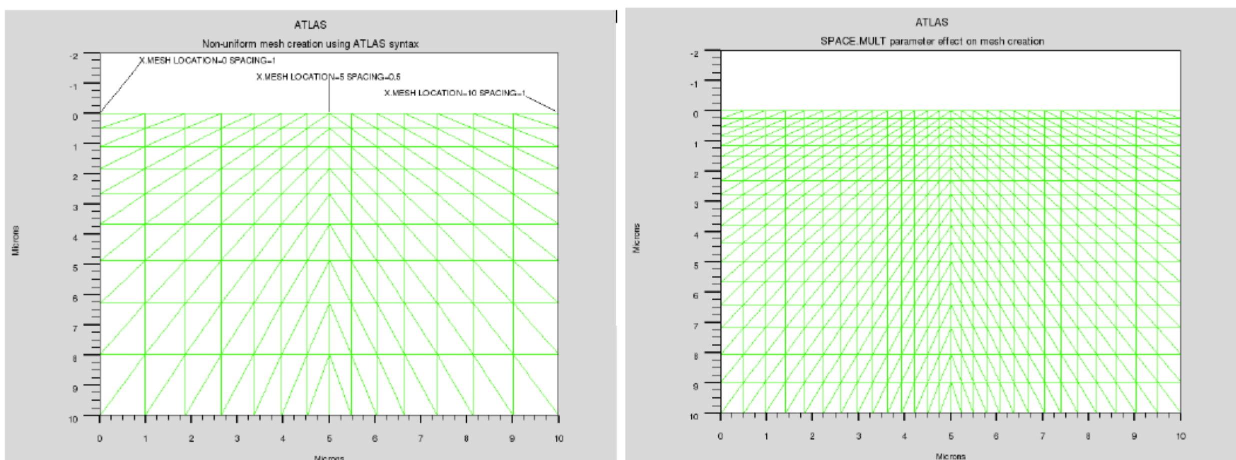

Figure 4.8: Non-uniform mesh creation using Atlas syntax.

4.3.4.1.2. Regions:

Once the mesh is specified, every part of it must be assigned a material type. This is done with `REGION` statements. For example:

```
REGION number=<integer> <material type> <position parameters>
```

Region numbers must start at 1 and are increased for each subsequent region statement. You can have up to 15000 different regions in Atlas. A large number of materials are available. If a composition-dependent material type is defined, the x and y composition fractions can also be specified in the `REGION` statement. The position parameters are specified in microns using the `X.MIN`, `X.MAX`, `Y.MIN`, and `Y.MAX` parameters. If the position parameters of a new statement overlap those of a previous `REGION` statement, the overlapped area is assigned as the material type of the new region. You can use the `MATERIAL` statement to specify the material properties of the defined regions. But you must complete the entire mesh and doping definition before any `MATERIAL` statements can be used [73].

4.3.4.1.3. Electrodes:

Once you have specified the regions and materials, define at least one electrode that contacts a semiconductor material. This is done with the `ELECTRODE` statement. For example:

```
ELECTRODE NAME=<electrode name> <position parameters>
```

You can specify up to 50 electrodes. The position parameters are specified in microns using the `X.MIN`, `X.MAX`, `Y.MIN`, and `Y.MAX` parameters. Multiple electrode statements may have the same electrode name. Nodes that are associated with the same electrode name are treated as being electrically connected. Some shortcuts can be used when defining the location of an electrode. If no Y coordinate parameters are specified, the electrode is assumed to be located on the top of the structure. You also can use the `RIGHT`, `LEFT`, `TOP`, and `BOTTOM` parameters to define the location [73].

4.3.4.1.4. Doping:

You can specify analytical doping distributions or have Atlas read in profiles that come from either process simulation or experiment. To specify the doping use the `DOPING` statement [73].
For example:

```
DOPING <distribution type> <dopant type> <position parameters>
```

Analytical doping profiles can have uniform, Gaussian, or complementary error function forms. The parameters defining the analytical distribution are specified in the DOPING statement [73]. Two examples are shown below with their combined effect shown in Figure 4.9.

```
DOPING UNIFORM CONCENTRATION=1E16 N.TYPE REGION=1
DOPING GAUSSIAN CONCENTRATION=1E18 CHARACTERISTIC=0.05 P.TYPE \
X.LEFT=0.0 X.RIGHT=1.0 PEAK=0.1
```

The first DOPING statement specifies a uniform n-type doping density of 10^{16} cm^{-3}. The position parameters X.MIN, X.MAX, Y.MIN, and Y.MAX can be used instead of a region number. The second DOPING statement specifies a p-type Gaussian profile with a peak concentration of 10^{18} cm^{-4}. This statement specifies that the peak doping is located along a line from x = 0 to x = 1 microns [73].

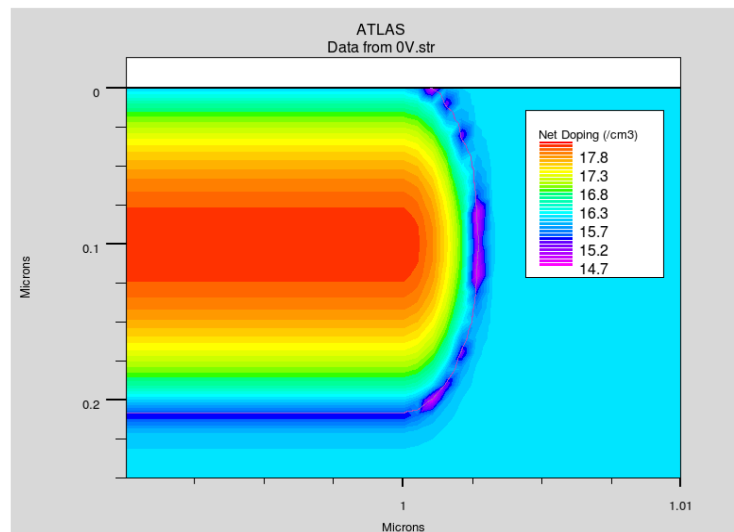

Figure 4.9: Analytical specification of a 2D Profile.

4.3.4.2. Material and models specification:

Once you define the mesh, geometry, and doping profiles, you can modify the characteristics of electrodes, change the default material parameters, and choose which physical models Atlas will use during the device simulation. To accomplish these actions, use the CONTACT, MATERIAL, and MODELS statements respectively. Impact ionization models can be enabled using the IMPACT statement. Interface properties are set by using the INTERFACE statement.

Many parameters are accessible through the Silvaco C-Interpreter (SCI). This allows you to define customized equations for some models.

4.3.4.2.1. Contact:

a. Workfunction for gates or Schottky contacts:

An electrode in contact with semiconductor material is assumed by default to be ohmic. If a work function is defined, the electrode is treated as a Schottky contact. The `CONTACT` statement is used to specify the metal workfunction of one or more electrodes. The `NAME` parameter is used to identify which electrode will have its properties modified. The `WORKFUNCTION` parameter sets the workfunction of the electrode [73]. For example,

`CONTACT NAME=gate WORKFUNCTION=5.8` sets the workfunction of the electrode named gate to 5.8eV. The workfunctions of several commonly used contact materials can be specified using the name of the material [73].

b. Setting current boundary conditions:

The `CONTACT` statement is also used to change an electrode from voltage control to current control. Current controlled electrodes are useful when simulating devices, where the current is highly sensitive to voltage or is a multi-valued function of voltage [73]. For example,

`CONTACT NAME=drain CURRENT` changes the drain electrode to current control.

4.3.4.2.2. Material:

a. Semiconductor, insulator or conductor

All materials are split into three classes: semiconductors, insulators and conductors. Each class requires a different set of parameters to be specified. For semiconductors, these properties include electron affinity, band gap, density of states and saturation velocities [73].

There are default parameters for material properties used in device simulation for many materials. The `MATERIAL` statement allows you to specify your own values for these basic parameters. Your values can apply to a specified material or a specified region [73]. For example, the statement:

`MATERIAL MATERIAL=Silicon EG300=1.12 MUN=1100` sets the band gap and low field electron mobility in all silicon regions in the device. If the material properties are defined by region, the region is specified using the `REGION` or `NAME` parameters in the `MATERIAL` statement [73]. For example, the statement:

`MATERIAL REGION=2 TAUN0=2e-7 TAUP0=1e-5` sets the electron and hole Shockley-Read-Hall recombination lifetimes for region number two. If the name, `base`, has been defined using the `NAME` parameter in the `REGION` statement, then the statement:

`MATERIAL NAME=base NC300=3e19` sets the conduction band density of states at 300 K for the region named base. The description of the `MATERIAL` statement provides a complete list of all the material parameters that are available [73].

b. Heterojunction materials

The material properties of heterojunctions can also be modified with the `MATERIAL` statement. In addition to the regular material parameters, you can define composition dependent material parameters. For example, composition dependent band parameters, dielectric constants, and saturation velocities.

For heterojunction material systems, the bandgap difference between the materials is divided between conduction and valence bands. The `ALIGN` parameter specifies the fraction of this difference applied to the conduction band edge. This determines the electron and hole barrier height and overrides any electron affinity specification [73].

4.3.4.2.3. Interface:

The `INTERFACE` statement is used to define the interface charge density and surface recombination velocity at interfaces between semiconductors and insulators [73]. For example, the statement:

`INTERFACE QF=3e10` specifies that all interfaces between semiconductors and insulators have a fixed charge of 4×10^{10} cm^{-2}. In many cases, the interface of interest is restricted to a specific region. This can be accomplished with the `X.MIN`, `X.MAX`, `Y.MIN`, and `Y.MAX` parameters on the `INTERFACE` statement. These parameters define a rectangle, where the interface properties apply [73]. For example, the statement:

`INTERFACE QF=3e10 X.MIN=1.0 X.MAX=2 Y.MIN=0.0 Y.MAX=0.5` restricts the interface charge to the semiconductor-insulator boundary within the specified rectangle. In addition to fixed charge, surface recombination velocity and thermionic emission are enabled and defined with the `INTERFACE` statement [73].

4.3.4.2.4. Models:

Physical models are specified using the `MODELS` and `IMPACT` statements. Parameters for these models appear on many statements including: `MODELS`, `IMPACT`, `MOBILITY`, and `MATERIAL`. The physical models can be grouped into five classes: mobility, recombination, carrier statistics, impact ionization, and tunneling. All models with the exception of impact ionization are

specified on the `MODELS` statement. Impact ionization is specified on the `IMPACT` statement [73].

4.3.4.3. Numerical methods selection:

4.3.4.3.1. Method:

Several different numerical methods can be used for calculating the solutions to semiconductor device problems. Numerical methods are given in the `METHOD` statements of the input file. Some guidelines for these methods will be given here. Different combinations of models will require Atlas to solve up to six equations. For each of the model types, there are basically three types of solution techniques: (a) decoupled (`GUMMEL`), (b) fully coupled (`NEWTON`) and (c) `BLOCK`. The `GUMMEL` method will solve for each unknown in turn keeping the other variables constant, repeating the process until a stable solution is achieved. The `NEWTON` method solve the total system of unknowns together. The `BLOCK` methods will solve some equations fully coupled while others are de-coupled. Generally, the `GUMMEL` method is useful where the system of equations is weakly coupled but has only linear convergence. The `NEWTON` method is useful when the system of equations is strongly coupled and has quadratic convergence. The `NEWTON` method may, however, spend extra time solving for quantities, which are essentially constant or weakly coupled. `NEWTON` also requires a more accurate initial guess to the problem to obtain convergence. Thus, a `BLOCK` method can provide for faster simulations times in these cases over `NEWTON`. `GUMMEL` can often provide better initial guesses to problems. It can be useful to start a solution with a few `GUMMEL` iterations to generate a better guess. Then, switch to `NEWTON` to complete the solution [73]. Specification of the solution method is carried out as follows:

```
METHOD GUMMEL BLOCK NEWTON
```

4.3.4.4. Solutions specification:

Atlas can calculate DC, AC small signal, and transient solutions. Obtaining solutions is similar to setting up parametric test equipment for device tests. You usually define the voltages on each of the electrodes in the device. Atlas then calculates the current through each electrode. Atlas also calculates internal quantities, such as carrier concentrations and electric fields throughout the device. This is information that is difficult or impossible to measure [73].

In all simulations, the device starts with zero bias on all electrodes. Solutions are obtained by stepping the biases on electrodes from this initial equilibrium condition. As will be discussed, due to the initial guess strategy, voltage step sizes are limited. To save results, use the `LOG` or `SAVE` statements [73].

4.3.4.4.1. Solve:

For example, in DC solutions, the voltage on each electrode is specified using the `SOLVE` statement.

```
SOLVE VGATE=1.0
SOLVE VGATE=2.0
```

It solves a single bias point with 1.0 V and then 2.0 V on the gate electrode. One important rule in Atlas is that when the voltage on any electrode is not specified in a given `SOLVE` statement, the value from the last `SOLVE` statement is assumed [73].

4.3.4.4.2. Log and Save:

Log files store the terminal characteristics calculated by Atlas. These are current and voltages for each electrode in DC simulations. In transient simulations, the time is stored. In AC simulations, the small signal frequency and the conductances and capacitances are saved [73]. For example, the statement:

`LOG OUTF=<FILENAME>` is used to open a log file. Terminal characteristics from all `SOLVE` statements after the `LOG` statement are then saved to this file along with any results from the `PROBE` statement. To not save the terminal characteristics to this file, use another `LOG` statement with either a different log filename or the `OFF` parameter. Typically, a separate log file should be used for each bias sweep. For example, separate log files are used for each gate bias in a MOS Id/Vds simulation or each base current in a bipolar Ic/Vce simulation. These files are then overlaid in TonyPlot. Log files contain only the terminal characteristics. They are typically viewed in TonyPlot. Parameter extraction of data in log files can be done in DeckBuild. Log files cannot be loaded into Atlas to re-initialize the simulation [73].

The `SAVE` statement is used for saving the basic data. The statement Syntax is:

```
SAVE OUTFILE=<filename>
```

In all cases the region boundaries, electrodes, mesh, and doping are saved. If a SOLVE statement has preceded the SAVE statement all electrical data from the last solution is stored [73].

4.3.4.5. Result analysis:

4.3.4.5.1. Extract:

The `EXTRACT` command allows extracting device parameters. It operates on the previous solved curve or structure file. By default, `EXTRACT` uses the currently open log file. To override this default, supply the name of a file to be used by `EXTRACT` before the extraction routine [73]. For example:

```
EXTRACT INIT INF="<filename>"
```

4.3.4.5.2. TonyPlot:

All graphics in Atlas is performed by saving a file and loading the file into TonyPlot. The TONYPLOT command causes Atlas to automatically save a structure file and plot it in TonyPlot. The TonyPlot window will appear displaying the material boundaries. Plot: Display menu is used to see more graphics options [73].

Chapter 5: Results and discussion

Chapter 5: Results and discussion

5.1. Introduction:

Transparent conducting metal oxides such as CdO and ZnO have excellent transparency in the visible region. They are widely used as windows in solar cells. Pure CdO and ZnO have n-type degenerate semiconducting behavior. Many researchs expose that CdO and ZnO thin films can create heterojunction structures just by depositing them onto p-Si substrates [4], [5], [47], [49], [74]–[80].

CdO/p-Si and ZnO/p-Si heterojunction solar cells which were fabricated by sol-gel method show poor photovoltaic performance [4], [5]. In this work numerical simulation using Silvaco ATLAS software is used to model the aforementioned solar cells and to elucidate this poor performance.

The same structures have been simulated, by using the extracted experimental results of these thin films, which were considered as semiconductors with continuous distribution of states in their band gap similar to an amorphous semiconductor. The density of states model used here is composed of four bands: two tail bands and two Gaussian distribution deep level bands. Evidently, the first case gave results far from reality. In the second case and by adjusting the constituents of the band gap states, it was possible to reproduce a good agreement between simulated and measured J-V characteristics of these solar cells.

5.2. Experimental results:

The CdO and ZnO thin films which were fabricated by sol-gel were studied and investigated. The optical characterization to be used in modeling the photovoltaic behaviour of CdO/p-Si and ZnO/p-Si solar cells were calculated and extracted.

5.2.1. Characterization of CdO thin film:

As seen in Figure 5.1(a), the transparency lies in the range of 70–80% in the visible range and it reaches a 92% value in the visible range. The optical band gap of CdO film was determined by

optical absorption method. It is well known that CdO is a direct band-gap semiconductor, and therefore, it has been used the following relation [81],

$$\alpha = \frac{B}{h\nu}(h\nu - E_g)^n \quad (5.1)$$

where B is an energy-independent constant, Eg is the optical band gap and n is a constant which determines the type of optical transitions and for indirect allowed transition, n=2; and indirect forbidden transition, n=3, for direct allowed transition, n=1/2; for direct forbidden transition, n=3/2. The curve of $(\alpha h\nu)^2$ vs. $h\nu$ for the CdO film was plotted, as shown in Figure 5.1(b). The Eg optical band gap of nanocluster-CdO film was found to be 2.27 eV [4].

In order to validate the simulation, it will be better to use the same experimental results of the film (CdO) used to fabricate the modeled solar cell (CdO/p-Si).

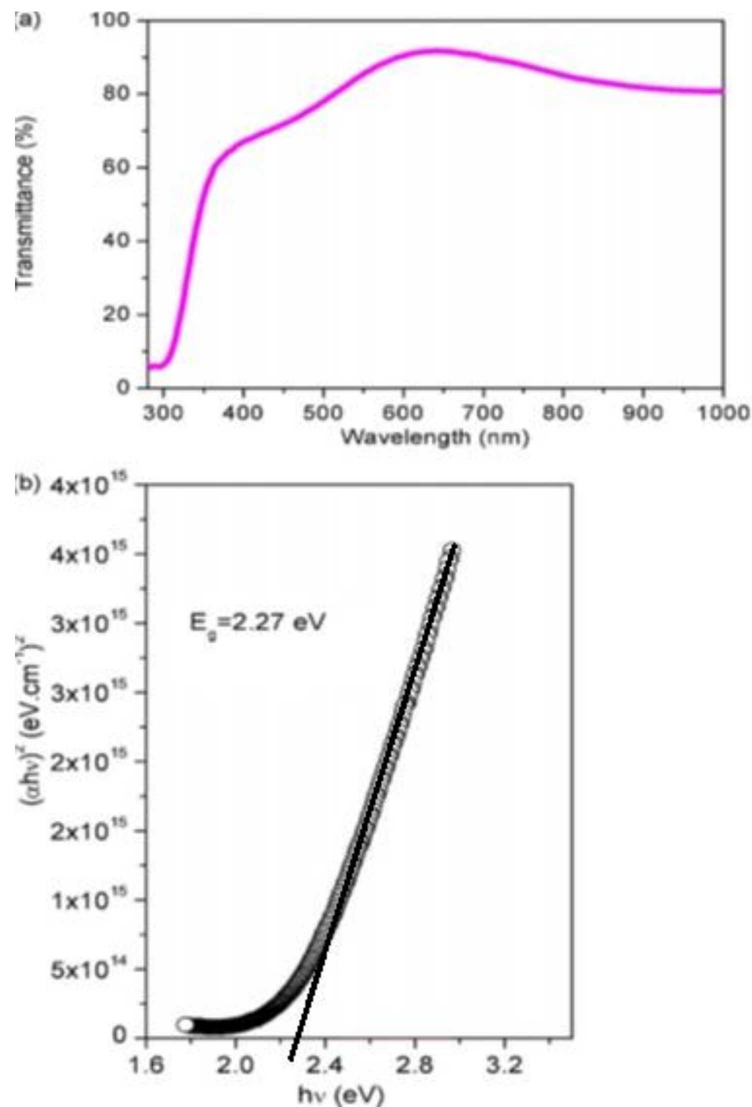

Figure 5. 1: Plots of transmittance and *(αhν)²* vs. *hν* for the nanostructure CdO film [4].

In order to extract the extinction coefficient values vs. wavelengths, we simply use the previous curve, $(\alpha h\nu)^2$ vs. $h\nu$. First we extract the absorption coefficient values vs. wavelengths, manually, and then we use the Eq. (5.2).

Since we have the extinction coefficient and the optical transmittance values vs. wavelengths we can use the Eq. (5.3) to extract the refractive index values vs. wavelengths.

$$k = \frac{\alpha\lambda}{4\pi} \qquad (5.2)$$

$$T(\lambda) = 1 - R(\lambda) = 1 - \frac{(n(\lambda) - 1)^2 + k(\lambda)^2}{(n(\lambda) + 1)^2 + k(\lambda)^2} \qquad (5.3)$$

where $T(\lambda)$ and $R(\lambda)$ are the transmittance and the reflectance of the cell's top surface (CdO film), respectively. $n(\lambda)$ and $k(\lambda)$ are, respectively, the refractive index and the extinction coefficient of the CdO film.

5.2.2. Characterization of CdO/p-Si solar cell:

The magnitude of generation of photoelectrons depends on a difference in electron affinities between the p-Si and CdO semiconductors. The solar cell characteristics are shown in Figure 5.2. The solar cell shows a photovoltaic behavior with a maximum open circuit voltage V_{oc} and short-circuit current I_{sc}. The photocurrent increases with increasing illumination intensity due to more generated photocarriers. The solar cell parameters can be obtained by the following equations .

$$FF = \frac{V_m I_m}{V_{oc} I_{sc}} \qquad (5.4)$$

and

$$\eta = \frac{J_{sc} V_{oc} FF}{P_{in} A} \qquad (5.5)$$

where FF is filling factor, V_{oc} is the open circuit voltage, J_{sc} is the short-circuit current density. I_m and V_m are current and potential maximum power point, P_{in} is the intensity of incident light, A is the cell area. The best values of V_{oc} and J_{sc} of Al/CdO/p-Si/Al solar cell were found to be V_{oc}= 0.41 V and J_{sc} = 2.19 mA/cm^2 under AM1.5, respectively. These results indicate that V_{oc} and J_{sc} values of Al/CdO/p-Si/Al are lower than some solar cells reported in the literature [82], however, this study opens the possibilities systematic research and further development in this

heterostructure. This is our preliminary attempt in the direction of making Al/CdO/p-Si/Al photovoltaic device, and our more studies are in progress to increase the J_{sc} and V_{oc} values.

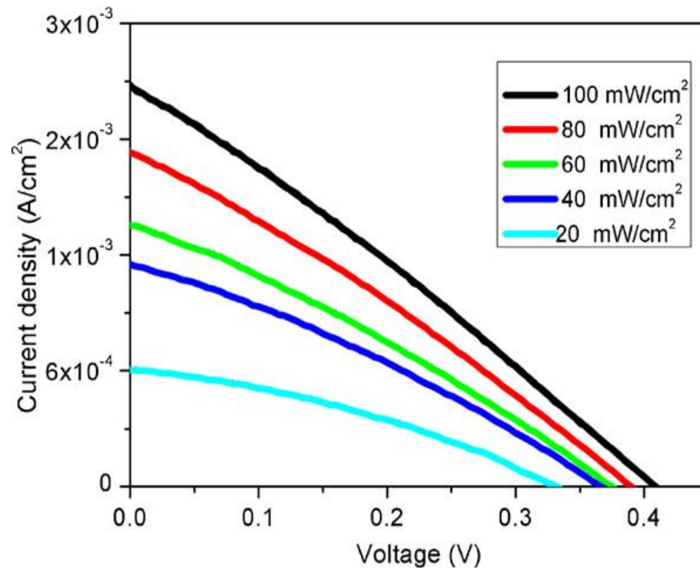

Figure 5. 2: Characteristics of the Al/CdO/p-Si/Al solar cell [4]**.**

Figure 5.3 shows the plots of V_{oc} and I_{sc} vs. P for the solar cell. The I_{sc} and V_{oc} values increase almost linearly with illumination intensity. The I_{sc} dependence of light intensity follows a power law $I_{sc} \sim F^{\alpha}$. The exponent α was found to be 0.75. This value shows the presence of continuous distribution of trapping centers [83]. The trap centers affect the generation process of photocarriers in Al/CdO/p-Si/Al solar cell [4].

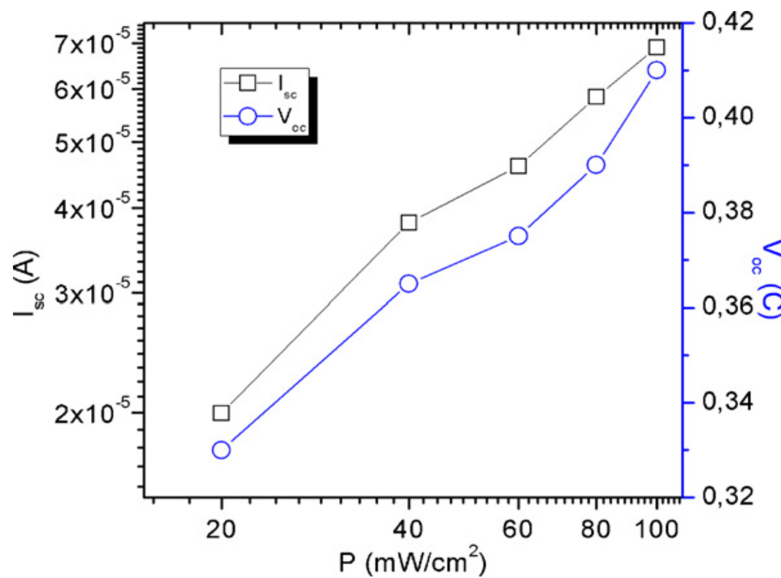

Figure 5.3: Plots of Isc and Voc vs. P of the Al/CdO/p-Si/Al solar cell [4]**.**

5.2.3. Characterization of ZnO thin film:

Figures 5.4, 5.5 and 5.6 show the transmittance (T), reflectance (R) and absorption coefficients (α) spectra as a function of wavelength range from 250 to 1000 nm for the ZnO thin film grown using the sol solutions with molarity: 0.3M.

The optical transmittance of a material is generally determined by the thickness, surface roughness, and absorption coefficient of the material.

The transmittance values of ZnO thin film, in the visible range, were found to be 85% - 92%. These high transmittance values in UV/VIS region make this film an excellent candidate for transparent window in solar cells.

The reflectance decreases as the wavelength increases (energy decreases) in the wavelength range (375-1000) nm

The absorption coefficient for the thin films was obtained using the equation,

$$I = I_0 e^{-\alpha d} \qquad (5.6)$$

where I and I_0 represent the intensities of the transmitted and incident light, respectively.

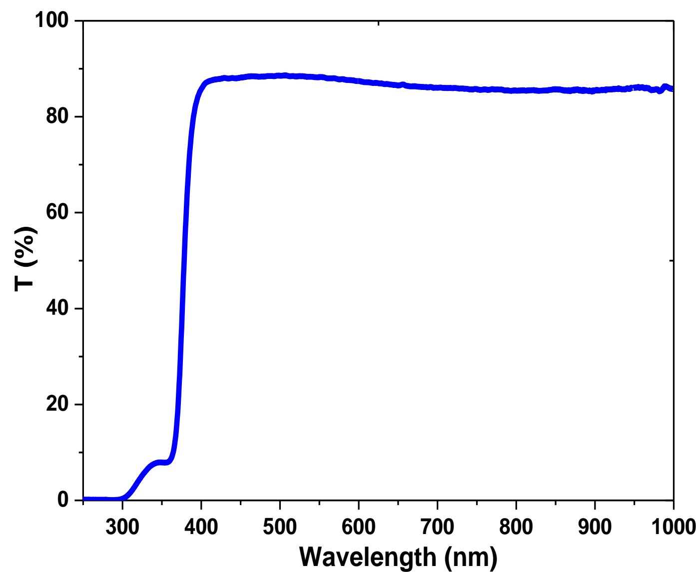

Figure 5. 4: Optical transmittance (T) as function of wavelength.

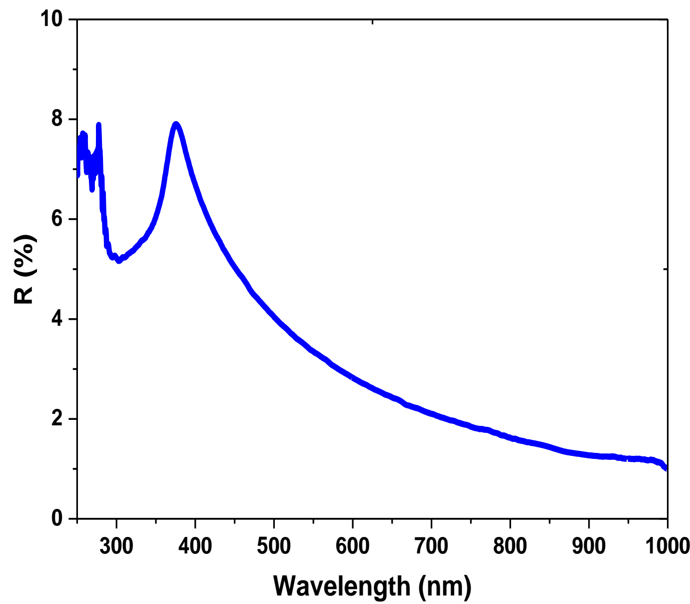

Figure 5. 5: Optical reflectance (R) as function of wavelength.

Considering interfaces related to the thin film and the thin film thickness in practical experiments, the transmittance and reflectance of the ZnO-based materials obey the following equation [84]:

$$T = (1 - R)^2 \exp[-\alpha d] \quad (5.7)$$

where T represents the optical transmittance, R denotes the reflectance, and d is the thickness of the thin films. Thus, α can be calculated using the following equation:

$$\alpha = -\frac{1}{d}\ln[T/(1-R)^2] \quad (5.8)$$

The optical bandgap (Eg) value of the thin film was calculated from a plot using the absorption coefficient of ZnO film as shown in Figure 5.7.

The presence of a single slope in the plot suggests that the films have direct and allowed transition. The band gap energy is obtained by extrapolating the straight line portion of the plot to zero absorption coefficient.

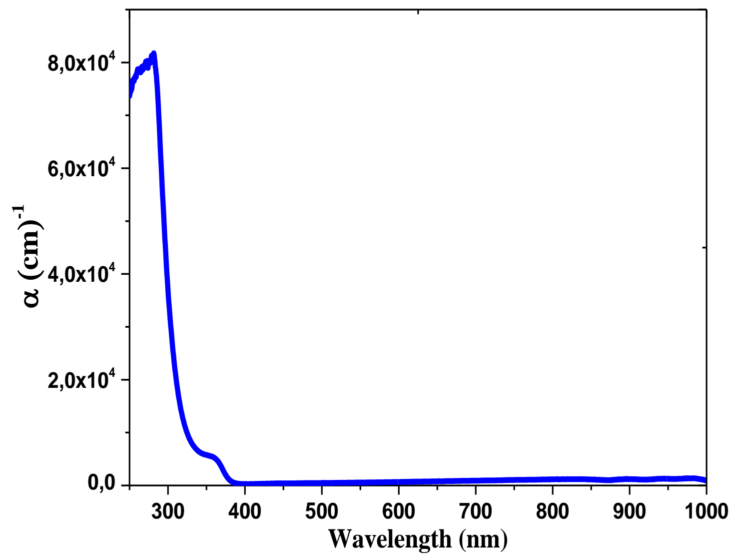

Figure 5. 6: Absorption coefficient (α) as function of wavelength.

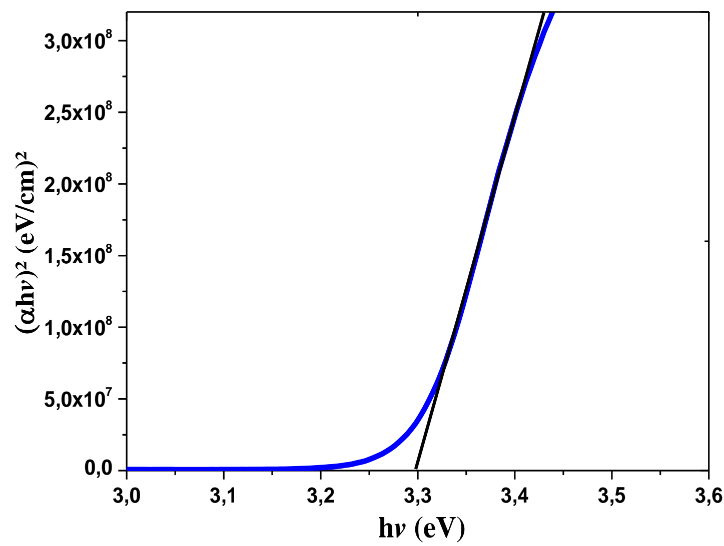

Figure 5. 7: $(\alpha h\nu)^2$ as function of wavelength.

The band gap value of ZnO thin film is found to be 3.3 eV. The absorption coefficient of ZnO thin films is found to be zero in forbidden energy region and it is found to increase rapidly with

the decrease in wavelength beyond energy band gap. Zero absorption coefficients of ZnO thin films in the visible range of spectrum make these thin films suitable as window layer in solar cells.

Figures 5.8 and 5.9 show the refractive index (n) and extinction coefficient (k), respectively, for the ZnO thin film grown using the sol-gel method. Knowledge of the dispersion of the refractive indices of semiconductor materials is essential to accurately model and optimize the optical properties of such materials. The complex refractive index of a semiconductor material can be expressed [85]:

$$\hat{n} = n(\omega) + ik(\omega) \qquad (5.9)$$

where n and k represent the real and imaginary parts, i.e., the refractive index and extinction coefficient of the complex refractive index, respectively. The real part quantifies the phase velocity of light whereas the imaginary part quantifies the absorption of light in the material. The refractive index of a semiconductor material can be calculated using the following relation [86]:

$$n = \left(\frac{1+R}{1-R}\right) + \sqrt{\frac{4R}{(1-R)^2} - k^2} \qquad (5.10)$$

where $k(=\alpha\lambda/4\pi)$, the extinction coefficient, can be calculated from the optical transmittance of the material.

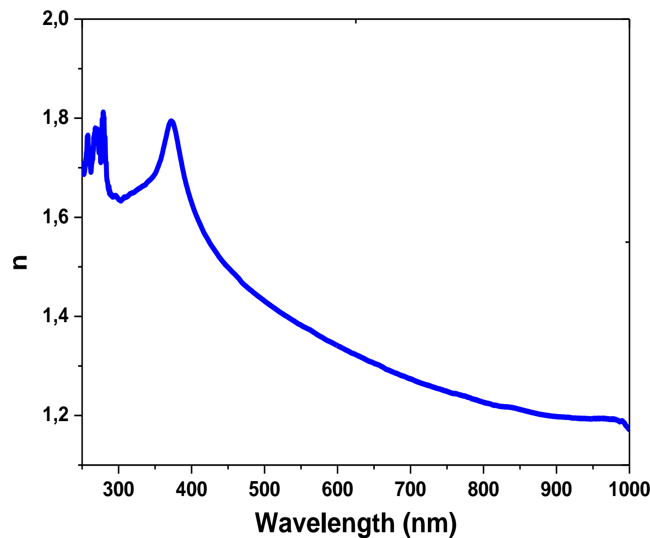

Figure 5. 8: Refractive index (n) as function of wavelength.

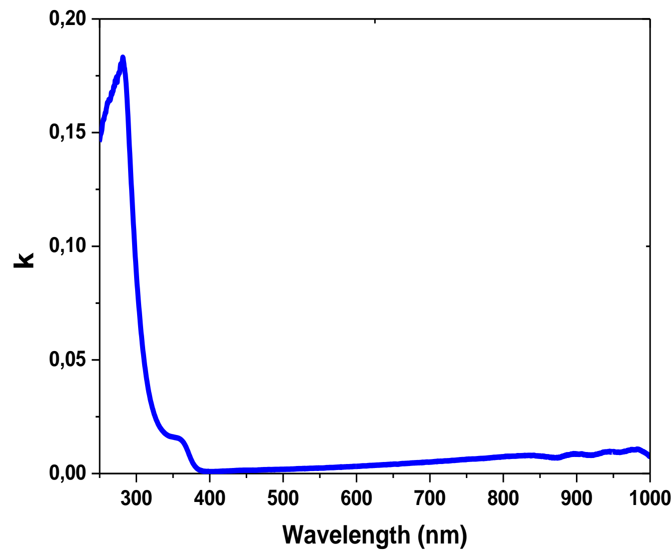

Figure 5. 9: Extinction coefficient (k) as function of wavelength.

Figures 5.10 and 5.11 show the dependence of the real (ε_1) and imaginary (ε_2) parts of the complex dielectric constant, respectively, on photon energy. The fundamental electron excitation spectra for the thin films are determined by the frequency dependence of the complex dielectric constant. The values of ε_1 and ε_2 are related to n and k and are calculated using the following formulas [85]:

$$\varepsilon_1 = n^2 - k^2 \qquad (5.11)$$

and

$$\varepsilon_2 = 2nk \qquad (5.12)$$

Thus, the dielectric properties of the ZnO thin film change with change in the refractive index and extinction coefficient of the thin films. The steep increase in ε_1 and ε_2 for photon energies is due to the band gap transitions.

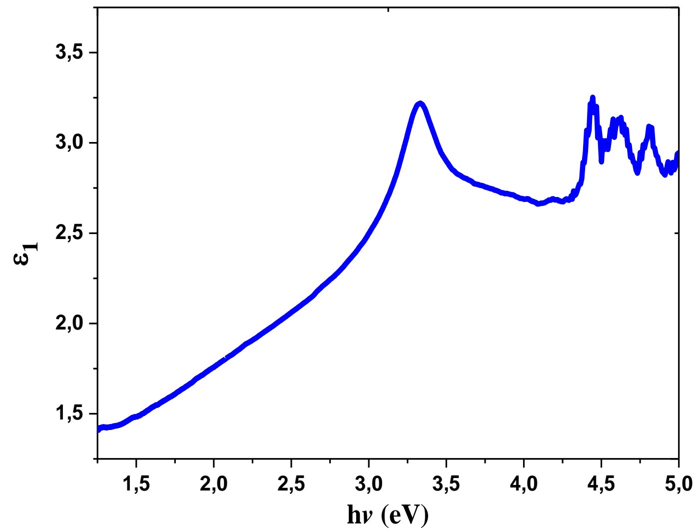

Figure 5. 10: Real dielectric constant (ε_1) as function of photon energy.

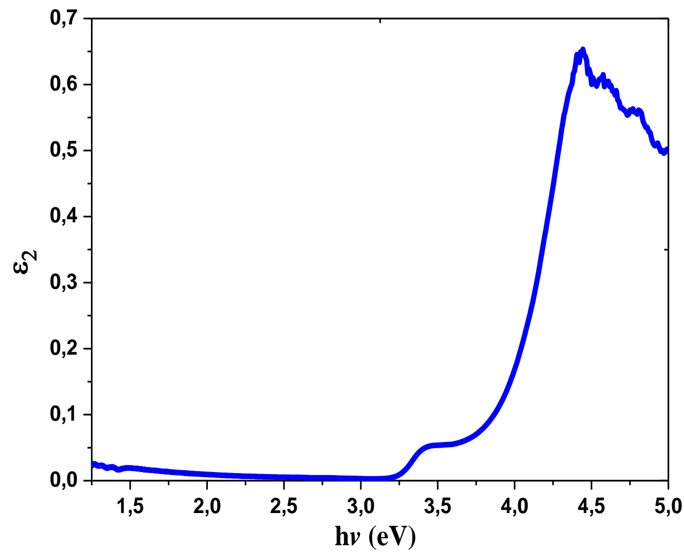

Figure 5. 11: Imaginary dielectric constant (ε_2) as function of photon energy.

5.2.4. Characterization of ZnO/p-Si solar cell:

The ZnO/p-Si solar cell which was fabricated by sol-gel spin coating method was electrically characterized. The short current density and open circuit voltage were measured and found to be

around J_{sc} = 8 mA/cm^2 and V_{oc} = 0.3 V, respectively, as shown in Figure 5.12. These results of this device are not of very high quality [5].

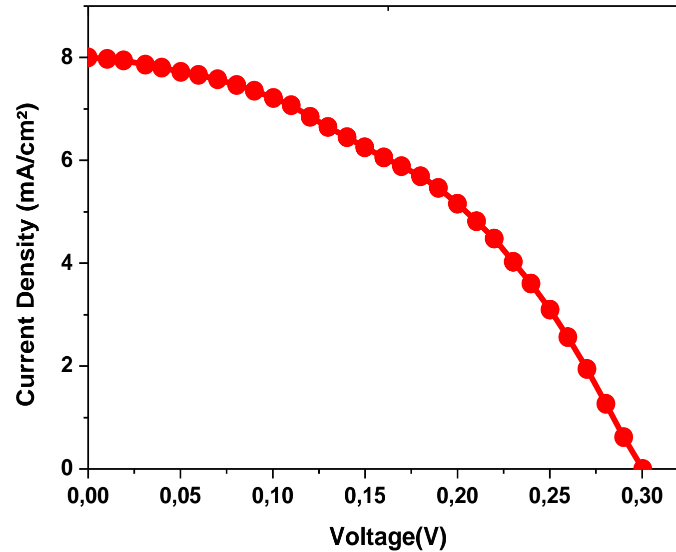

Figure 5. 12: Characteristics of the ZnO/p-Si solar cell [5]**.**

5.3. Simulation results:

The J-V results of both CdO/p-Si and ZnO/p-Si solar cells are lower than those similar solar cells reported in the literature [82]. It has been suggested that this poor performance was related to the presence of defects which create continuous distribution of trapping centers in the gap of CdO and ZnO materials. In the simulation section we will demonstrate this fact by considering the structures with and without the presence of the defects.

5.3.1. Important equations for simulation:

The space charge density in amorphous semiconductors is given by

$$\rho = q\left(p - n + n_{tail} - p_{tail} + n_{ga} - p_{gd} + N_d\right) \quad (5.13)$$

where n and p are the free carrier's densities, N_d is the n channel doping concentration and n_{tail}, p_{tail}, n_{ga}, p_{gd} are given by:

$$n_{tail} = \int_{E_v}^{E_c} g_{ct}^{A}(E) f_{ct}^{n}(E)\, dE \quad (5.14)$$

$$p_{tail} = \int_{E_v}^{E_c} g_{vt}^{D}(E) f_{vt}^{p}(E)\, dE \quad (5.15)$$

$$n_{ga} = \int_{E_v}^{E_c} g_{G}^{A}(E) f_{AG}^{n}(E)\, dE \quad (5.16)$$

$$p_{gd} = \int_{E_v}^{E_c} g_{G}^{D}(E) f_{DG}^{p}(E)\, dE \quad (5.17)$$

where $f_{ct}^{n}(E)$, $f_{AG}^{n}(E)$ are the ionization probabilities of the acceptor tail and Gaussian states, respectively, and $f_{vt}^{p}(E)$, $f_{DG}^{p}(E)$ are the ionization of the donor states (tail and Gaussian). At the steady state, these ionization probabilities are given by the Shockley-Read-Hall model as [87], [88]:

$$f_{ct}^{n}(E) = \frac{v_{th}^{n}\sigma_{nc}n + v_{th}^{p}\sigma_{pc}n_i e^{\frac{E_i-E}{k_BT}}}{v_{th}^{n}\sigma_{nc}\left(n + n_i e^{\frac{E-E_i}{k_BT}}\right) + v_{th}^{p}\sigma_{pc}\left(p + n_i e^{\frac{E_i-E}{k_BT}}\right)} \quad (5.18)$$

$$f_{AG}^{n}(E) = \frac{v_{th}^{n}\sigma_{ng}^{a}n + v_{th}^{p}\sigma_{pg}^{a}n_i e^{\frac{E_i-E}{k_BT}}}{v_{th}^{n}\sigma_{ng}^{a}\left(n + n_i e^{\frac{E-E_i}{k_BT}}\right) + v_{th}^{p}\sigma_{pg}^{a}\left(p + n_i e^{\frac{E_i-E}{k_BT}}\right)} \quad (5.19)$$

$$f_{vt}^{p}(E) = \frac{v_{th}^{p}\sigma_{pv}p + v_{th}^{n}\sigma_{nv}n_i e^{\frac{E-E_i}{k_BT}}}{v_{th}^{n}\sigma_{nc}\left(n + n_i e^{\frac{E-E_i}{k_BT}}\right) + v_{th}^{p}\sigma_{pc}\left(p + n_i e^{\frac{E_i-E}{k_BT}}\right)} \quad (5.20)$$

$$f_{DG}^{p}(E) = \frac{v_{th}^{p}\sigma_{pg}^{d}p + v_{th}^{n}\sigma_{ng}^{d}n_i e^{\frac{E-E_i}{k_BT}}}{v_{th}^{n}\sigma_{ng}^{d}\left(n + n_i e^{\frac{E-E_i}{k_BT}}\right) + v_{th}^{p}\sigma_{pg}^{d}\left(p + n_i e^{\frac{E_i-E}{k_BT}}\right)} \quad (5.21)$$

where v_{th}^{n} is the electron thermal velocity and v_{th}^{p} is the hole thermal velocity, n_i is the intrinsic carrier concentration. σ_{nc} and σ_{ng}^{a} are the electron capture cross-section for the acceptor tail and Gaussian states respectively. σ_{pc} and σ_{pg}^{a} are the hole capture cross-sections for the acceptor tail and Gaussian states respectively and σ_{nv}, σ_{ng}^{d}, σ_{pv}, and σ_{pg}^{d} are the equivalents for donors states.

It has to be mentioned here that when Eq. (5.13) is applied to a crystalline semiconductor (like Si) the terms $n_{tail} - p_{tail} + n_{ga} - p_{gd}$ are neglected.

The continuity equations for both electrons and holes, in steady state, are expressed as:

$$\frac{\partial n}{\partial t} = \frac{1}{q} div\overrightarrow{J_n} + G_n - R_n \qquad (5.22.a)$$

$$\frac{\partial p}{\partial t} = -\frac{1}{q} div\overrightarrow{J_p} + G_p - R_p \qquad (5.22.b)$$

where $\overrightarrow{J_n}$ and $\overrightarrow{J_p}$ are the electron and hole current densities, G_n and G_p are the generation rates for electrons and holes, R_n and R_p are the total recombination rates for electrons and holes in Gaussian and tail states, and q is the electron charge. The generation rate of these pairs at a position *x* from the illuminated front is given by [89]:

$$G(x) = \int_{Spectrum} T(\lambda)\phi_0(\lambda)\alpha(\lambda)exp(-\alpha(\lambda)x)\, d\lambda \quad (5.23)$$

where $\phi_0(\lambda)$ is the AM1.5 spectrum flux.

R_n and R_p are assumed to be the same and given by [90],

$$R_n = R_p = \int_{E_V}^{E_C} (np - n_i^2) \left\{ \left[\frac{v_{th}^n v_{th}^p \sigma_{pc}\, \sigma_{nc} g_{ct}^A(E)}{v_{th}^n \sigma_{nc}\left(n + n_i e^{\frac{E-E_i}{k_B T}}\right) + v_{th}^p \sigma_{pc}\left(p + n_i e^{\frac{E_i-E}{k_B T}}\right)} \right] + \left[\frac{v_{th}^n v_{th}^p \sigma_{pv}\, \sigma_{nv} g_{vt}^D(E)}{v_{th}^n \sigma_{nv}\left(n + n_i e^{\frac{E-E_i}{k_B T}}\right) + v_{th}^p \sigma_{pv}\left(p + n_i e^{\frac{E_i-E}{k_B T}}\right)} \right] + \left[\frac{v_{th}^n v_{th}^p \sigma_{pg}^a \sigma_{ng}^a g_G^A(E)}{v_{th}^n \sigma_{ng}^a\left(n + n_i e^{\frac{E-E_i}{k_B T}}\right) + v_{th}^p \sigma_{pg}^a\left(p + n_i e^{\frac{E_i-E}{k_B T}}\right)} \right] + \left[\frac{v_{th}^n v_{th}^p \sigma_{pg}^d \sigma_{ng}^d g_G^D(E)}{v_{th}^n \sigma_{ng}^d\left(n + n_i e^{\frac{E-E_i}{k_B T}}\right) + v_{th}^p \sigma_{pg}^d\left(p + n_i e^{\frac{E_i-E}{k_B T}}\right)} \right] \right\} dE \qquad (5.24)$$

where v_{th}^n is the electron thermal velocity and v_{th}^p is the hole thermal velocity, n_i is the intrinsic carrier concentration. σ_{nc} and σ_{ng}^a are the electron capture cross-section for the acceptor tail and Gaussian states respectively. σ_{pc} and σ_{pg}^a are the hole capture cross-sections for the acceptor tail and Gaussian states respectively and σ_{nv}, σ_{ng}^d, σ_{pv}, and σ_{pg}^d are the equivalents for donors states.

In the drift-diffusion model, the current densities are expressed in terms of the quasi-Fermi levels ϕ_n and ϕ_p as:

$$\vec{J}_n = -q\mu_n n \nabla\phi_n \quad (5.25.\mathrm{a})$$

$$\vec{J}_p = -q\mu_p p \nabla\phi_p \quad (5.25.\mathrm{b})$$

where μ_n and μ_p are the electron and hole mobilities, respectively. The quasi-Fermi levels are then linked to the carrier concentrations and the potential through the two Boltzmann approximations: $n = n_i exp\left(\frac{\psi-\phi_n}{k_B T}\right)$ and $p = n_i exp\left(-\frac{\psi-\phi_p}{k_B T}\right)$ where n_i is the effective intrinsic concentration and T is the lattice temperature.

The electrical characteristics are calculated following the specified physical structure and bias conditions. This is achieved by approximating the operation of the device onto a two dimensional grid, consisting of a number of grid points called nodes. By applying the set of differential equations (Poisson's and continuity equations) onto this grid (or equation's discretization), the transport of carriers through the structure can be simulated. The finite element grid is used to represent the simulation domain.

5.3.2. CdO modelling:

Of interest to the present work, the current-voltage characteristics are calculated under illumination and different conditions. In the first case, the CdO film will be considered as a crystalline semiconductor (absence of defects). In the second case, the CdO film will be considered as an amorphous semiconductor, i.e it contains a continuously distributed energy states in its band gap due to the presence of defects.

5.3.2.1. Crystalline CdO:

The parameters used in this work to simulate the Al/CdO/p-Si/Al solar cell are presented in tables 5.1 and 5.2 for CdO and Si respectively.

Table 5.1: Parameters used to simulate the CdO film of the ideal Al/CdO/p-Si/Al solar cell.

Parameter	Value	Reference
Band gap	2.27 eV	[4]
Electron affinity	4.51 eV	[47]
Donor density, N_D	$4.4\text{x}10^{19}$ cm^{-3}	[50]
CB effective density of states, N_C	$2.2\text{x}10^{19}$ cm^{-3}	[73]
VB effective density of states, N_V	$1.8\text{x}10^{19}$ cm^{-3}	[73]
Electron mobility	7.03 cm^2/Vs	[50]
SRH lifetime for electrons and holes	$1\text{x}10^{-9}$ s	[73]

Table 5.2: Parameters used to simulate silicon of the ideal Al/CdO/p-Si/Al solar cell.

Parameter	Value	Reference
Band gap	1.12 eV	[64]
Electron affinity	5.05 eV	[64]
Acceptor density, N_A	2.0×10^{17} cm^{-3}	Supposed
CB effective density of states, N_C	2.8×10^{19} cm^{-3}	[64]
VB effective density of states, N_V	1.04×10^{19} cm^{-3}	[64]
Electron mobility	1450 cm^2/Vs	[64]
SRH lifetime for electrons and holes	1×10^{-7} s	[73]

The simulated (compared to measured) *J-V* characteristic under AM1.5 spectrum for the ideal Al/CdO/p-Si/Al solar cell using the parameters of tables 5.1 and 5.2 is shown in Figure 5.13. The short circuit current density (J_{SC}) and the open circuit voltage (V_{OC}) are much higher than those of measured J-V characteristics. Therefore it is of no interest to discuss this case.

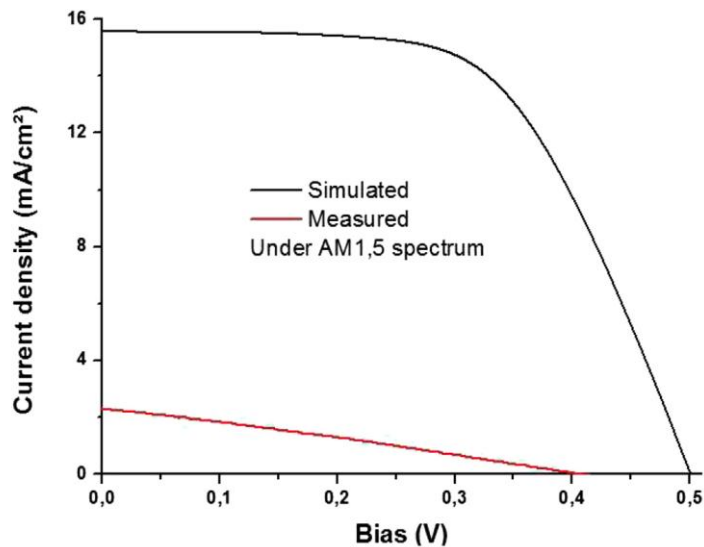

Figure 5.13: The simulated J-V characteristics of the ideal Al/n-CdO/p-Si/Al solar cell under AM1.5 spectrum.

5.3.2.2. Amorphous CdO:

It is well known that, in most cases, thin films have non crystalline structure. It is therefore expected that the polycrystalline or amorphous nature of these films give rise to defects in the

film lattice. These will give rise to different types of energy levels in the band gap of the material.

In amorphous semiconductors, the density of states (DOS) is composed of four bands: two tail bands (a donor-like valence band and an acceptor-like conduction band) and two deep level bands (one acceptor-like and the other donor-like). The firsts are modeled as decaying exponentials from the band edge while the latters are modeled using a Gaussian distribution. The density is then given by:

$$g(E) = g_{GA}(E) + g_{GD}(E) + g_{TA}(E) + g_{TD}(E) \quad (5.26)$$

The subscripts *G* and *T* are for Gaussian and tail respectively while *A* and *D* are for acceptor and donor respectively.

$$g(E) = G_{GA}exp\left[-\left[\frac{E_{GA}-E}{\sigma_D}\right]^2\right] + G_{GD}exp\left[-\left[\frac{E-E_{GD}}{\sigma_D}\right]^2\right] + G_{TA}\,exp\left[\frac{E-E_C}{E_A}\right] + G_{TD}exp\left[\frac{E_V-E}{E_D}\right] \quad (5.27)$$

Where $E_{V(C)}$is the valence (conduction) band edge, $G_{TD(A)}(\,cm^{-3}eV^{-1})$ the effective density at $E_{V(C)}$, $E_{D(A)}$ the characteristic slope energy of the valence (conduction) band-tail states, $G_{GA(D)}$ the total density ($cm^{-3}eV^{-1}$), $\sigma_D(\sigma_A)$ the standard deviation and $E_{GD(A)}$ the peak energy of the Gaussian distribution.

The parameters of the different constituents of the DOS used to simulate their effect on the Al/CdO/p-Si/Al solar cell performance are presented in table 5.3.

Table 5.3: Parameters of the DOS used to simulate the CdO film of the Al/CdO/p-Si/Al solar cell.

Parameter	Value
Standard deviation of the deep acceptors σ_A (eV)	0.025
Standard deviation of the deep donors σ_D (eV)	0.05
Peak energy of deep acceptors E_{GA} (eV)	1.225
Peak energy of deep donors E_{GD} (eV)	1.225
Characteristic slope energy of the valence band-tail states E_A (eV)	0.1
Characteristic slope energy of the conduction band-tail states E_D (eV)	0.1

Furthermore the capture cross-sections for majority and minority carriers are 1×10^{-14} and $1 \times 10^{-16}\ cm^2$ respectively for all states. A schematic representation of such states is shown in figure 5.14 for densities of: $G_{GA} = G_{GD} = 1 \times 10^{14}\ cm^{-3}eV^{-1}$ and $G_{TA} = G_{TD} = 1 \times 10^{19}\ cm^{-3}eV^{-1}$.

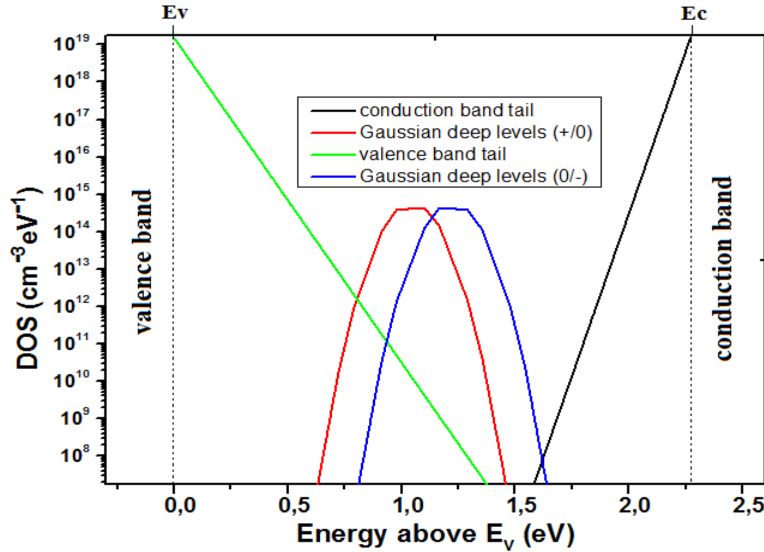

Figure 5.14: The density of states (Gaussian and tail) in the nergy gap of CdO.

We will now consider the effect of the different constituents of the DOS on the *J-V* characteristics of the non-ideal Al/CdO/p-Si/Al solar cell under AM1.5 spectrum.

5.3.2.3. Effect of the deep Gaussian states:

First the acceptor-like and donor-like deep level bands in the CdO film are varied symmetrically ($g_{GA}(E) = g_{GD}(E)$) and the *J-V* characteristics of the non-ideal Al/n-CdO/p-Si/Al solar cell under AM1.5 spectrum were computed. The density of tail was kept at a low value at $G_{TA} = G_{TD} = 1 \times 10^{10}\ cm^{-3}eV^{-1}$so that it can be neglected compared to deep states. The acceptor doping concentration of silicon was $N_A = 1 \times 10^{18}\ cm^{-3}$. The fixed oxide charge density was also kept low at $Q_f = 3 \times 10^{10}\ cm^{-2}$. The simulated *J-V* characteristics are shown in Figure 5.15.

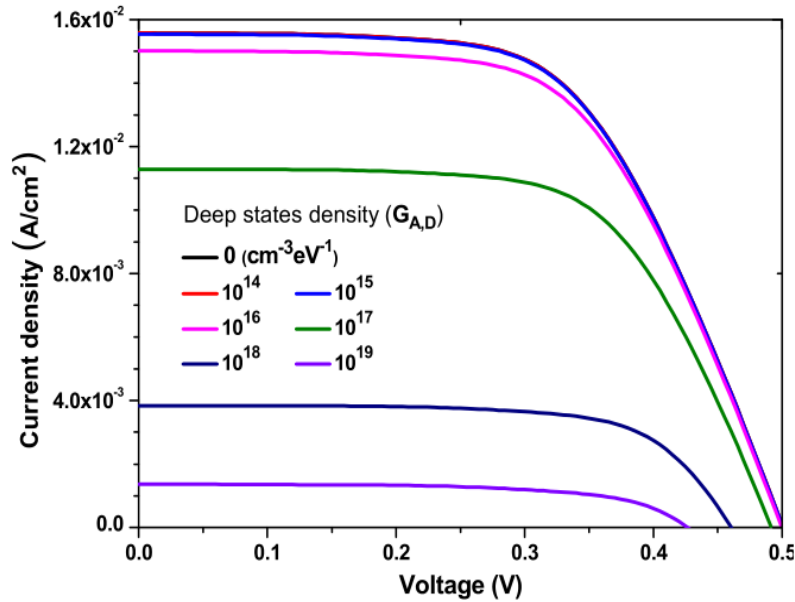

Figure 5.15: The simulated J-V characteristics of the non-ideal Al/CdO/p-Si/Al solar cell under AM1.5 spectrum for variable acceptor-like and donor-like deep Gaussian bands in the CdO film.

The figures of merit of the solar cell: the short circuit current density (J_{SC}), the open circuit voltage (V_{OC}), the efficiency (η) and the fill factor (*FF*) are extracted from the *J-V* characteristics. These are shown in Figure 5.16.

The cell performance parameters do not change as long as the DOS stays below 1×10^{14} cm^{-3} eV^{-1}. From 10^{16} cm^{-3} eV^{-1}, the presence of deep level bands in the CdO film degrades all solar cell parameters except the fill factor which increases with increasing density. It has to be mentioned that although the decreased parameters tend to approach the real (measured parameters), the fill factor is not. This means that the simulated *J-V* characteristics are not comparable to measurements. The degradation of J_{SC} can be understood from the fact that the photogenerated carriers are captured by the high density of the defects. The degradation of V_{OC} can be explained by a decrease in J_{SC} as well as a possible increase of the dark saturation current J_S of the CdO/Si diode in the presence of defects in accordance to the relation $V_{OC} \approx V_T ln(J_{SC}/J_S)$.

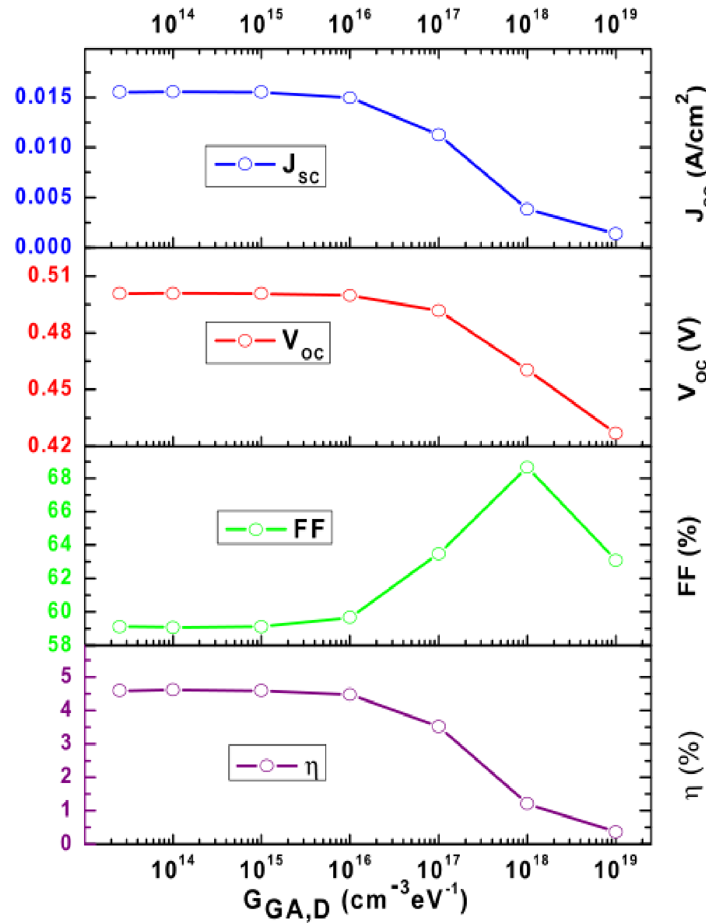

Figure 5.16: The effect of deep level Gaussian bands in the CdO film on the solar cell performance parameters under AM1.5 spectrum.

The strange behaviuor of the fill factor *FF* (increasing then decreasing) with increasing density of states) may be explained by considering the equivalent circuit of the solar cell. The electric model is often composed of: a diode, representing the behavior of the solar cell in dark, a current source representing the photogenerated current, a series resistance R_s representing the resistive losses of the material and a shunt resistance R_{sh} modeling parasitic currents which cross the cell. When the defect DOS increases, two cases arise:

(i) If defects are found in the space-charge zone, the increase of the defects DOS can create conduction channels and leakage currents associated. This will decrease R_{sh}.

(ii) If defects are found out of the space charge zone, the increase of the defect DOS will increase the non-radiative recombination rate, thus increasing R_s.

In the present case, ie when the defects increases, the space charge decreases inducing a decrease in R_{sh} but an increase in R_s. Both resistances are known to influence the fill factor of the solar cell. An increase in R_s (or decrease in R_{sh}) will degrade FF. So there is a competution between the effects of both resistances. An increase in FF is dominated by the decrease in R_s while a decrease in FF is dominated by the decrease in R_{sh}.

5.3.2.4. Effect of the tail states:

The second case was studying the effect of the tail states on the solar cell performance by varying, symmetrically, the acceptor and donor densities at the conduction and valence band edges of the CdO film respectively ($G_{TA} = G_{TD}$). The density deep states was kept at a low value of $G_{GA} = G_{GD} = 1 \times 10^{10}\ cm^{-3}eV^{-1}$ so that it can be neglected compared to tail states. The acceptor doping concentration of silicon was $N_A = 1 \times 10^{18}\ cm^{-3}$. The fixed oxide charge density was also kept low at $Q_f = 3 \times 10^{10}\ cm^{-2}$. The simulated *J-V* characteristics are shown in Figure 5.17.

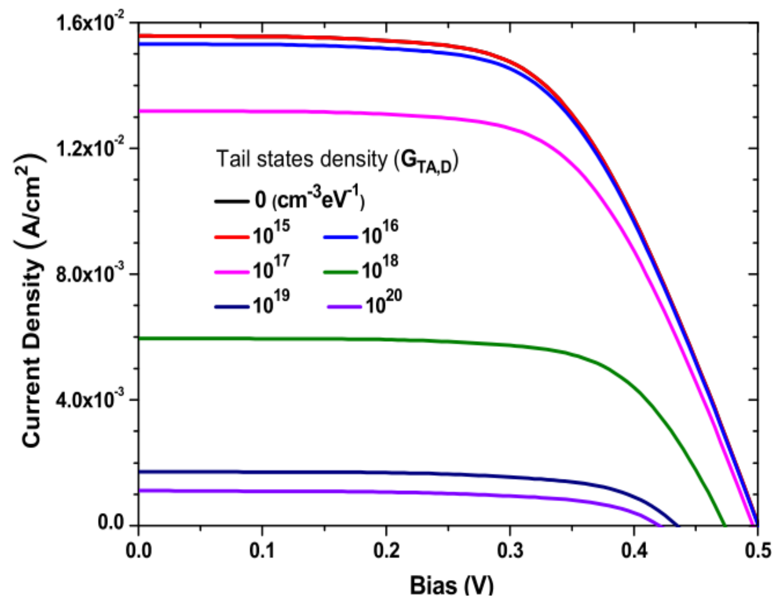

Figure 5.17: The simulated J-V characteristics of the non-ideal Al/CdO/p-Si/Al solar cell under AM1.5 spectrum for variable acceptor-like and donor-like deep tail states in the CdO film.

The figures of merit of the solar cell: the short circuit current density (J_{SC}), the open circuit voltage (V_{OC}), the efficiency (η) and the fill factor (*FF*) are extracted from the *J-V* characteristics. These are shown in Figure 5.18.

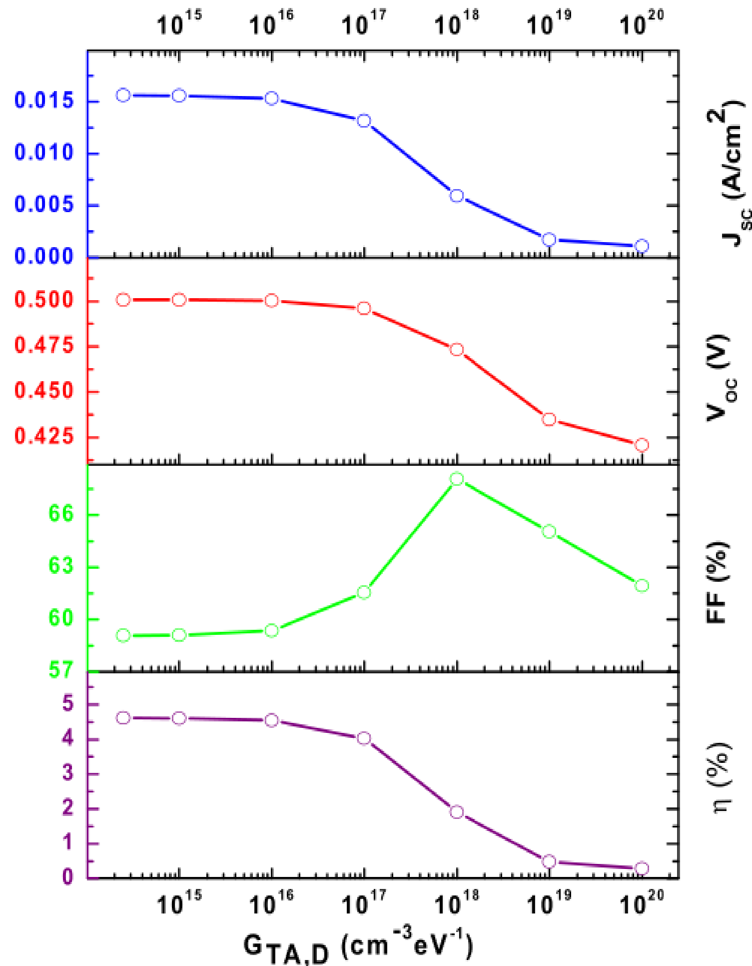

Figure 5.18: The effect of the density of the tail states at the conduction and valence band edges in the CdO film on the solar cell performance parameters under AM1.5 spectrum.

The cell performance parameters do not change as long as the tail states density stays below 1×10^{16} cm^{-3} eV^{-1}. From 10^{16} cm^{-3} eV^{-1}, the presence of deep level bands in the CdO film degrades all solar cell parameters except the fill factor which increases with increasing density until 1×10^{18} cm^{-3} eV^{-1} when it starts to decrease. As in the case of the DOS effect and although the decreased parameters tend to approach the real (measured parameters), the fill factor is not. This means that the simulated *J-V* characteristics are still not comparable to measurements.

It has to be mentioned that the effect of tail states is very similar to that of Gaussian states. In both cases the effect indicates that the defects act as dopants, modifying the doping profile and reducing the space charge zone of the junction. So the same analysis of the dependence of the solar cell parameters on the density of the tail states used in the previous case may are applicable here.

5.3.2.5. Effect of p-type doping of silicon:

The third and last case studied is the effect of the p-type doping of the silicon absorber layer (Si) which was varied from $N_A = 2.5 \times 10^{17}$ to $1 \times 10^{18}\ cm^{-3}$. The other parameters were: the density of the Gaussian deep states distribution $G_{A,D} = 1 \times 10^{15} cm^{-3} eV^{-1}$, the density of the tail $G_{TA,D} = 1 \times 10^{19} cm^{-3} eV^{-1}$ and the fixed oxide charge density $Q_f = 1 \times 10^{10} cm^{-2}$. The simulated *J-V* characteristics are shown in Figure 5.19.

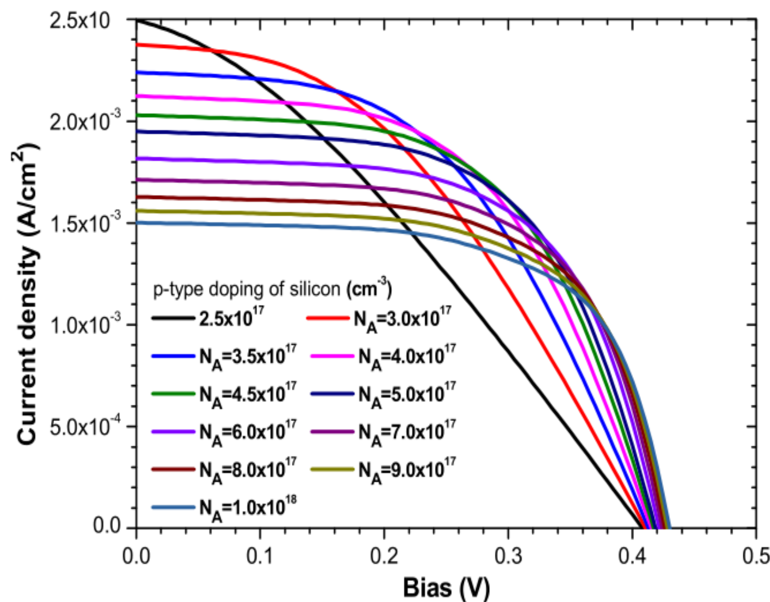

Figure 5.19: The simulated J-V characteristics of the non-ideal Al/CdO/p-Si/Al solar cell under AM1.5 spectrum for variable p-type doping of

The extracted figures of merit of the solar cell are shown in Figure 5.20 under the effect of variable p-type doping of silicon. V_{OC} increases with increasing p-type doping of Si. This can be understood bearing in mind that it is proportional to the barrier (diffusion, built-in) voltage (V_B)

of the p-n junction and the latter is proportional to the doping density of the two sides of the junction as $V_B = kT/q ln(N_A N_D/n_i^2)$. J_{SC}, on the other hand, decreases which may be due to the decrease in of the junction dark saturation current density J_S which in turn is inversely proportional to the doping density. This relationship is given by $J_{SC} = J_S ln(V_{OC}/V_T) \propto (1/N_A) ln(V_{OC}/V_T)$. Although V_{OC}increases, but the increase of N_A (the decrease of $1/N_A$) will be far more influent. The increase in the fill factor (FF) with increasing N_A may be interpreted by the effect on the space charge region (SCR) of which the width increase with decreasing doping density. This may create a path through the defects in SCR which is usually represented as a shunt resistance R_{sh} in the electrical model of a diode. The effect of R_{sh} on FF is well known: they are simply proportional. Thus a decrease in R_{sh} induces a decrease in FF.

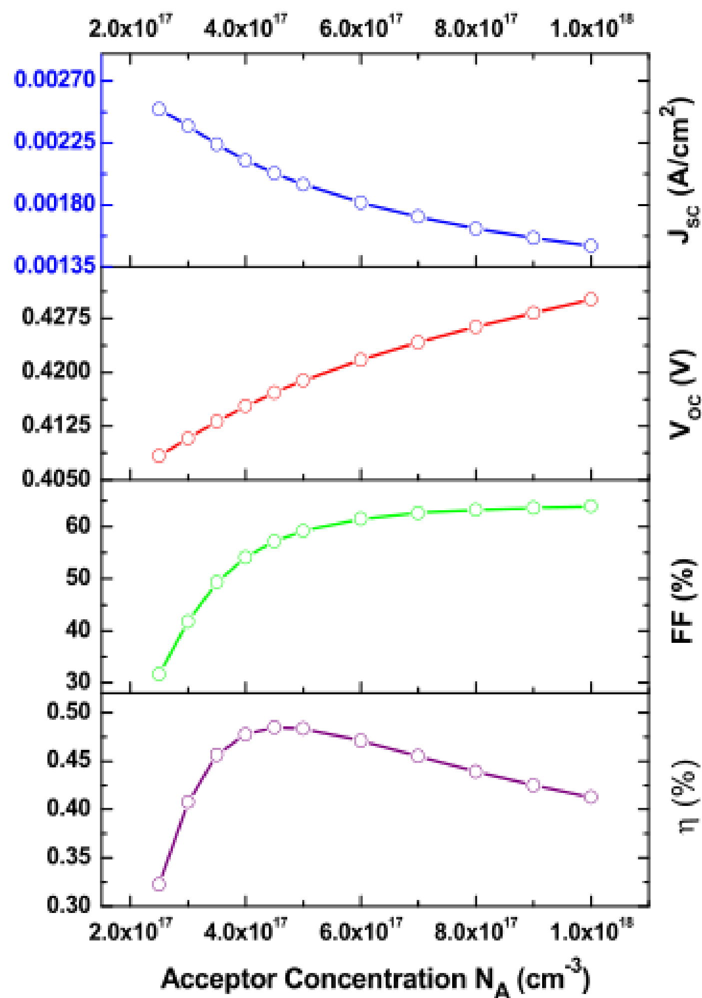

Figure 5.20: The extracted figures of merit extracted from the simulated J-V characteristics of the non-ideal Al/CdO/p-Si/Al solar cell under AM1.5 spectrum for variable p-type doping of Silicon.

5.3.2.6. Simulation of the effect of defects under different illumination power intensities on the Al/CdO/p-Si/Al solar cell performance:

Simulation of the effect of the tail and Gaussian defect on the Al/CdO/p-Si/Al solar cell has led to comparable values between simulation and measurement for both $V_{OC}$and J_{SC}. However the effect was not able to obtain comparable values for *FF*. The acceptor doping of silicon induced comparable values for *FF*. Combing the effects of defects in CdO and doping in Si, all parameters were almost perfectly reproduced when the solar cell is subjected to AM1.5 spectrum (light power intensity of 100 mW/cm^2). The values which gave comparable simulation and measurement were: an acceptor p-type doping of silicon, N_A= 2.07x10^{17} cm^{-3}, a total density of the Gaussian states, $G_{Ga,d}$=1x10^{15} cm^{-3}/eV, a density of tail states, $G_{Ta,d}$= 1.5x10^{19} cm^{-3}/eV, and a fixed oxide charge density; Qf=5x10^{11} cm^{-2}. These values were then used to simulate the effect of light intensity on the *J-V* characteristics of the solar cell and compared to measurements. This comparison is shown in Figure 5.21.

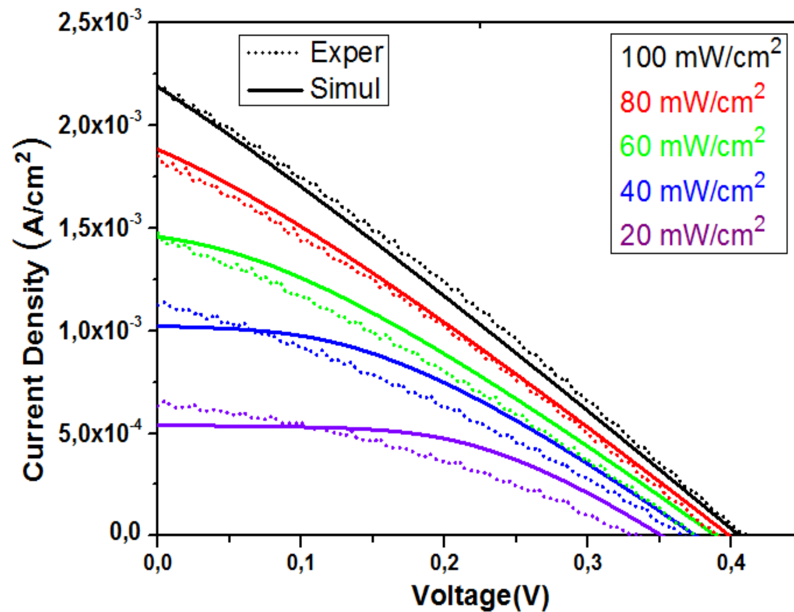

Figure 5.21: Comparison of simulated and measured J-V characteristics of the Al/CdO/p-Si/Al solar cell diode for different illumination power intensities.

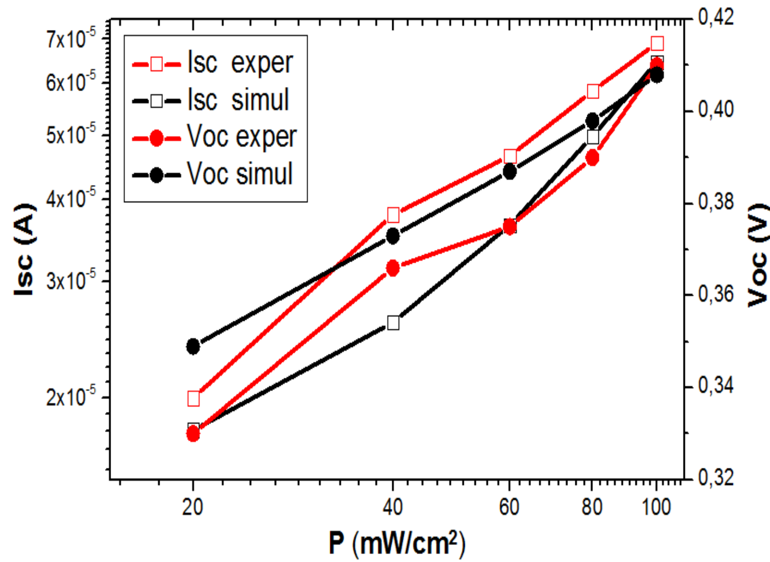

Figure 5.22: Comparison of the Al/CdO/p-Si/Al solar cell parameters extracted from the simulated and measured J-V characteristics of Figure 5.21 for different illumination power intensities.

As it is very clear there is a very good agreement between simulation and measurements. From Figure 5.21, the solar cell parameters are extracted and presented in Figure 5.22. The extracted parameters give almost a perfect match between simulation and measurement.

5.3.3. ZnO modelling:

A similar study of CdO is carried out fo ZnO. In the first case, the ZnO film will be considered as a crystalline semiconductor (absence of defects). In the second case, the ZnO film was considered as an amorphous semiconductor, i.e. it contains a continuously distributed energy states in its band gap due to the presence of defects.

5.3.3.1. Crystalline ZnO:

The parameters of ZnO used in this work to simulate the ZnO/p-Si/Al solar cell are presented in tables 5.4 and 5.5. The same parameters of p-Si used in the studied CdO/p-Si solar cell are used in this study.

Table 5.4: Parameters used to simulate the ZnO film of the ideal ZnO/p-Si/Al solar cell.

Parameter	Value	Reference
Band gap	3.3 eV	Extracted
Electron affinity	4.35	[49]
Donor density, N_D	$5x10^{19}$ cm^{-3}	[51]
CB effective density of states, N_C	$2.2x10^{19}$ cm^{-3}	[73]
VB effective density of states, N_V	$1.8x10^{19}$ cm^{-3}	[73]
Electron mobility	8	[2]
SRH lifetime for electrons and holes	$1x10^{-9}$ s	[73]

5.3.3.2. Amorphous ZnO:

The parameters of the different constituents of the DOS used to simulate their effect on the ZnO/p-Si/Al solar cell performance are presented in table 5.5.

Table 5.5: Parameters of the DOS used to simulate the ZnO film of the ZnO/p-Si/Al solar cell.

Parameter	Value
Standard deviation of the deep acceptors σ_A (eV)	0.07
Standard deviation of the deep donors σ_D (eV)	0.07
Peak energy of deep acceptors E_{GA} (eV)	1.5
Peak energy of deep donors E_{GD} (eV)	1.5
Characteristic slope energy of the valence band-tail states E_A (eV)	0.1
Characteristic slope energy of the conduction band-tail states E_D (eV)	0.1

5.3.3.3. Simulation of the effect of defects on the ZnO/p-Si/Al solar cell performance:

The effect of the different constituents of the DOS on the J-V characteristics of the non-ideal ZnO/p-Si solar cell is shown in Figure 5.23. Simulation of the effect of the fixed oxide charge density, tail and Gaussian defects on the ZnO/p-Si/Al solar cell has led to comparable values between simulation and measurement for FF, $V_{OC}$and J_{SC}. The values which gave comparable simulation and measurement were: a total density of the Gaussian states, $G_{Ga,d}$=$1.5x10^{15}$ cm^{-3}/eV,

a density of tail states, $G_{Ta,d}$= 2.5x10^{20} cm^{-3}/eV, and a fixed oxide charge density; Qf=1.5x10^{11} cm^{-2}.

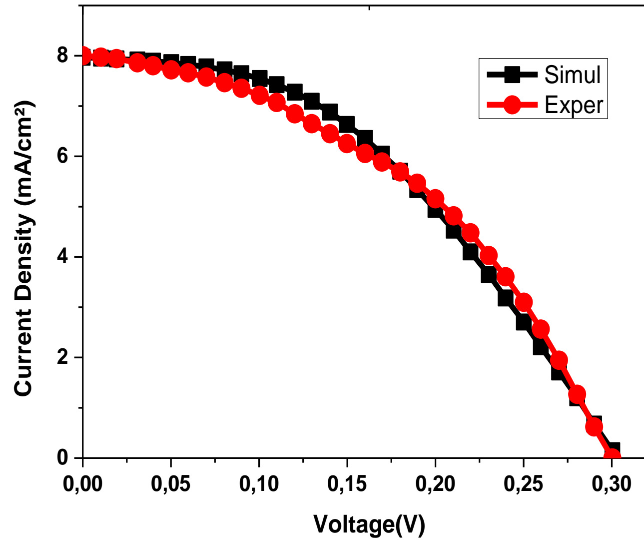

Figure 5.23: Comparison of simulated and measured J-V characteristics of the ZnO/p-Si solar cell.

As it is very clear there is a very good agreement between simulation and measurements. The extracted parameters gave almost a perfect match between simulation and measurement.

Table 5.6: Table gathers all parameter values which gave comparable simulation and measurement of both CdO/p-Si and ZnO/p-Si solar cells.

Solar cells	**CdO/p-Si**	**ZnO/p-Si**
Tail DOS, acceptor-like, G_{TA} (cm^{-3}/eV)	G_{TA} (CdO)= 1.5x10^{19}	G_{TA} ZnO: 2.5x10^{20}
Tail DOS, donor-like , G_{TD} (cm^{-3}/eV)	G_{TD} (CdO)= 1.5x10^{19}	G_{TD} ZnO: 2.5x10^{20}
Gaussian DOS, acceptor-like, G_{GA} (cm^{-3}/eV)	G_{GA} (CdO)= 1x10^{15}	G_{GA} ZnO: 1.5x10^{15}
Gaussian DOS, donor-like, G_{GD} (cm^{-3}/eV)	G_{GD} (CdO)= 1x10^{15}	G_{GD} ZnO: 1.5x10^{15}
Density of fixed oxide charge, Q_F (cm^{-2})	Q_F (CdO)= 5x10^{11}	Q_F (ZnO)= 1.5x10^{11}
Density of acceptors, N_A (cm^{-3})	N_A (p-Si)= 2.07x10^{17}	N_A (p-Si)= Fixed

5.4. Conclusion:

CdO and ZnO thin films were prepared by sol-gel spin-coating. The film have been characterized using optical measurements. The optical constants of the CdO and ZnO films were analyzed and investigated. CdO/p-Si and ZnO/p-Si heterojunction solar cells which were then fabricated. Electrical characterisation of these solar cells showed a poor performanc. In this work numerical simulation using Silvaco ATLAS software is used to model the aforementioned solar cells and to elucidate this poor performance. Several possible causes were considered: the presence of defects in the semiconductor (tail or Gaussian states), fixed charge, and doping of silicon. For the CdO film, the defects were found to mainly affect V_{OC} and J_{SC}. On the other hand FF is mainly affected by the p-type doping of silicon. Good comparison between experimental and simulation results was obtained with these values: an acceptor p-type doping of silicon, N_A= 2.07x10^{17} cm^{-3}, a total density of the Gaussian states, $G_{Ga,d}$=1x10^{15} cm^{-3}/eV, a density of tail states, $G_{Ta,d}$= 1.5x10^{19} cm^{-3}/eV, and a fixed oxide charge density; Qf=5x10^{11} cm^{-2}. These values produced a good agreement between simulated and measured *J-V* characteristics of the solar cell under the effect of the light power intensity. For the ZnO film, the simulation of the effect of the fixed oxide charge density, tail and Gaussian defects on the ZnO/p-Si/Al solar cell has led to comparable values between simulation and measurement for FF, V_{OC} and J_{SC}. The values which gave comparable simulation and measurement were: a fixed oxide charge density, Qf=1.5x10^{11} cm^{-2}, a total density of the Gaussian states, $G_{Ga,d}$=1.5x10^{15} cm^{-3}/eV and a density of tail states, $G_{Ta,d}$= 2.5x10^{20} cm^{-3}/eV.

Chapter 6: Conclusion and perspectives

Chapter 6: Conclusion and perspectives

6.1. Conclusion:

CdO and ZnO thin films were prepared by sol-gel spin-coating. The films have been characterized using optical measurements. The optical constants of the CdO and ZnO films, band gap (Eg), refractive index (n), extinction coefficient (k), to be used in simulation, were analyzed and investigated. CdO/p-Si and ZnO/p-Si heterojunction solar cells which were then fabricated. Electrical characterisation of these solar cells showed a poor performance. In this work numerical simulation using Silvaco ATLAS software is used to model the aforementioned solar cells and to elucidate this poor performance. Several possible causes were considered: the presence of defects in the semiconductor (tail or Gaussian states), fixed charge, and doping of silicon. Evidently the first case produced results far from reality. In the second case, however, and by adjusting the constituents of the band gap states,

1. For CdO material, the simulation of the effect of the tail and Gaussian defects of CdO on the Al/CdO/p-Si/Al solar cell has led to comparable values between simulation and measurement for both V_{OC} and J_{SC}. However the effect was not able to obtain comparable values for FF. The acceptor doping of silicon induced comparable values for FF. Combing the effects of defects in CdO and doping in Si, all parameters were almost perfectly reproduced when the solar cell is subjected to AM1.5 spectrum (light power intensity of 100 mW/cm^2). The values which gave comparable simulation and measurement were: an acceptor p-type doping of silicon, N_A= 2.07x10^{17} cm^{-3}, a total density of the Gaussian states, $G_{Ga,d}$=1x10^{15} cm^{-3}/eV, a density of tail states, $G_{Ta,d}$= 1.5x10^{19} cm^{-3}/eV, and a fixed oxide charge density; Qf=5x10^{11} cm^{-2}. These values were then used to simulate the effect of light intensity on the J-V characteristics of the solar cell and compared to measurements.
2. For ZnO material, the simulation of the effect of the fixed oxide charge density, tail and Gaussian defects of ZnO on the ZnO/p-Si/Al solar cell has led to comparable values between simulation and measurement for FF, V_{OC} and J_{SC}. The values which gave comparable simulation and measurement were: a fixed oxide charge density, Qf=1.5x10^{11}

cm^{-2}, a total density of the Gaussian states, $G_{Ga,d}$=1.5x10^{15} cm^{-3}/eV and a density of tail states, $G_{Ta,d}$= 2.5x10^{20} cm^{-3}/eV.

6.2. Perspectives:

The obtained results of studying the CdO/p-Si and ZnO/p-Si heterojunction solar cells left some questions unresolved. Several issues which were observed in these solar cells should be investigated in order to achieve a better characterization.

The existed defects in the CdO and ZnO materials and changing of the doping concentration of the absorber layer, p-Si, have remarkable effects on the efficiency of these solar cells. Therefore, the interest of studying these parameters may lead to improve the electrical characteristics.

In our perspectives, if it will be possible, we will prepare similar structures by using different techniques and different absorber substrates. We can summarize these projects in these following titles,

- Use different deposition methods.
- Study the effect of solution molarity.
- Study the effect of CdO and ZnO doping.
- Change the absorber layers with others have different doping concentration.

References

References

[1] S. K. Deb, 'Thin-film solar cells: an overview', *Natl. Renew. Energy Lab.*, pp. 375–379, 1996.

[2] T. L. Chu and S. S. Chu, 'Thin film II-VI photovoltaics', *Solid-Stare Electron.*, vol. 38, pp. 533–549, 1995.

[3] R. Ghosh, B. Mallik, and D. Basak, 'Dependence of photoconductivity on the crystallite orientations and porosity of polycrystalline ZnO films', *Appl. Phys. A*, vol. 81, pp. 1281–1284, 2005.

[4] F. Yakuphanoglu, 'Nanocluster n-CdO thin film by sol-gel for solar cell applications', *Appl. Surf. Sci.*, vol. 257, pp. 1413–1419, 2010.

[5] F. Sajid, S. H. Syed, R. Saira, and N. Shahzad, 'ZnO/c-Si solar cell fabricated through sol-gel and spin coating', *World Congr. ACEM 12*, pp. 2202–2208, 2012.

[6] NCERT authors, 'Chapter Fourteen: Semiconductor electronics: materials, devices and simple circuits', in *PhysicsTextbook: Class 12*, 2014th ed., National Council of Education Research and Training, 2014, pp. 468–512.

[7] D. A. Neamen, 'Chapter 3: Introduction to the Quantum Theory of Solids', in *Semiconductor Physics and Devices*, 3rd ed., Boston McGraw-Hill, 2003, pp. 56–102.

[8] C. H. Chenming, 'Chapter 1: Electrons and Holes in Semiconductors', in *Modern Semiconductor Devices for Integrated Circuits*, 1st ed., Pearson, 2009, pp. 1–34.

[9] Y. Y. Peter and C. Manuel, *Fundamentals of Semiconductors: Physics and Materials Properties*, 4th ed., vol. 7, no. 11. Springer, 2010.

[10] J. I. Pankove and T. D. Moustakas, *Semiconductors and Semimetals*, 1st ed. Academic Press, 1998.

[11] S. Nakamura and G. Fasol, *The Blue Laser Diode. GaN Based Light Emitters and Lasers*. Springer, 1997.

[12] V. A. Fedorov, A. V. Ganshin, and Y. N. Korkishk, ‘Ion Exchange in II-VI Crystals: Thermodynamics, Kinetics, and Technology’, *phys. stat. sol.*, vol. 9, 1993.

[13] C. Aydin, M. Benhaliliba, and A. A. Al-ghamdi, ‘Determination of optical band gap of ZnO:ZnAl2O4 composite semiconductor nanopowder materials by optical reflectance method’, *J. Electroceram*, 2013.

[14] M. Benhaliliba *et al.*, ‘Luminescence and physical properties of copper doped CdO derived nanostructures’, vol. 132, pp. 2653–2658, 2012.

[15] J. Wang and M. Isshiki, ‘Wide-Bandgap II–VI Semiconductors: Growth and Properties’, *Springer Handb. Electron. Photonic Mater.*, pp. 325–342, 2007.

[16] D. Verity, F. J. Bryant, C. G. Scott, and D. Shaw, ‘Dlts investigation of some’, vol. 59, pp. 234–239, 1982.

[17] J. M. Harris and B. Roach, ‘Chapter 11: Energy: The Great Transition’, in *Environmental and Natural Resource Economics: A Contemporary Approach*, 4th ed., no. Due, Global Development And Environment Institute, Tufts University, 2017, pp. 1–39.

[18] S. C. Yadav and M. D. Uplane, ‘Synthesis and properties of Boron doped ZnO thin films by spray CVD technique at low substrate temperature’, *Int. J. Eng. Sci. Technol.*, vol. 4, no. 12, pp. 4893–4898, 2012.

[19] A. F. Aaktaruzzaman, G. L. Sharma, and L. K. Malhotra, ‘Electrical, Optical and Annealing Characteristics Of Zno:Al Films Prepared By Spray Pyrolysis’, *Thin Solid Films*, vol. 198, pp. 67–74, 1991.

[20] M. Arita, M. Yamaguchi, and M. Masuda, ‘Electrical and Optical Properties of Germanium-Doped Zinc Oxide Thin Films’, *Mater. Trans.*, vol. 45, no. 11, pp. 3180–3183, 2004.

[21] C. E. Benouis, M. Benhaliliba, A. J. Sanchez, M. S. Aida, F. Chami, and F. Yakuphanoglu, ‘The effect of indium doping on structural , electrical conductivity , photoconductivity and density of states properties of ZnO films’, *J. Alloys Compd.*, vol. 490, pp. 62–67, 2010.

[22] B. Efafi, S. S. Mousavi, M. Hossein, M. Ara, B. Ghafari, and H. R. Mazandarani, ‘A

Method for Optimizing the Electrical Conductivity of Al:ZnO TCO Films', *Mater. Lett.*, 2017.

[23] C. Liu, F. Yun, and H. Morkoc, 'Ferromagnetism of ZnO and GaN : A Review', vol. 6, pp. 555–597, 2005.

[24] J. Tian, M. Liang, Y. Ho, Y. Liu, and L. Chang, 'Growth of a-plane ZnO thin films on LaAlO3 (1 0 0) substrate by metal-organic chemical vapor deposition', *J. Cryst. Growth*, vol. 310, pp. 777–782, 2008.

[25] X. Z. Cui *et al.*, 'Growth of single-crystalline ZnO film with two-dimensional periodic structure on Si (111) substrate by molecular beam epitaxy', *J. Cryst. Growth*, vol. 310, pp. 5428–5431, 2008.

[26] N. Sakai, Y. Umeda, F. Mitsugi, and T. Ikegami, 'Characterization of zinc oxide thin films prepared by pulsed laser deposition at room temperature', *Surf. Coat. Technol.*, vol. 202, pp. 5467–5470, 2008.

[27] Y. Caglar, M. Caglar, S. Ilican, and F. Yakuphanoglu, 'Thermally stimulated current and space charge limited current mechanism in film of the gold/zinc oxide/gold type', *Phys. B*, vol. 392, pp. 99–103, 2007.

[28] M. Caglar, S. Ilican, Y. Caglar, and F. Yakuphanoglu, 'Electrical conductivity and optical properties of ZnO nanostructured thin film', *Appl. Surf. Sci.*, vol. 255, pp. 4491–4496, 2009.

[29] Y. Yang, L. Wang, H. Yan, S. Jin, and T. J. Marks, 'Highly transparent and conductive double-layer oxide thin films as anodes for organic light-emitting diodes', *Appl. Phys. Lett.*, vol. 89, p. 51116, 2006.

[30] B. Saha, R. Thapa, and K. K. Chattopadhyay, 'Bandgap widening in highly conducting CdO thin film by Ti incorporation through radio frequency magnetron sputtering technique', *Solid State Commun.*, vol. 145, pp. 33–37, 2008.

[31] Z. Zhao, D. L. Morel, and C. S. Ferekides, 'Electrical and optical properties of tin-doped CdO films deposited by atmospheric metalorganic chemical vapor deposition', *Thin Solid Films*, vol. 413, pp. 203–211, 2002.

[32] R. Maity and K. K. Chattopadhyay, 'Synthesis and characterization of aluminum-doped CdO thin films by sol-gel process', *Sol. Energy Mater. Sol. Cells*, vol. 90, pp. 597–606, 2006.

[33] S. Jin *et al.*, 'Dopant Ion Size and Electronic Structure Effects on Transparent Conducting Oxides. Sc-Doped CdO Thin Films Grown by MOCVD', *J. Am. Chem. Soc.*, vol. 126, pp. 13787–13793, 2004.

[34] R. K. Gupta, K. Ghosh, R. Patel, S. R. Mishra, and P. K. Kahol, 'Structural , optical and electrical properties of In doped CdO thin fi lms for optoelectronic applications', *Mater. Lett.*, vol. 62, pp. 3373–3375, 2008.

[35] A. A. Dakhel, 'Effect of thallium doping on the electrical and optical properties of CdO thin films', *phys. stat. sol.*, vol. 205, no. 11, pp. 2704–2710, 2008.

[36] R. K. Gupta, K. Ghosh, R. Patel, S. R. Mishra, and P. K. Kahol, 'Preparation and characterization of highly conducting and transparent Al doped CdO thin films by pulsed laser deposition', *Curr. Appl. Phys.*, vol. 9, pp. 673–677, 2009.

[37] J. Santos-Cruz *et al.*, 'Dependence of electrical and optical properties of sol-gel prepared undoped cadmium oxide thin films on annealing temperature', *Thin Solid Films*, vol. 493, pp. 83–87, 2005.

[38] T. K. Subramanyam, S. Uthanna, and B. S. Naidu, 'Preparation and characterization of CdO films deposited by dc magnetron reactive sputtering', *Mater. Lett. 35*, vol. 35, pp. 214–220, 1998.

[39] N. Ueda, H. Maeda, H. Hosono, and H. Kawazoe, 'Band-gap widening of CdO thin films', *J. Appl. Phys.*, vol. 84, no. 11, p. 6174, 1998.

[40] B. J. Lokhande, P. S. Patil, and M. D. Uplane, 'Studies on cadmium oxide sprayed thin films deposited through non-aqueous medium', *Mater. Chem. Phys.*, vol. 84, pp. 238–242, 2004.

[41] M. Yan, M. Lane, C. R. Kannewurf, and R. P. H. Chang, 'Highly conductive epitaxial CdO thin films prepared by pulsed laser deposition', *Appl. Phys. Lett.*, vol. 78, no. 16, pp. 2342–2344, 2001.

[42] X. Liu, C. Li, S. Han, J. Han, and C. Zhou, 'Synthesis and electronic transport studies of CdO nanoneedles', *Appl. Phys. Lett.*, vol. 82, no. 12, pp. 1950–1952, 2003.

[43] L. R. León-Gutiérrez, J. J. Cayente-Romero, J. M. Peza-Tapia, E. Barrera-Calva, J. C. Martinez-Flores, and M. Ortega-Lopez, 'Some physical properties of Sn-doped CdO thin films prepared by chemical bath deposition', *Mater. Lett.*, vol. 60, pp. 3866–3870, 2006.

[44] S. Adachi, *Properties of Semiconductor Alloys: Group-IV, III-V and II-VI Semiconductors*, 1st ed. John Wiley & Sons, Ltd, Publication, 2009.

[45] H. H. Afify, N. M. Ahmed, M. T. Y. Tadros, and F. M. Ibrahim, 'Temperature Dependence Growth of CdO Thin Film Prepared by Spray Pyrolysis', *J. Electr. Syst. Inf. Technol.*, vol. 1, pp. 120–128, 2014.

[46] Y. Dou, T. Fishlock, and R. G. Egdell, 'Band-gap shrinkage in n-type-doped CdO probed by photoemission spectroscopy', *Phys. Rev. B*, vol. 55, no. 20, pp. 381–384, 1997.

[47] F. Yakuphanoglu, M. Caglar, Y. Caglar, and S. Ilican, 'Electrical characterization of nanocluster n-CdO/p-Si heterojunction diode', *J. Alloys Compd.*, vol. 506, pp. 188–193, 2010.

[48] W. R. L. Lambrecht, A. V. Rodina, S. Limpijumnong, B. Segall, and B. K. Meyer, 'Valence-band ordering and magneto-optic exciton fine structure in ZnO', *Phys. Rev. B*, vol. 65, pp. 75207–1, 2002.

[49] F. Yakuphanoglu, Y. Caglar, M. Caglar, and S. Ilican, 'ZnO/p-Si heterojunction photodiode by sol-gel deposition of nanostructure n-ZnO film on p-Si substrate', *Mater. Sci. Semicond. Process.*, vol. 13, pp. 137–140, 2010.

[50] A. A. Dakhel, 'Effect of tellurium doping on the structural , optical , and electrical properties of CdO', *Sol. Energy*, vol. 84, pp. 1433–1438, 2010.

[51] S. Alamdari, M. J. Tafreshi, and M. S. Ghamsari, 'The effects of Indium precursors on the structural , optical and electrical properties of nanostructured thin ZnO films', *Mater. Lett.*, 2017.

[52] M. Furuta, T. Hiramatsu, T. Matsuda, C. Li, H. Furuta, and T. Hirao, 'Thermal Stability and Sheet Resistance of Undoped ZnO Films Deposited on Insulators', *Electrochem.*

Solid-State Lett., vol. 12, pp. 74–76, 2009.

[53] A. W. Vere, *Defects in Crystals*, 1st ed. Springer US, 1987.

[54] C. Kittel, *Introduction to Solid State Physics*, 7th ed. New York: John Wiley & Sons, Ltd, Publication, 1996.

[55] L. Schmidt-Mende and J. L. MacManus-Driscoll, 'ZnO-nanostructures, defects, and devices', *Mater. Today*, vol. 10, no. 5, pp. 40–48, 2007.

[56] J. Han, P. Q. Mantas, and A. M. R. Senos, 'Defect chemistry and electrical characteristics of undoped and Mn-doped ZnO', *J. Eur. Ceram. Soc.*, vol. 22, pp. 49–59, 2002.

[57] K. I. Hagemark, 'Defect Structure of Zn-Doped ZnO', *J. Solid State Chem.*, vol. 16, pp. 293–299, 1976.

[58] F. A. Kröger, *The Chemistry of Imperfect Crystals*, 2nd ed. North-Holland: Amsterdam, 1974.

[59] P. D. C. King, T. D. Veal, P. H. Jefferson, J. Zuniga-Pérez, V. Munoz-Sanjosé, and C. F. McConville, 'Unification of the electrical behavior of defects, impurities, and surface states in semiconductors: Virtual gap states in CdO', *Phys. Rev. B*, vol. 79, pp. 35203–1, 2009.

[60] D. T. Speaks, M. A. Mayer, K. M. Yu, S. S. Mao, E. E. Haller, and W. Walukiewicz, 'Fermi level stabilization energy in cadmium oxide', *J. Appl. Phys.*, vol. 107, no. 2010, pp. 113706–1, 2010.

[61] W. Walukiewicz, 'Mechanism of Fermi-level stabilization in semiconductors', *Phys. Rev. B*, vol. 37, no. 9, p. 4760, 1988.

[62] M. N. Amini, R. Saniz, D. Lamoen, and B. Partoens, 'Hydrogen impurities and native defects in CdO', *J. Appl. Phys.*, vol. 110, pp. 63521–1, 2011.

[63] F. C. Krebs, *Solar Cells: Materials, Manufacture and Operation*, 1st ed. Elsevier Ltd, 2005.

[64] S. M. Sze and K. K. Ng, *Physics of Semiconductor Devices*, 3rd ed. John Wiley & Sons, Ltd, Publication, 2007.

[65] C. T. Sah, R. N. Noyce, and W. Shockley, 'Carrier Generation and Recombination in P-N Junctions and P-N Junction Characteristics', *IEEE*, vol. 45, pp. 1228–1243, 1957.

[66] P. Bhattacharya, *Semiconductor Optoelectronic Devices*, 2nd ed. Prentice Hall, 1996.

[67] J. R. Sites and P. H. Mauk, 'Diode quality factor determination for thin-film solar cells', *Sol. Cells*, vol. 27, pp. 411–417, 1989.

[68] X. Wang, F. Shi, X. Gao, C. Fan, W. Huang, and X. Feng, 'A sol-gel dip/spin coating method to prepare titanium oxide fi lms', *Thin Solid Films*, vol. 548, pp. 34–39, 2013.

[69] L. L. Hench and J. K. West, 'The Sol-Gel Process', *Chem. Rev.*, vol. 90, pp. 33–72, 1990.

[70] C. J. Brinker and G. W. Scherer, *Sol-Gel Science: The Physics and Chemistry of Sol–Gel Processing*, 1st ed. Academic Press, 1990.

[71] L. E. Scriven, 'Physics and Applications of Dip Coating and Spin Coating', *Mat. Res. Soc. Symp. Proc.*, vol. 121, pp. 717–729, 1988.

[72] J. A. N. T. Soares, *Chapter 2: Introduction to Optical Characterization of Materials*. Springer Science+Business Media New York, 2014.

[73] *Atlas User's Manual: Device Simulation Software*. Santa Clara, USA: Silvaco, Inc, 2013.

[74] N. Zebbar, M. S. Aida, A. E. K. Hafdallah, O. Daranfad, H. Lekiket, and M. Kechouane, 'Properties of ZnO thin films grown on Si substrates by ultrasonic spray and ZnO/Si heterojunctions', *Mater. Sci. Forum*, vol. 609, pp. 133–137, 2009.

[75] Y. Zhang, G. Du, B. Zhang, Y. Cui, H. Zhu, and Y. Chang, 'Properties of ZnO thin films grown on Si substrates by MOCVD and ZnO/Si heterojunctions', *Semicond. Sci. Technol.*, vol. 20, pp. 1132–1135, 2005.

[76] X. Li *et al.*, 'Properties of ZnO thin films grown on Si substrates by photo-assisted MOCVD', *Semicond. Sci. Technol.*, vol. 20, pp. 1132–1135, 200AD.

[77] F. Zhu-x, L. Bi-xi, and L. Gui-hong, 'Photovoltaic Effect of ZnO/Si Heterostructure', *Chinese Phys. Lett.*, vol. 16, pp. 753–755, 1999.

[78] S. Chala, N. Sengouga, and F. Yakuphanoglu, 'Modeling the effect of defects on the performance of an n-CdO/p-Si solar cell', *Vacuum*, vol. 120, pp. 81–88, 2015.

[79] Y. S. Ocak, 'Electrical characterization of DC sputtered ZnO/p-Si heterojunction', *J. Alloys Compd.*, vol. 513, pp. 130–134, 2012.

[80] M. Nawaz, E. S. Marstein, and A. Holt, 'Design Analysis of ZnO/c-Si Heterojunction Solar Cell', *35th IEEE Photovolt. Spec. Conf.*, pp. 2213–2218, 2010.

[81] F. Yakuphanoglu, 'Heat treatment effect on the single oscillator parameters and optical band gap of an organic thin film', *Opt. Mater. (Amst).*, vol. 29, pp. 253–256, 2006.

[82] R. A. Ismail and O. A. Abdulrazaq, 'A new route for fabricating CdO/c-Si heterojunction solar cells', *Sol. Energy Mater. Sol. Cells*, 2007.

[83] F. Yakuphanoglu, 'Photovoltaic properties of the organic-inorganic photodiode based on polymer and fullerene blend for optical sensors', *Sensors Actuators A*, vol. 141, pp. 383–389, 2008.

[84] M. S. Kim *et al.*, 'Growth and Characterization of Indium-Doped Zinc Oxide Thin Films Prepared by Sol-Gel Method', *Acta Phys. Pol. A*, vol. 121, pp. 217–220, 2012.

[85] F. Yakuphanoglu, A. Cukurovali, and I. Yilmaz, 'Refractive index and optical absorption properties of the complexes of a cyclobutane containing thiazolyl hydrazone ligand', *Opt. Mater. (Amst).*, vol. 27, pp. 1363–1368, 2005.

[86] M. R. Islam and J. Podder, 'Optical properties of ZnO nano fiber thin films grown by spray pyrolysis of zinc acetate precursor', *Cryst. Res. Technol.*, vol. 44, pp. 286–292, 2009.

[87] W. Shockley and W. T. Read, 'Statistics of the Recombinations of Holes and Electrons', *Phys. Rev.*, vol. 87, no. 5, pp. 835–842, 1952.

[88] R. N. Hall, 'Electron-Hole Recombination in Germanium', *Lett. to Ed.*, p. 387, 1952.

[89] M. Zeman, J. Van Den Heuvel, M. Kroon, and J. Willemen, *Amorphous semiconductor analysis (ASA) user's manual*, Version 3. Delft: Delft Univ. of Technology; 2000.

[90] A. Meftah, A. Meftah, F. Hiouani, and A. Merazga, 'Numerical simulation of the defect density influence on the steady state response of a silicon-based p-i-n cell', *J. Phys. Condens. Matter 16*, vol. 16, pp. 2003–2016, 2004.

Publications and communications

Publications and communications

1. Publications:

1. S. Chala, N. Sengouga and F. Yakuphanoglu, “Modeling the effect of defects on the performance of an n-CdO/p-Si solar cell”, Vacuum. 120 (2015) 81–88. doi:10.1016/j.vacuum.2015.05.019.

2. S. Chala et *al.*, “Extraction of ZnO thin film parameters for ZnO/Si solar cells modelling”, SEEP2017, University of Maribor Press (2017) 89-98, https://doi.org/10.18690/978-961-286-058-5.8.

2. Communications:

1. S. Chala, N. Sengouga and F. Yakuphanoglu, “Characterisation and simulation of an n-CdO/p-Si heterostructure for solar cell applications”, International Conference on Nanoscience and Nanotechnolgy for Next Generation (NanoNG), 20-22 August 2014, Firat University, Elazig, Turkey.

2. S. Chala, N. Sengouga and F. Yakuphanoglu, “Modeling the effect of defects on the performance of an n-CdO/p-Si solar cell”, International Conference on Science & Applications of Thin Films (SATF), 15-19 September, 2014, Cesme, Izmir, Turkey.

3. S. Chala et *al.*, “Extraction of ZnO thin film parameters for ZnO/Si solar cells modelling” International Conference on Sustainable Energy & Environmental Protection (SEEP), 27-30 June 2017, Golf Hotel, Bled, Slovenia.

Vacuum 120 (2015) 81–88

Contents lists available at ScienceDirect

Vacuum

journal homepage: www.elsevier.com/locate/vacuum

Modeling the effect of defects on the performance of an n-CdO/p-Si solar cell

S. Chala [a], N. Sengouga [a, *], F. Yakuphanoglu [b]

[a] *Laboratory of Metallic and Semiconducting Materials, Université de Biskra, 07000 Biskra, Algeria*
[b] *Physics Department, Firat University, 23169 Elazig, Turkey*

A R T I C L E I N F O

Article history:
Received 29 October 2014
Received in revised form
23 April 2015
Accepted 18 May 2015
Available online 28 May 2015

Keywords:
CdO/Si solar cell
Characterisation
Simulation
Defects

A B S T R A C T

The interest in the study of Cadmium oxide (CdO) for photonic applications has increased significantly because of its promising electrical and optical properties. Real solar cells based on an n-CdO/p-Si heterostructures show poor photovoltaic performance, however. In this work numerical simulation is used to elucidate this poor performance by considering two cases. CdO is firstly considered as a perfect crystalline semiconductor. The second case models CdO as a semiconductor with continuous distribution of defects states in its band-gap, similar to an amorphous semiconductor, made of two tail bands (a donor-like and an acceptor-like) and two Gaussian distribution deep level bands (an acceptor-like and a donor-like). Evidently the first case produced results far from reality. In the second case, however, and by adjusting the constituents of the band-gap states the open circuit voltage (V_{OC}) and the short circuit current (J_{SC}) were almost perfectly reproduced but not the fill factor (FF) and the conversion efficiency (η). The p-type doping of Silicon adjustment has lead to a better reproduction of the two latter parameters.

© 2015 Elsevier Ltd. All rights reserved.

NanoNG'14 INTERNATIONAL CONFERENCE

NANOSCIENCE & NANOTECHNOLOGY FOR NEXT GENERATION

CERTIFICATE of PARTICIPATION

THIS IS TO CERTIFY THAT

SLIMANE CHALA

HAS PARTICIPATED IN THE INTERNATIONAL NANOSCIENCE & NANOTECHNOLOGY FOR NEXT GENERATION CONFERENCE, HELD IN ELAZIĞ, TURKEY ON AUGUST 20-22, 2014

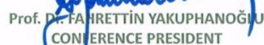

Prof. Dr. FAHRETTİN YAKUPHANOĞLU
CONFERENCE PRESIDENT

20-22 August 2014

SATF2014

SCIENCE & APPLICATIONS OF THIN FILMS CONFERENCE & EXHIBITION

This is to certify that

SLIMANE CHALA

has attended "**Science and Applications of Thin Films Conference and Exhibiton (SATF2014)**" held in Altinyunus Resort & Thermal Hotel between the dates of 15-19 September 2014, Izmir, Turkey

Prof. Dr. Lutfi OZYUZER
Chair of SATF2014

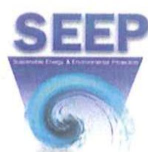

CERTIFICATE

SLIMANE CHALA

PRESENTED THE PAPER

EXTRACTION OF ZNO THIN FILM PARAMETERS FOR ZnO-Si SOLAR CELLS MODELLING

AT THE 10TH INTERNATIONAL CONFERENCE ON

SUSTAINABLE ENERGY AND ENVIRONMENTAL PROTECTION

Bled, Slovenia

June 27th – 30th, 2017

Faculty of Chemistry and Chemical Engineering

UNIVERSITY OF THE WEST of SCOTLAND
UWS

General Chair

Emeritus Prof. Dr. Jurij Krope